

REPORT DOCUMENTATION PAGE			Form Approved OMB No. 0704-0188	
Public reporting burden for this collection of information is estimated to average 1 hour per response, including the time for reviewing instructions, searching existing data sources, gathering and maintaining the data needed, and completing and reviewing the collection of information. Send comments regarding this burden estimate or any other aspect of this collection of information, including suggestions for reducing this burden, to Washington Headquarters Services, Directorate for Information Operations and Reports, 1215 Jefferson Davis Highway, Suite 1204, Arlington, VA 22202-4302, and to the Office of Management and Budget, Paperwork Reduction Project (0704-0188), Washington, DC 20503.				
1. AGENCY USE ONLY (Leave blank)	2. REPORT DATE FEB 1992	3. REPORT TYPE AND DATES COVERED Final 7/10/91-1/31/92		
4. TITLE AND SUBTITLE Projectile Yaw Sensing Technology		5. FUNDING NUMBERS C DAAA15-91-C-0101		
6. AUTHOR(S) Steven M. Buc				
7. PERFORMING ORGANIZATION NAME(S) AND ADDRESS(ES) SAA International, Ltd. 53 Lake Park Court Germantown, Maryland 20874		8. PERFORMING ORGANIZATION REPORT NUMBER 91-02		
9. SPONSORING / MONITORING AGENCY NAME(S) AND ADDRESS(ES) Ballistics Research Laboratory ATTN: SLCBR-AS Building 328, Room 223 Aberdeen Proving Ground, Maryland 21010		10. SPONSORING / MONITORING AGENCY REPORT NUMBER		
11. SUPPLEMENTARY NOTES		19980413 064		
12a. DISTRIBUTION / AVAILABILITY STATEMENT Approved for public release; distribution is unlimited.				
13. ABSTRACT (Maximum 200 words) The in-flight yaw and spin motion of artillery shells and other munitions is frequently measured by the use of optical sensing and standard RF telemetry techniques. The standard system that is used is called the Yawsonde. The technique that has been investigated replaces this device with an inertial sensor package. This program has determined that all three characteristic rates of motion -- spin, nutation, and precession -- are directly calculable from each of several inertial sensor configurations. In addition, there are currently available components that are suitable for this application and can survive the launch environment. DTIC QUALITY INSPECTED 2				
14. SUBJECT TERMS gyroscope, accelerometer, pitch, yaw, roll sensing, signal demodulation, telemetry, Fourier analysis, phase locked loop, yaw arms, epicycle motion		15. NUMBER OF PAGES 88		16. PRICE CODE
17. SECURITY CLASSIFICATION OF REPORT unclassified	18. SECURITY CLASSIFICATION OF THIS PAGE unclassified	19. SECURITY CLASSIFICATION OF ABSTRACT unclassified	20. LIMITATION OF ABSTRACT unlimited	

Projectile Yaw Sensing Technology

Prepared by:

Steven M. Buc

S. ADELMAN ASSOCIATES
301 Maple Ave W.
Suite 100
Vienna, VA 22180

February 1992

Contract DAAA15-91-C-0101

Prepared for:

Ballistics Research Laboratory
ATTN: SLCBR-AS
Bldg 328, Rm 223
Aberdeen Proving Ground, MD 21010

Contents

Abstract.....	iii
Figures.....	iv
Tables.....	vii
 1.0 Summary.....	 1
 2.0 Introduction.....	 2
General Considerations	2
Typical Epicycle Motions of Fin and Spin Stabilized Projectiles	2
Determination of the Yaw Arms from Superposition	9
Determination of the Yaw Arms from Integration of Accelerations	10
Determination of the Yaw Arms from Integration of Rates	13
Theoretical Sensor Configurations	13
 3.0 Methods, Assumptions and Procedures	 14
General considerations	14
Radially Oriented Accelerometers to Measure \dot{V} and \dot{W}	14
Radially Oriented Gyroscopes to Measure $\dot{\theta}$ and $\dot{\Psi}_m$	16
Axially Oriented Accelerometers to Measure \dot{U}	18
Axially Oriented Gyroscope to Measure Ω	18
Sensor configurations for Determining Roll Orientation.....	21
Alternate configuration for Determining Roll Orientation.....	21
Accelerometer Configurations for Nutation and Precession Rates.....	24
Methodology for Amplitude Demodulating Sensor Outputs.....	24
Qualitative Assessment of Projectile Stability.....	70
Fourier Analysis of Accelerometer Traces.....	70
Frequency and Amplitude Analysis of Outputs from Sensors.....	71
Direct Integration of Acceleration Traces.....	74
Simultaneous Integration of Sensor Outputs.....	79
Determining Roll Orientation with Phase Locked Loop.....	84
 4.0 Results and Discussions	 84
General considerations.....	84
The Binary Answer.....	84
Yaw Arm Calculation.....	85
Reconstruction of Epicycle Motion.....	85
 5.0 Conclusions	 86
General Considerations.....	86
Sensor Technical Data.....	87
 6.0 Recommendations	 88

List of Figures

Figure 1	Undamped Motion for M107 at Mach 2 and +5 degrees and +5 Radians/sec Pitch and Yaw	4
Figure 2	Epicycle Motion for Fin Stabilized Projectile with 50 Hz Spin Rate and +5 Degrees and +5 Radians/sec Initial Pitch and Yaw	5
Figure 2.1	Generic Fin Stabilized Projectile Design	8
Figure 3	Velocity and Angle Relationships for 6-DOF Trajectory	11
Figure 3 (a)	Equations of Motion, Initial Conditions, and Nomenclature for 6-DOF Trajectory	12
Figure 4	Radially Oriented Accelerometer Configuration for Determining \dot{V} and \dot{W}	15
Figure 5	Schematic of a Simple Rate Gyroscope	17
Figure 6	Gyroscope Based Telemetry Configuration for Determining Missile Pitch and Yaw Angular Rates	17
Figure 7	Accelerometer Configuration for Determining \dot{U} and Rate of Change of Total Yaw Angle, $\dot{\Omega}$	19
Figure 8	Axially Oriented Gyroscope Configuration for Measuring Total Yaw Angular Rate	20
Figure 9	Alternate Radially Oriented Accelerometer Configuration for Determining \dot{V} , \dot{W} , and Inertial Spin Rate	22
Figure 10	Total Yaw Angle History for Figure 1	26
Figure 11	Output from One Radial Accelerometer for Figure 1	27
Figure 12	Vector Sum of Two Orthogonal Radial Accelerometers for Figure 1	28
Figure 13	Undamped Motion for Modified Projectile with the same Initial Conditions as Figure 1	34
Figure 14	Output from One Radial Accelerometer for Figure 13	35
Figure 15	Vector Sum of Two Orthogonal Radial Accelerometers for Figure 13	36
Figure 16	Total Yaw Angle History for Figure 13	37
Figure 17	Damped Epicycle Motion of M107 at Mach 2 and +5 Degrees and +5 Radians/Sec Pitch and Yaw	38
Figure 18	Acceleration Trace from One Radial Accelerometer for Figure 17	39

Figure 19	Vector Sum of Two Orthogonal Radial Accelerometers for Figure 17	40
Figure 20	Total Angle of Attack (Yaw) History for Figure 17	41
Figure 21	Peak Values from Damped Acceleration Trace, Figure 19	42
Figure 22	Polynomial Interpolation of Peak Values from the Front Portion of Figure 21	43
Figure 23	Polynomial Interpolation of Peak Values from the Central Portion of Figure 21	44
Figure 24	Polynomial Interpolation of Peak Values from the Tail Portion of Figure 21	45
Figure 25	Generic Fin Stabilized Projectile Design	46
Figure 26	Epicycle Motion of Finner with 50 Hz Spin Rate	49
Figure 27	Angle of Attack History for Figure 26 Epicycle Motion	50
Figure 28	Vector Sum of Output from Two Orthogonal Radial Accelerometers for Figure 26 ..	51
Figure 29	Output from One Radial Accelerometer for Figure 26	52
Figure 30	Peak Values from Figure 29	54
Figure 31	Peak Values from Figure 30	55
Figure 32	Polynomial Interpolation of Figure 31 Data	56
Figure 33	Polynomial Interpolation of Figure 31 Data, cont.	57
Figure 34	Polynomial Interpolation of Figure 31 Data, cont.	58
Figure 35	Polynomial Interpolation of Figure 31 Data, cont.	59
Figure 36	Polynomial Interpolation of Figure 31 Data, concluded	60
Figure 37	Epicycle Motion of Finner with 75 Hz Spin Rate	62
Figure 38	Output from One Radial Accelerometer for Figure 37	63
Figure 39	Peak Values from Figure 38	64
Figure 40	Peak Values from Figure 39	65
Figure 41	Output from Two Orthogonal Radial Accelerometers for Figure 37	67
Figure 42	Peak Values from Figure 41	68
Figure 43	FFT Output for Figure 14 -- One Radially Oriented Accelerometer	69
Figure 43.2	Angular Rate Output from FFT for Figure 43	72

Figure 44	Total Yaw Angular Rate from Longitudinal Sensor for Figure 1	74
Figure 45	Total Yaw Angular Rate as Measured by Longitudinal Sensor	75
Figure 46	Rate of Change of Angle of Attack from Two Longitudinal Accelerometers for Figure 26	76
Figure 47	Rate of Change of Angle of Attack from Two Longitudinal Accelerometers for Figure 37	77
Figure 48	Angle of Attack History from 6DOF Simulation for Figure 37	78
Figure 49	Original Epicycle Motion from 6-DOF Simulation	80
Figure 50	Reconstructed Motion with zero Spin Rate Error	80
Figure 51	Reconstructed Motion with 10% Spin Rate Error	81
Figure 52	Reconstructed Motion with 5% Spin Rate Error	81
Figure 53	Reconstructed Motion with 1% Spin Rate Error	82
Figure 54	Reconstructed Motion with 0.5% Spin Rate Error	82
Figure 55	Reconstructed Motion with 0.25% Spin Rate Error	83
Figure 56	Reconstructed Motion with 0.10% Spin Rate Error	83

1.0 Summary

The objective of this Phase 1 SBIR research program has been to develop alternative sensor configurations suitable for use in radio telemetry devices for the purpose of measuring the in-flight yaw of various projectile types of interest to the BRL. Current yaw sensing telemetry is performed by the yawsonde, a device which senses the passage of the sun over optical slits as the projectile spins, nutates, and precesses. The obvious limitations of the yawsonde include the requirement for the sun to be visible to the sensor and within a narrow range of angles in the sky, depending on the flight profile. Even when these ephemeral requirements are met, however, the yawsonde still provides only limited information on the yawing motion of the projectile. The sensor configurations that have been developed and analyzed in this study use inertial sensors, and greatly expand the information which can be collected on the projectile motion, at the same time eliminating the ephemeral restrictions placed on the employment of the existing yawsonde device.

The telemetry sensors that were originally proposed as alternatives or supplements to the yawsonde included accelerometer or gyroscope based systems, or some combination of the two. Since the spinning, nutating, and precessing motion of a projectile generates both centripetal and tangential accelerations, as well as angular rates of motion, it was postulated that the acceleration or angular rate outputs from these devices would reveal unique characteristics of the pitching and yawing motion of the projectile during flight. Post processing of the sensor output would then allow analytical reconstruction of the projectile total yaw and any other useful information, which might be contained in the data. Postulated configurations would also have to consider the projectile launch and flight environment and the selection of devices of appropriate hardness and sensitivity to perform their required telemetry tasks.

It is significant that all program objectives have been met. It has been determined that all three characteristic rates of motion -- spin, nutation, and precession, as well as the magnitudes of the nutation and precession yaw arms -- are directly calculable from each of several inertial sensor configurations using combinations of accelerometers and/or rate gyroscopes. In addition, we have identified components that are suitable for this application and can survive the launch environment. These components will be able to fit into an existing fuze cavity in a way so that the structure and the sensor will survive the launch environment. We are now at the point where detailed component tradeoffs can be made, hardware configurations can be designed in detail, hardware constructed, and performance verified. This device will permit all yawsonde functions to be performed, in addition to extracting many other useful yawing motion parameters, without the current restrictions and performance limitations.

2.0 Introduction

2.1 General Considerations

In order to perform analysis on the motion of typical projectiles, a six-degree-of-freedom trajectory simulation, using a fourth-order Runge Kutta integration scheme¹, was modified to provide acceleration and angular rate output for sensors located at a prescribed axial and radial position within a projectile body. The appropriate differential equations of motion for an earth-fixed six-degree-of-freedom particle trajectory² were incorporated into the model, as well as aerodynamic formulations applicable to both spin and fin stabilized projectiles³. Aerodynamic coefficients necessary to exercise the simulation were generated off-line for candidate spin and fin stabilized projectiles using software from References 4 and 5, respectfully.

The six-degree-of-freedom trajectory model was used to generate simulated sensor output for different projectile types, both fin and spin stabilized, subjected to various launch conditions that would generate significant yawing motions. These sensor outputs were then analyzed by various numerical and closed-form post processing algorithms developed during this effort to extract the projectile yawing motion parameters of interest. Numerous post processing approaches were hypothesized and tested, with some being clearly more successful and practical than others. Some data analysis was also performed in order to validate the results.

This study involved revisiting, on several occasions, approaches which had been initially abandoned in the earlier stages of the program in favor of pursuing other directions of investigation. In this sense, the study did not follow a straight path to a solution, but rather took a broad sweep at accumulating information by testing as many hypotheses as possible, and then re-evaluating most ideas in an iterative fashion as more knowledge was developed. Therefore, this presentation of our results does not imply any chronological order to their discovery.

2.2 Typical Epicycle Motions of Fin and Spin Stabilized Projectiles

Figure 1 shows the epicycle motion of a typical spin stabilized projectile, as calculated using the six-degree-of-freedom computer model developed in this study. In order to determine typical motions for a projectile, the projectile nose is given an initial pitch and yaw angle of 5 degrees to the left and down, and an initial pitch and yaw rate of 5 radians/second to the left and down. This drawing is a two dimensional representation of the motion that the nose of the projectile makes with respect to the projectile's center of gravity, as it follows

the flight path of the particle trajectory. The observer is looking forward from the projectile tail to nose.

For this particular computer run shown in Figure 1, aerodynamic damping was turned off, so that nutation and precession amplitudes would remain clearly visible over several seconds of flight time. Therefore, the only aerodynamic force acting on the projectile is the pitching moment, represented by C_{ma} . The full aerodynamic coefficients and mass properties for this projectile are given in Table 1. As the projectile nose traces the path shown in Figure 1, there are two modes of motion clearly visible. The first is the faster mode called nutation, and is shown as the many small clockwise loops that the nose makes on top of the slower circular motion about the flight path axis located at the origin of the graph. The larger and slower circular clockwise motion about the origin is the precession. Not visible on this graph is the inertial spin rate of the projectile about its longitudinal axis. In this simulation, the spin rate is also clockwise. All three rates of motion -- spin, nutation, and precession -- are all in the same sense and are, therefore, prograde.

Figure 2 shows the epicycle motion of a typical fin stabilized projectile (Figure 2.1). This projectile's nose is also given an initial pitch and yaw angle of 5 degrees to the left and down, and an initial pitch and yaw rate of 5 radians/second to the left and down. The full aerodynamic coefficients and mass properties for this projectile are given in Table 2. As with the previous computer run, aerodynamic damping was turned off, so that nutation and precession amplitudes would remain clearly visible over several seconds of flight time. As with the spin stabilized case, the fin stabilized projectile shows the same two characteristic modes of nutation and precession. However, because of the static stability of the fin stabilized projectile, the precession is retrograde to the nutation. By following the line traced out by the projectile nose, one observes small loops going in a clockwise path, with each succeeding loop following a counter-clockwise direction.

Given these typical epicycle motions, the objective of this research is to develop a sensor scheme which allows determination of the amplitude of each of these nutation and precession yaw arms. One can see in Figure 1 that the projectile nose oscillates between a total angle of attack of between 5.25 and 11.6 degrees. This maximum and minimum yaw angle equals the sum and difference of the nutation yaw arm on top of the precession yaw arm. The same superposition of yaw arms applies to the fin stabilized case, as well. It is the determination of these yaw arms, through analysis of in-flight telemetry data, provided by a suitable sensor configuration, which is the goal of this research.

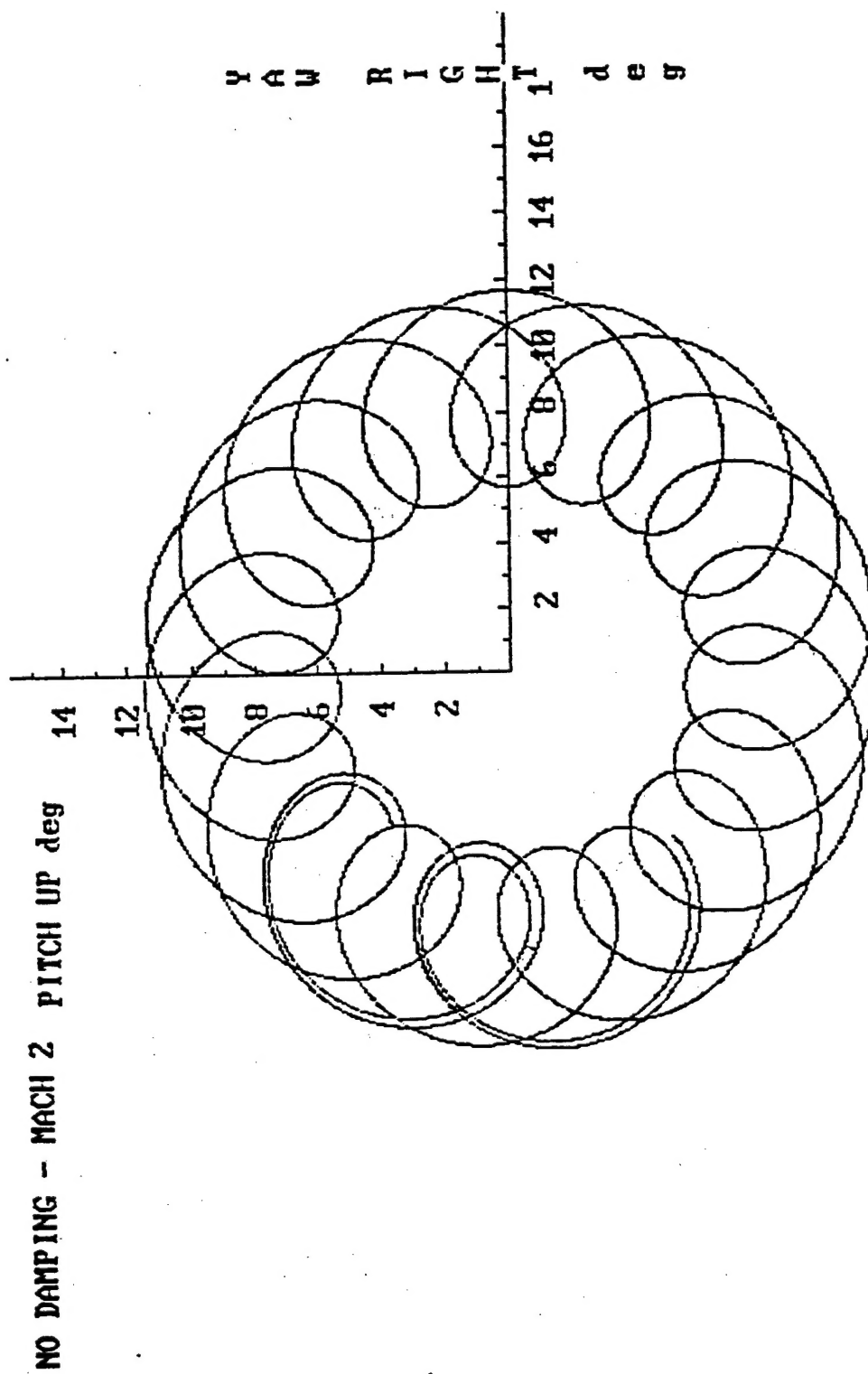


Figure 1 -- Undamped Motion for M107 at Mach 2 and +5 degrees and +5 Radians/sec Pitch and Yaw

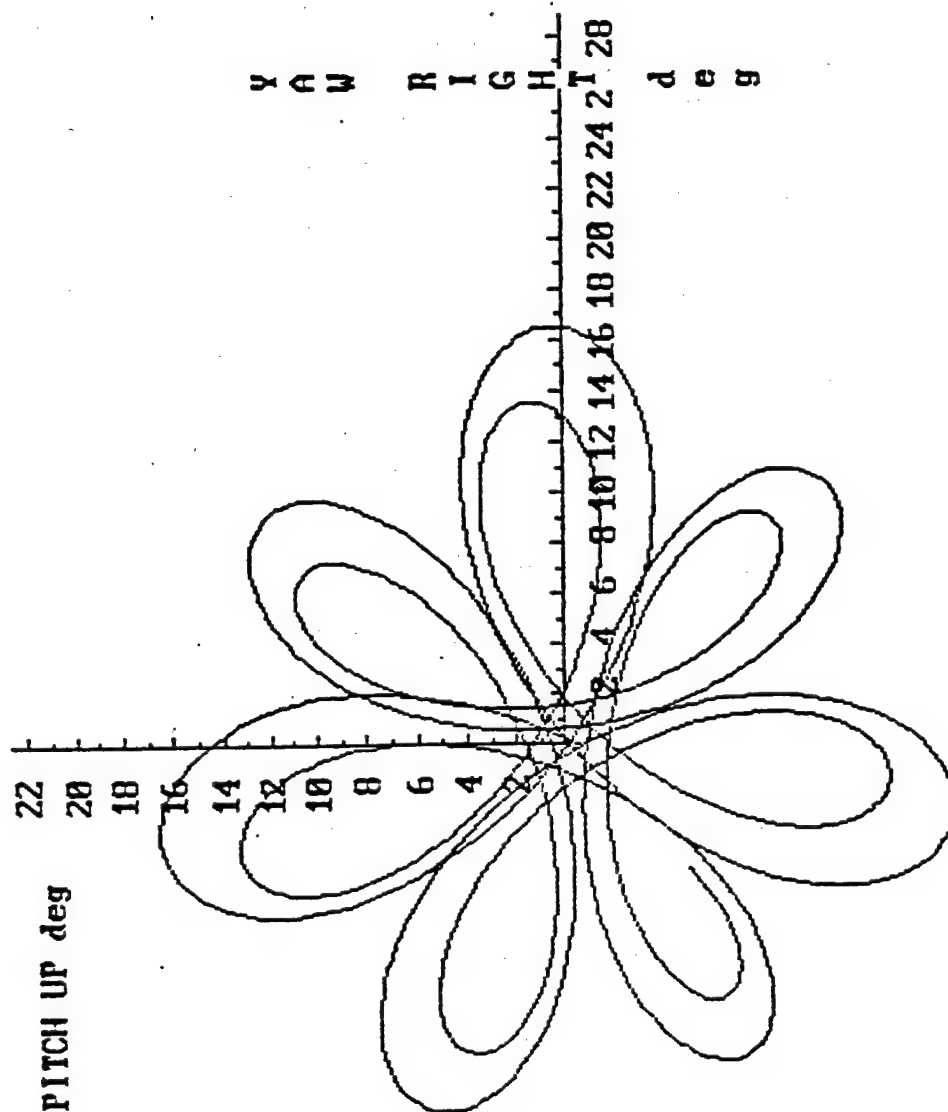


Figure 2 -- Epicycle Motion for Fin Stabilized Projectile with 50 Hz Spin Rate and +5 Degrees and +5 Radians/sec Initial Pitch and Yaw

SPIN-73
M107

TOTAL LENGTH	NOSE LENGTH	BOAT TAIL LENGTH	CG (FM NOSE)	WEPLATE DIAMETER	BAND DIAMETER	NOSE RADIUS	BOOM LENGTH							
4.510	2.450	0.450	2.960	0.088	1.020	10.750	0.000							
DIAMETER INCHES	IX LB-IN-SQ	IY LB-IN-SQ	WEIGHT LBS	GUN TWIST CAL/TURN	ACTUAL TWIST CAL/TURN	GUN-BORE INCHES	TEMPERATURE DEG-F	AIR DENSITY SLUGS/FT**3						
4.090	499.200	4311.000	95.000	20.000	20.197	4.150	59.000	0.00238						
AERODYNAMIC COEFFICIENTS														
MACH	CI	CI2	CMA	CMA	CPN	CTPA	CNPA3	CNPA5	CPF*1	CPF*5	CNPA*5	CND	CLP	
0.010	0.141	2.362	1.763	3.336	1.068	-0.767	-0.524	87.779	-840.289	2.277	3.312	0.270	-5.225	-0.030
0.600	0.141	2.362	1.763	3.338	1.056	-0.767	-0.524	87.779	-840.289	2.277	3.312	0.270	-5.225	-0.030
0.800	0.143	2.858	1.783	3.552	0.968	-0.767	-0.379	79.761	-760.111	2.465	3.406	0.342	-5.225	-0.028
0.900	0.161	3.371	1.831	3.898	0.831	-0.857	-0.139	58.213	-544.633	2.797	3.413	0.388	-7.533	-0.024
0.950	0.219	3.728	2.035	3.962	1.013	-1.082	0.050	45.686	-419.355	3.006	3.390	0.465	-9.961	-0.021
1.000	0.325	4.177	2.151	3.770	1.208	-0.992	0.166	31.153	-274.033	3.128	3.414	0.451	-13.892	-0.020
1.050	0.384	4.643	2.232	3.542	1.373	-0.902	0.265	18.626	-148.755	3.254	3.444	0.436	-13.436	-0.019
1.100	0.383	5.182	2.279	3.508	1.421	-0.857	0.307	13.113	-93.633	3.318	3.461	0.429	-14.661	-0.019
1.200	0.374	5.684	2.350	3.556	1.447	-0.767	0.328	9.205	-54.547	3.388	3.501	0.414	-15.845	-0.019
1.350	0.357	5.113	2.466	3.424	1.571	-0.767	0.342	7.601	-38.511	3.406	3.501	0.414	-15.861	-0.019
1.500	0.342	4.542	2.581	3.372	1.654	-0.767	0.349	6.799	-30.493	3.416	3.501	0.414	-15.343	-0.019
1.750	0.318	3.979	2.690	3.196	1.772	-0.767	0.357	5.998	-22.475	3.425	3.501	0.414	-15.343	-0.018
2.000	0.298	3.443	2.770	3.070	1.852	-0.767	0.364	5.196	-14.458	3.435	3.501	0.414	-15.343	-0.018
2.500	0.266	2.784	2.898	2.831	1.983	-0.767	0.371	4.394	-6.440	3.444	3.501	0.414	-15.343	-0.017
3.000	0.242	2.312	2.849	2.648	2.030	-0.767	0.378	3.592	1.578	3.454	3.501	0.414	-15.343	-0.016
4.000	0.204	1.890	2.749	2.638	2.000	-0.767	0.378	3.592	1.578	3.454	3.501	0.414	-15.343	-0.016
5.000	0.182	1.469	2.649	2.621	1.970	-0.767	0.378	3.592	1.578	3.454	3.501	0.414	-15.343	-0.016

STABILITY ANALYSIS

MACH	GYRO	SBAR	RECIP	SBAR*5	RECIP*5	SPIN	W1	W2	L1	L2	L1*5	L2*5	DELT	DISP
0.010	2.887	-0.124	-3.810	1.410	1.202	6.8	0.72	0.08-0.000363	0.000046-0.000081	-0.000236	0.4381	0.756		
0.600	2.868	-0.124	-3.810	1.410	1.202	410.7	42.97	4.59-0.000364	0.000046-0.000081	-0.000236	0.0073	0.750		
0.800	2.710	0.164	3.323	1.550	1.433	547.6	56.90	6.52-0.000315	0.000004-0.000054	-0.000265	0.0055	0.705		
0.900	2.470	0.505	1.325	1.504	1.102	616.1	63.19	8.15-0.000317	0.000082-0.000121	-0.000279	0.0050	0.635		
0.950	2.430	0.686	1.110	1.190	1.037	650.3	66.54	8.77-0.000338	0.000159-0.000182	-0.000315	0.0047	0.676		
1.000	2.554	0.649	1.140	0.919	1.007	684.6	70.55	8.72-0.000441	0.000196-0.000337	-0.000301	0.0045	0.727		
1.050	2.718	0.765	1.858	0.932	1.005	718.8	74.70	8.53-0.000385	0.000243-0.000323	-0.000305	0.0042	0.797		
1.100	2.745	0.762	1.060	0.872	1.017	753.0	78.36	8.84-0.000415	0.000258-0.000372	-0.000302	0.0040	0.829		
1.200	2.708	0.747	1.068	0.820	1.033	821.5	85.33	9.79-0.000452	0.000266-0.000421	-0.000298	0.0037	0.848		
1.350	2.812	0.786	1.048	0.846	1.024	924.2	96.46	10.55-0.000438	0.000284-0.000412	-0.000310	0.0033	0.950		
1.500	2.855	0.823	1.032	0.877	1.015	1026.8	107.38	11.53-0.000422	0.000299-0.000399	-0.000322	0.0029	1.029		
1.750	3.012	0.947	1.024	0.894	1.011	1198.0	126.05	12.67-0.000418	0.000312-0.000397	-0.000332	0.0025	1.166		
2.000	3.134	0.866	1.018	0.907	1.009	1369.1	144.69	13.85-0.000414	0.000322-0.000396	-0.000340	0.0022	1.276		
2.500	3.401	0.892	1.012	0.926	1.005	1711.4	182.34	15.83-0.000410	0.000337-0.000395	-0.000351	0.0017	1.502		
3.000	3.634	0.894	1.011	0.923	1.006	2053.7	220.15	17.66-0.000407	0.000335-0.000395	-0.000347	0.0014	1.611		
4.000	3.650	0.886	1.013	0.915	1.007	2738.2	293.63	23.45-0.000408	0.000326-0.000395	-0.000339	0.0011	1.586		
5.000	3.673	0.876	1.016	0.905	1.009	3422.8	367.23	29.11-0.000408	0.000318-0.000396	-0.000330	0.0009	1.543		

- CND - Zero yaw axial force coefficient
- CL2 - Yaw axial force coefficient per sin² α
- CMA - Normal force coefficient derivative per sin α
- CMA - Pitching moment coefficient derivative per sin α
- CPN - Normal force center of pressure - calibers for nose
- CTP - Magnus force coefficient derivative per sin α
- CNPA - Zero yaw Magnus moment coefficient derivative per sin α
- CNPA3 - Cubic Magnus moment coefficient derivative per sin³ α
- CNPA5 - Quintic Magnus moment coefficient derivative per sin⁵ α
- CPF1 - Center of pressure of Magnus force at 1° yaw or less calibers from nose
- CPF5 - Center of pressure of Magnus force at 5° yaw, calibers from nose
- CNPA-5 - 5° - Secant slope of Magnus moment coefficient derivative (at 5° yaw) per sin α
- Cmq - Damping moment coefficient
- CLp - Spin deceleration coefficient

'Stability Analysis'

- GYRO Gyroscopic stability factor
- SBAR Dynamic stability factor at 1° yaw
- RECIP Dynamic reciprocal factor at 1° yaw
- SBAR*5 Dynamic stability factor at 5° yaw
- RECIP*5 Dynamic reciprocal factor at 5° yaw
- SPIN Spin rate, radians/second
- W1 Nutation frequency, radians/second
- W2 Precession frequency, radians/second
- L1 Nutation damping factor per foot @ 1° yaw
- L2 Precession damping factor per foot @ 1° yaw
- L1-5 Nutation damping factor per foot @5° yaw
- L2-5 Precession damping factor per foot @ 5° yaw
- DELT Integration time step, seconds (20 per nutation)
- DISP Dispersion factor per 5° first max yaw, mils

Table 1 -- Aerodynamic and Mass Properties of M107 Projectile

6.	REFERENCE DIAMETER (INCHES).....	6.0000
21.	AXIAL INERTIA (LB-IN ²).....	227.8000
22.	TRANSVERSE INERTIA (LB-IN ²).....	1833.0000
23.	PROJECTILE WEIGHT (LB).....	52.8900
	MACH NO	1.10 1.20 1.30 1.50 1.80 2.00 2.50 3.00 3.50 4.00 5.00
CI TOTAL	0.385 0.209 0.220 0.398 0.464 0.480 0.450 0.351 0.402 0.385 0.344 0.311 0.294 0.275 0.254	
CMA TOTAL	5.18 3.44 6.08 6.33 6.73 6.71 6.33 6.16 6.17 3.96 3.41 1.91 4.48 4.11 3.66	
CMA TOTAL	-0.37 -0.53 -0.94 -0.79 -1.71 -1.71 -1.56 -1.44 -1.23 -1.05 -0.59 -0.29 0.15 0.51 0.91	
CMD	-9 -9 -10 -20 -24 -26 -26 -24 -23 -23 -21 -20 -19 -18 -18	
CLIP FIN	-0.81 -0.49 -0.82 -0.89 -0.91 -0.90 -0.85 -0.80 -0.71 -0.65 -0.51 -0.42 -0.34 -0.27 -0.20	
CLD FIN	1.43 1.56 1.85 2.00 2.06 2.02 1.91 1.80 1.61 1.46 1.15 0.94 0.76 0.61 0.45	
CYPA	-0.640 -0.640 -0.640 -0.840 -0.720 -0.640 -0.640 -0.640 -0.640 -0.640 -0.640 -0.640 -0.640 -0.640 -0.640	
CNPA	-0.500 -0.500 -0.372 0.183 0.265 0.255 0.263 0.274 0.282 0.287 0.293 0.300 0.300 0.300 0.300	
CNP3	77.806 77.806 70.694 27.583 11.583 8.117 7.169 5.983 5.130 4.561 3.850 3.139 3.139 3.139 3.139	
CNP3	-740.56-740.56-669.44-238.33 -78.33 -43.67 -34.19 -22.33 -13.80 -8.11 -1.00 6.11 6.11 6.11 6.11	

Table 2 -- Mass Properties and Aerodynamic Coefficients for Finner Design

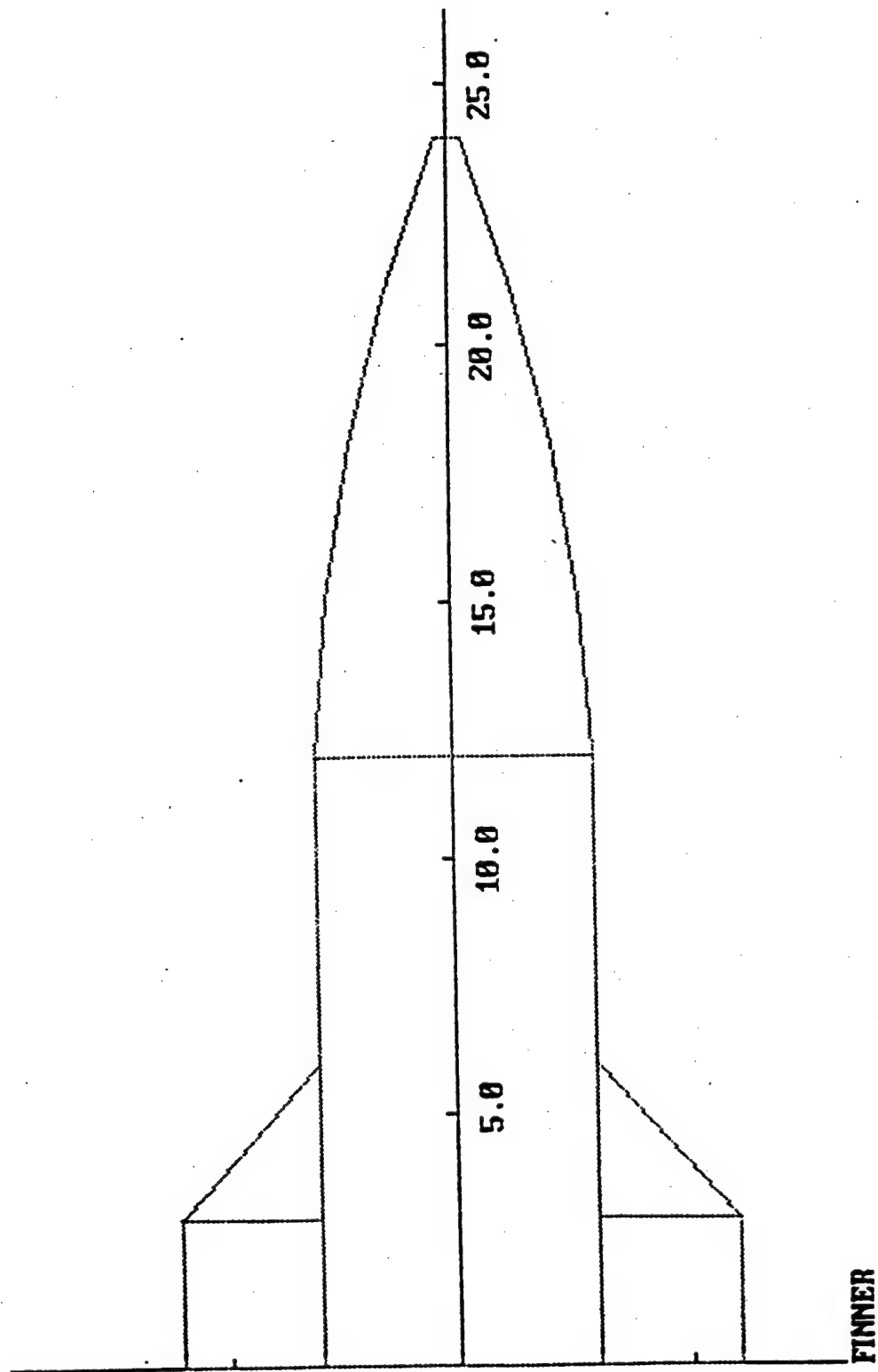


Figure 2.1 Generic Fin Stabilized Projectile Design

2.3 Determination of the Yaw Arms from the Superposition of the Nutation and Precession Angular Rates of Motion

Returning to Figures 1 and 2, one can imagine that as the nose of the projectile traces out its epicycle motion about the flight path of the projectile's center of gravity, the axis of the projectile is subjected to an ever changing angular rate of motion. This angular rate is the rate of change of the total angle of attack (total yaw angle) of the projectile. This rate shall be called Ω . The tip of the projectile, located at a distance X_{cg} from the center of gravity of the projectile, which is also the center of the epicycle motion, therefore, has an instantaneous tangential speed defined by:

$$S_{tip} = \Omega * X_{cg} \quad (1)$$

Through superposition of velocities of motion, one may also define this speed of the projectile tip, at any time, in terms of the nutation and precession yaw arms and rates of motion. The nutation and precession motions are both circular. The precession arm sweeps around a center located on the tangent to the flight path, and the nutation arm sweeps around a center located on the precession arm. The speed of each motion may be defined by:

$$S_{prec} = \Omega_{prec} * R_{prec} \quad (2)$$

and

$$S_{nut} = \Omega_{nut} * R_{nut} \quad (3)$$

If the directions of the nutation and precession speeds are known, vector addition would yield the tip speed at any time. However, at two points in the epicycle path, the nutation and precession velocities are parallel and, therefore, the speeds are fully superimposed. The nutation and precession velocities are in the same direction and, hence, additive at the maximum yaw and in opposite directions and, hence, differenced at the minimum yaw for the spin stabilized projectile. For the fin stabilized projectile, since the motion is prograde, the opposite is the case. At the minimum yaw, the speeds are additive, and at the maximum yaw they are differenced. Nevertheless, for both fin and spin stabilized projectiles, the maximum tip speed is the sum of the nutation and precession components, and the minimum tip speed is the difference between the two. Therefore:

$$S_{tip} |_{max} = S_{prec} + S_{nut} \quad (4)$$

and

$$S_{tip} |_{min} = S_{prec} - S_{nut} \quad (5)$$

Substituting (1), (2), and (3) into (4) and (5) gives the tip speed in terms of yaw arms and rates:

$$\Omega_{\max} * X_{cg} = \Omega_{\text{prec}} * R_{\text{prec}} + \Omega_{\text{nut}} * R_{\text{nut}} \quad (6)$$

and

$$\Omega_{\min} * X_{cg} = \Omega_{\text{prec}} * R_{\text{prec}} - \Omega_{\text{nut}} * R_{\text{nut}} \quad (7)$$

Dividing (6) and (7) by the center of gravity location gives the yaw arm relationships in terms of angles:

$$\Omega_{\max} = \Omega_{\text{prec}} * \alpha_{\text{prec}} + \Omega_{\text{nut}} * \alpha_{\text{nut}} \quad (8)$$

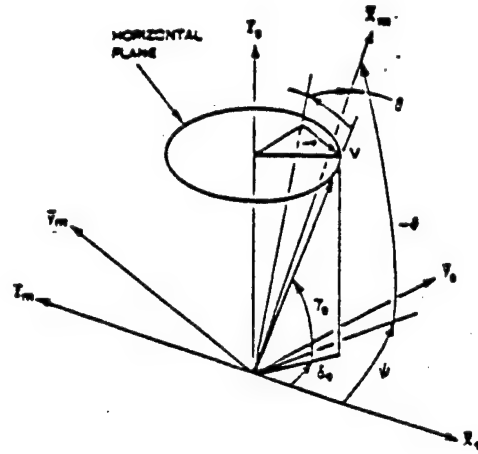
and

$$\Omega_{\min} = \Omega_{\text{prec}} * \alpha_{\text{prec}} - \Omega_{\text{nut}} * \alpha_{\text{nut}} \quad (9)$$

Given this last system of equations (8 and 9), if a sensor configuration can be developed which would measure the rate of change of total angle of attack, Ω , and the nutation and precession rates of motion, Ω_{nut} , and Ω_{prec} , the yaw arms α_{nut} and α_{prec} are readily calculated for both spin and fin stabilized projectiles. This approach, however, assumes that there are only two modes of motion -- nutation and precession. Any additional modes, caused by inertial imbalances in the projectile will have to be included in (8) and (9) with angular rate and yaw arm terms.

2.4 Determination of Yaw Arms from the Simultaneous Integration of Orthogonal Accelerations

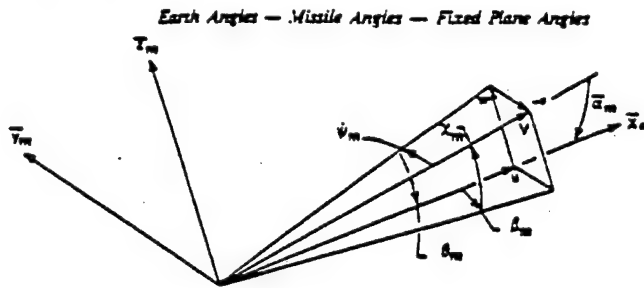
Another methodology for reducing sensor data into projectile pitch and yaw arms may be derived from the geometrical construction of the six-degree-of-freedom particle trajectory equations of motion. Figure 3 shows the missile velocity and missile angle geometrical relationships as defined in the trajectory model. The corresponding equations reveal that the missile pitch and yaw angles, Θ_m and Ψ_m , are direct functions of the orthogonal missile velocities, U, V, and W, and their vector sum, V_m . If these component velocities can be determined from telemetry data, it follows that the missile pitch and yaw angle history can be calculated, resulting in direct reconstruction of the epicycle motion of the projectile. The resulting data analysis will provide a graph similar to Figures 1 and 2.



$$\theta = \theta_m - \sin^{-1} \left[\sin \gamma_e / \cos \psi_m \right]$$

$$\psi = \sin^{-1} \left[\sin \psi_m / \cos \gamma_e \right] + \delta_e$$

NOTE: γ_m AND CORRESPONDING MISSILE VELOCITY v ARE CONSTRAINED TO THE EARTH HORIZONTAL PLANE.



NOTE: γ_m AND CORRESPONDING MISSILE VELOCITY v ARE CONSTRAINED TO THE EARTH HORIZONTAL PLANE.

Missile Velocities — Missile Angles

$$\dot{x} = u \cos \theta \cos \psi - v \sin \psi + w \sin \theta \cos \psi$$

$$\dot{y} = u \cos \theta \sin \psi + v \cos \psi + w \sin \theta \sin \psi$$

$$\dot{z} = -u \sin \theta + w \cos \theta$$

$$\dot{\theta} = q$$

$$\dot{\psi} = r / \cos \theta$$

$$\dot{\delta} = p + r \tan \theta$$

$$\dot{u} = g \sin \theta - qv + rv + F_x/m$$

$$\dot{v} = -ru - rv \tan \theta + F_y/m$$

$$\dot{w} = -g \cos \theta + rv \tan \theta + qu + F_z/m$$

$$\dot{p} = L/I_x$$

$$\dot{q} = -r^2 \tan \theta - I_x/I_y \, r p + M/I_y$$

$$\dot{r} = +qr \tan \theta + I_x/I_y \, q p + N/I_y$$

where:

$$F_x = \bar{q} A C_x$$

$$F_y = \bar{q} A \left[-C_{y\alpha} \frac{v}{V_A} + \frac{pd}{2V_A} C_{y\beta} \frac{v}{V_A} \right]$$

$$F_z = \bar{q} A \left[-C_{z\alpha} \frac{v}{V_A} - \frac{pd}{2V_A} C_{z\beta} \frac{v}{V_A} \right]$$

$$L = \bar{q} A d \left[\frac{pd}{2V_A} C_{lp} + C_{ls} \delta_s \right]$$

$$M = \bar{q} A d \left[C_{m\alpha} \frac{v}{V_A} + \frac{qd}{2V_A} C_{mq} + \frac{pd}{2V_A} C_{m\beta} \frac{v}{V_A} \right]$$

$$N = \bar{q} A d \left[-C_{n\alpha} \frac{v}{V_A} + \frac{rd}{2V_A} C_{nq} + \frac{pd}{2V_A} C_{n\beta} \frac{v}{V_A} \right]$$

$$\bar{q} = \frac{1}{2} \rho V_A^2$$

Figure 3 -- Velocity and Angle Relationships for 6-DOF Trajectory

$$\begin{aligned}
 w &= V_a \cos \psi_a \sin \theta_a \\
 v &= -V_a \sin \psi_a \\
 u &= V_a \cos \psi_a \cos \theta_a \\
 \phi &= 0.0 \\
 \theta &= \theta_a - \sin^{-1} \left[\sin \gamma_a / \cos \psi_a \right] \\
 \psi &= \sin^{-1} \left[\sin \psi_a / \cos \gamma_a \right] + \delta_a
 \end{aligned}$$

6-DOF Initial Conditions

NOMENCLATURE

A	Reference Area	\bar{q}	Dynamic pressure, lb/ft ²
C _{lp}	Spin Deceleration Coefficient	θ, ψ, ϕ	Fixed plane angles, radians
C _m	Pitching Moment Coefficient	g	Gravity
C _{mq}	Damping in Pitch Coefficient	X _a , Y _a , Z _a	Earth fixed distances, ft.
C _{mp}	Magnus Moment Coefficient	V _{Xa} , V _{Ya} , V _{Za}	Earth fixed velocities, ft/sec
C _N	Normal Force Coefficient	θ_a	Missile pitch angle, sin ⁻¹ $w/\sqrt{u^2 + w^2}$
C _{Np}	Magnus Force Coefficient	ψ_a	Missile yaw angle, sin ⁻¹ $-v/V$
C _X	Axial Force Coefficient	$\bar{\alpha}$	Missile total angle of attack, sin ⁻¹ $\sqrt{v^2 + w^2}/V$
I _x	Axial Moment of Inertia, slug-ft. ²	c	sin $\bar{\alpha}$
I _y	Transverse Moment of Inertia, slug-ft. ²	ρ	density, lb. sec ² /ft ⁴
V	Total Missile Velocity, ft/sec.	Superscripts	
VREF	Reference Velocity, ft/sec.	.	derivative with respect to time
u, v, w	Missile Fixed Velocities, ft/sec.	-	second derivative with respect to time
d	Reference Diameter	Subscript	
m	Mass, slugs	a	derivative with respect to sin α
p	Missile spin rate, rad/sec.	a	derivative with respect to sin ³ α
		a	derivative with respect to sin ³ α
		a ³	derivative with respect to sin ⁷ α
		a ⁷	derivative with respect to sin ² α
		2	derivative with respect to sin α

Figure 3 (a) -- Equations of Motion, Initial Conditions, and Nomenclature

Unfortunately, we know of no sensor which can directly measure velocity. However, velocity is only the first integral of acceleration, and we have accelerometers to work with. Therefore, for this telemetry scheme to be effective, accelerometers must be oriented within the projectile to provide \ddot{U} , \ddot{V} , and \ddot{W} . These accelerations may then be numerically integrated to provide the necessary velocity components at each time increment in the reconstruction. The reconstructed motion, however, will lack the initial angular conditions, or the constants of integration, so the pitch and yaw plot will be offset by these amounts. Nevertheless, the magnitude of the yaw arms will be apparent.

This technique is more versatile than the previous, since the nature of the motion is irrelevant. The integrated accelerations are orthogonal. Therefore, all motion is accounted for no matter how many modes are present. Nevertheless, the application of this technique will be shown to be restricted to only projectiles with known centers of gravity.

2.5 Determination of Yaw Arms from the Simultaneous Integration of Orthogonal Angular Rates

A third analysis methodology, similar to the previous technique, involves directly measuring the missile pitch and yaw angular rates, using orthogonal gyroscopes. These angular rate data are then numerically integrated to give the pitch and yaw angle histories for the flight. As with any integration scheme, the initial conditions may not be known, so the reconstructed motion is offset. Nevertheless, the yaw amplitudes will be easily recognizable from the plot.

This technique is the most versatile. It will account for all modes of motion, and projectile inertial properties and center of gravity may vary during flight. This technique, however, is the most demanding on the hardening requirements of the gyroscope sensor in order to survive launch accelerations.

2.6 Theoretical Sensor Configurations

There are several configurations, or families of configurations, of inertial components that can theoretically be employed in the measurement of the required pitch and yaw arms. Each of these has been considered and analyzed -- considering the accuracy, ease of construction, component requirements, cost, data reduction requirements, reliability, etc. The configurations that have been considered, and are analyzed in Section 3, are:

- ▶ RADIALLY ORIENTED ACCELEROMETERS TO MEASURE \dot{V} AND \dot{W}
- ▶ RADIALLY ORIENTED GYROSCOPES TO MEASURE $\dot{\theta}_m$ AND $\dot{\psi}_m$
- ▶ AXIALLY ORIENTED ACCELEROMETERS TO MEASURE \dot{U} AND THE RATE OF CHANGE OF TOTAL YAW ANGLE, Ω
- ▶ AXIALLY ORIENTED GYROSCOPE TO MEASURE Ω , THE RATE OF CHANGE OF THE TOTAL YAW ANGLE
- ▶ SENSOR CONFIGURATIONS TO DETERMINE THE ROLL ORIENTATION OF A HIGH SPIN RATE SHELL
- ▶ AN ALTERNATE SENSOR CONFIGURATION FOR DETERMINING ROLL ORIENTATION OF A HIGHLY VARIABLE FIN-STABILIZED PROJECTILE
- ▶ ACCELEROMETER CONFIGURATIONS FOR DETERMINING THE NUTATION AND PRECESSION RATES OF MOTION

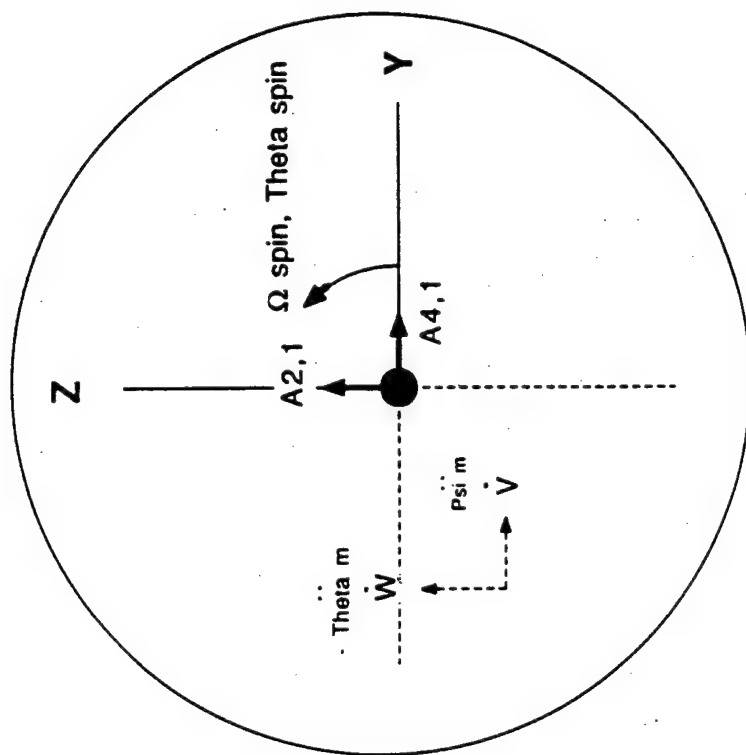
3.0 Methods, Assumptions and Procedures

3.1 General

The methods that were used to perform the analysis and to ultimately reach the tradeoffs and conclusions involved first examine the output characteristics of each of the sensors that appear in the candidate configurations, and to then look at the appropriate data demodulation and analysis techniques that may be applicable to this sensor. This permits us to arrive at the advantages and limitations of each configuration, and to thereby reach a conclusion or series of conclusions relating to each telemetry concept.

3.2 Radially Oriented Accelerometers to Measure \dot{V} and \dot{W}

Figure 4 shows a configuration of radially oriented accelerometers, which will allow extraction of the \dot{V} and \dot{W} missile accelerations. This configuration requires two orthogonal radial accelerometers, A_{21} and A_{41} , located at a known distance X_{cg1} from the projectile center of gravity, and a second, parallel set, A_{22} and A_{42} , located at another known distance X_{cg2} from the center of gravity. As shown by the equations defining each measured acceleration output, two sets



$$A2 = - (X_1 \Theta_m'' - W') \cos(\Theta_{spin}) - (X_1 \Psi_m'' + V') \sin(\Theta_{spin})$$

$$A4 = - (X_1 \Theta_m'' - W') \sin(\Theta_{spin}) - (X_1 \Psi_m'' + V') \cos(\Theta_{spin})$$

Figure 4 -- Radially Oriented Accelerometer Configuration for Determining \dot{V} and \dot{W}

are required in order to separate the acceleration contributions of \dot{V} and \dot{W} , which we want, from the effects of the missile pitch and yaw angular accelerations, $\ddot{\theta}_m$ and $\ddot{\psi}_m$, which results from the axial location of the sensor package from the missile center of gravity.

Note that each acceleration component is modulated by the spin rate or the relative roll orientation angle, as defined by the sine and cosine terms. Since the projectile is spinning, the orientation of the accelerometers is constantly changing with respect to the pitching and yawing accelerations. The total acceleration is always being measured by the vector sum of each pair of accelerometers. However, in order to isolate \dot{V} and \dot{W} for integration, each accelerometer output must be decomposed into orthogonal components with respect to an arbitrary initial roll orientation angle. Determining this relative roll orientation angle history from telemetry is a later topic in this section of the report.

3.3 Radially Oriented Gyroscopes to Measure $\dot{\theta}_m$ and $\dot{\psi}_m$

Figure 5 shows a schematic of a simple spring restrained rate gyroscope. As the inertia wheel J spins about the axis 2-3, this axis will precess at a rate ω about axis 1-2 in response to a force F parallel to axis 1-2. Conversely, a force F will be generated in response to a rotation of the axis 2-3 about axis 1-2. Similarly, if the axis 2-3 was forced to rotate in the plane 1-2-3, a force would be generated perpendicular to this plane (going into or out of the page, not shown), and this force would be proportional to the angular rate of motion. If axis 1-2 represents the longitudinal axis of the projectile, plane 1-2-3 represents the pitch or yaw plane of motion, and point 1 was the projectile center of gravity, it follows that a force F perpendicular to the plane 1-2-3 would be generated as a result of the pitching or yawing rate of the projectile nose about the projectile center of gravity. It is the measurement of this force which gives the pitching or yawing rate to be integrated to yield the pitch and yaw angles.

Figure 6 shows two radially oriented gyroscopes, configured to measure the pitch and yaw angular rates during projectile flight. Axis U is the missile longitudinal axis about which the sensor package spins. Axes V and W are orthogonal and perpendicular to axis U. It is in the Plane V-W that the pitch and yaw motion to be measured takes place. As each gyroscope aligns with axis W, one output, F2, measures angular rate ω_2 . This same output, when the gyroscope aligns with axis V, measures angular rate ω_3 . When the gyroscopes are oriented between each of these axes, this output measures a combination of the sine and cosine components of rates ω_2 and ω_3 . Therefore, the rate output from each of the perpendicular gyroscopes is orthogonal, as shown in

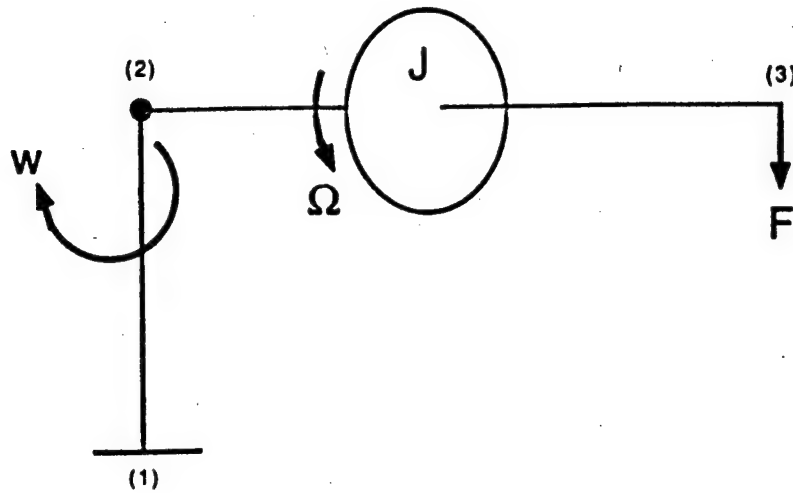


Figure 5 -- Schematic of a Simple Rate Gyroscope

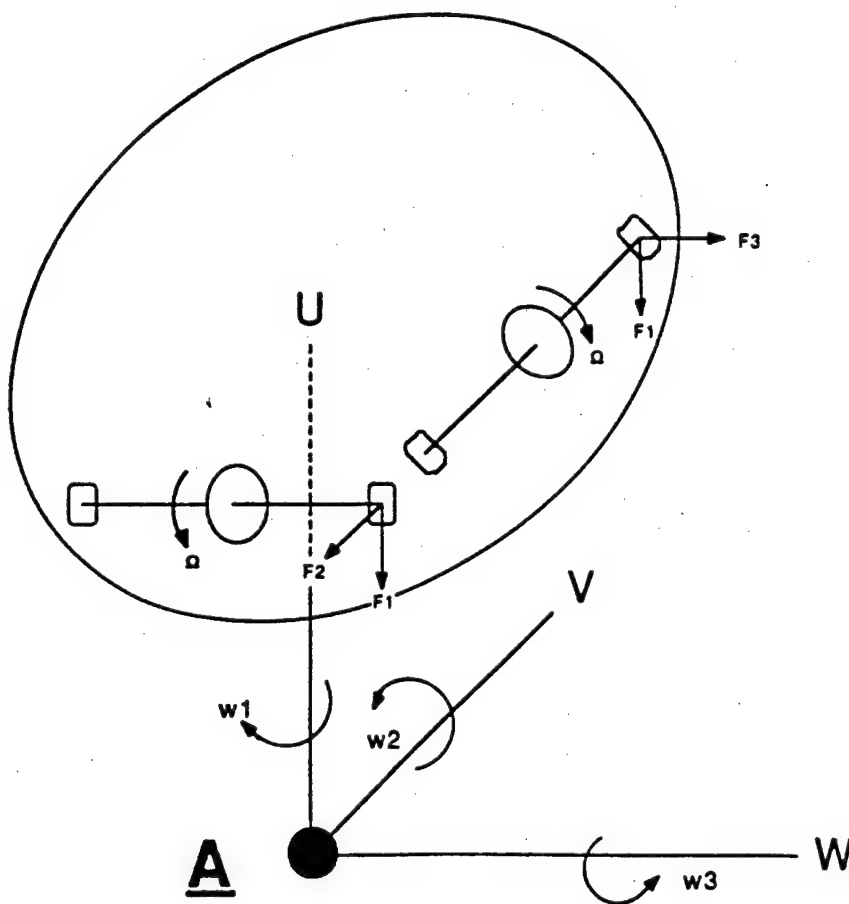


Figure 6 -- Gyroscope Based Telemetry Configuration for Determining Missile Pitch and Yaw Angular Rates

the following equations:

$$\text{Output 1} = \omega_2 \sin(\omega_1 t) + \omega_3 \cos(\omega_1 t) \quad (10)$$

$$\text{Output 2} = \omega_2 \cos(\omega_1 t) - \omega_3 \sin(\omega_1 t) \quad (11)$$

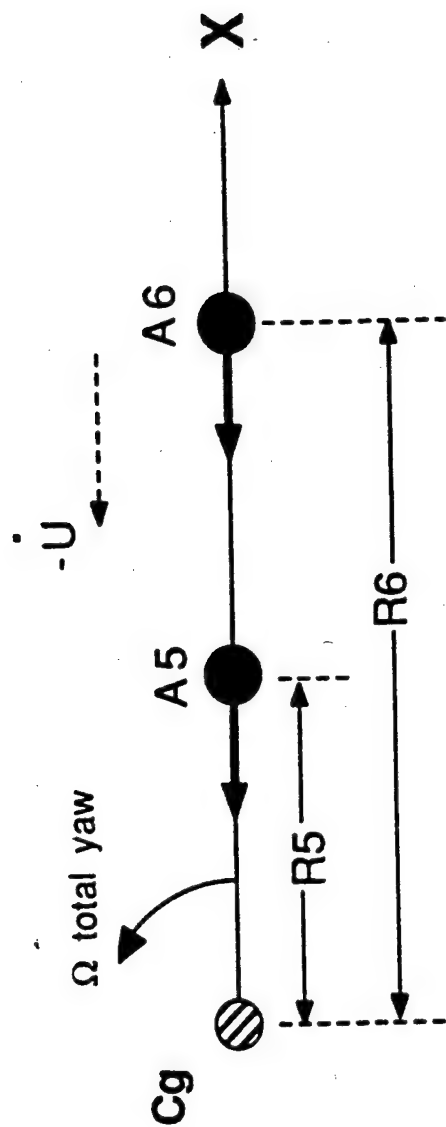
As with the accelerometer scheme previously discussed, roll orientation will be required, in order to decompose the gyroscope outputs into orthogonal components of pitch and yaw angular rates, prior to integration. (The additional output, F1, shown in Figure 6 allows measurement of the inertial spin rate of the projectile, ω_1 .)

3.4 Axially Oriented Accelerometers to Measure \dot{U} and the Rate of Change of Total Yaw Angle

Figure 7 shows that if two axially oriented accelerometers are positioned a known distance from the projectile center of gravity, \dot{U} is readily calculated from the accelerometer outputs. We see from these equations the restricted application of this configuration to projectiles with known center of gravity during flight. If the center of gravity shifts after launch, measurement of \dot{U} is not possible because the axial distance of the sensor from the center of gravity is now unknown. As a byproduct of this configuration, if the two accelerometers are separated by a known distance D , as shown in Figure 7, the rate of change of the total angle of attack, $\dot{\Omega}$, is readily calculated from the accelerometer outputs, regardless of Cg position.

3.5 Axially Oriented Gyroscope to Measure $\dot{\Omega}$, the Rate of Change of the Total Yaw Angle

Figure 8 shows a two axis rate gyroscope oriented parallel to the projectile longitudinal axis. If the plane of pitch angle is the page, and the plane of yaw angle is perpendicular to the page, as the projectile pitches and yaws, the outputs F2 and F3 will measure these angular rates. As the projectile spins about its axis, the orientation of these outputs will change and each output will measure a component of both the pitch and yaw rate, based on the sine and cosine of the inertial roll angle. However, the vector sum of each output is always the vector sum of the pitch and yaw rates, which is the rate of change of total yaw angle, regardless of the roll orientation of the gyroscope. Therefore, the rate of change of total angle of attack is simply the square root of the sum of the squares of both rate outputs. The result can be seen by performing this algebraic operation on equations 10 and 11.



$$D = R6 - R5$$

$$A5 = \Omega^2 R5 - \dot{U}$$

$$A6 = \Omega^2 R6 - \dot{U}$$

$$\Omega = ((A6 - A5)/D)^{1/2}$$

Figure 7 -- Accelerometer Configuration for Determining \dot{U} and Rate of Change of Total Yaw Angle, Ω

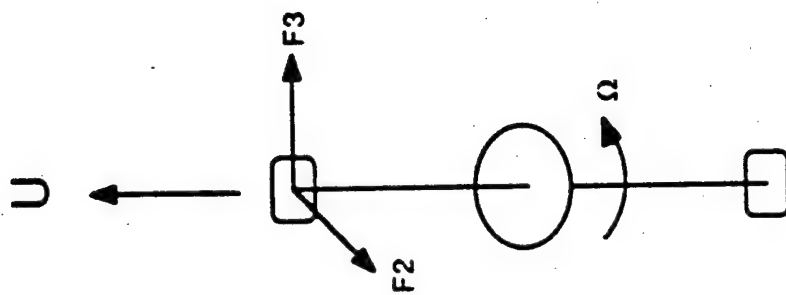


Figure 8 -- Axially Oriented Gyroscope Configuration for Measuring Total Yaw Angular Rate

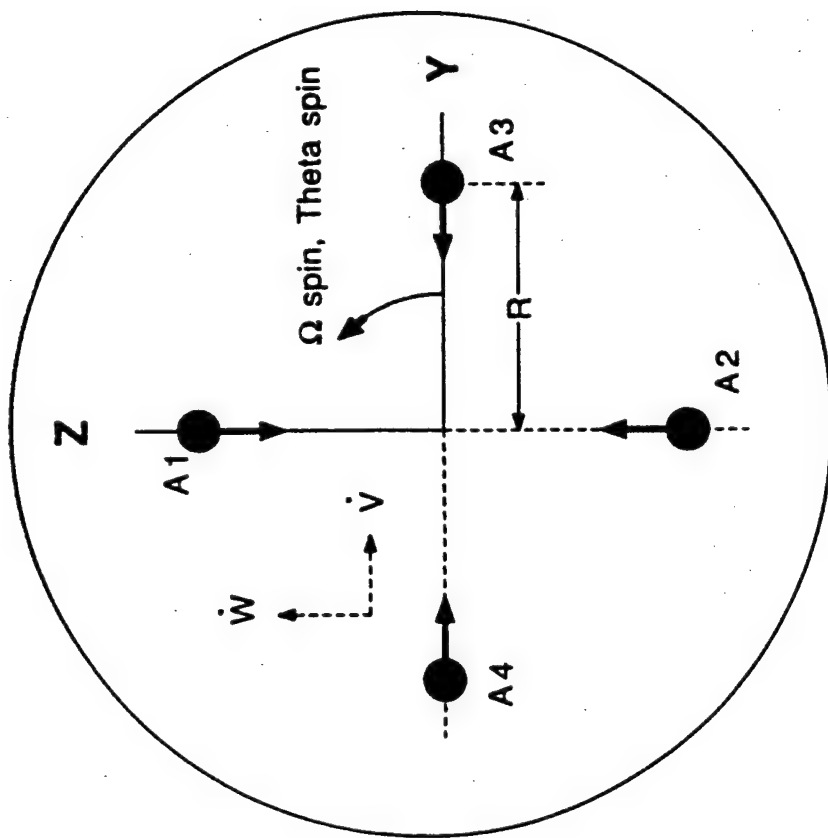
3.6 Sensor configurations for determining roll orientation of a high spin rate shell

In order to decompose radially oriented accelerometer or gyroscope outputs into their orthogonal components in the plane of pitch and yaw, prior to numerical integration, a relative inertial roll orientation angle must be known over the flight time of interest. We postulated that the requirement for knowing a relative inertial roll orientation of the projectile could be satisfied by accurately measuring the inertial spin rate. For high spin rate shells, with little spin damping, it may be practical to then assume a constant spin rate or a small linear decay of spin rate over the short period of time during which the epicycle motion would be reconstructed. Of course, analysis has to be performed to see how accurately the spin rate must be known, in order to accurately reconstruct the epicycle motion.

The inertial spin rate is most easily measured by placing a radially oriented accelerometer a known distance from the axis of spin and measuring the centripetal acceleration due to rotation. However, this accelerometer will also measure the angular acceleration due to the pitching and yawing motion of the axial location of the sensor. Therefore, as shown in Figure 9, an additional accelerometer will be required, oriented 180 degrees apart. The sum of the outputs from these two radially oriented accelerometers is then directly proportional to twice the spin rate. The inertial spin rate can also be directly measured from the output of a radially oriented rate gyroscope. Figure 6 shows that the gyroscope output $F1$ is proportional to the spin rate $w1$, regardless of the roll orientation of the radially oriented gyroscope.

3.7 Alternate sensor configuration for determining roll orientation of a highly variable spin fin-stabilized shell

Since fin stabilized projectiles are subjected to high spin damping and acceleration rates within even a few nutation cycles, the technique of assuming a constant or near constant spin rate with which to calculate a relative roll orientation angle is not practical. The nature of sensor scale factor errors also precludes the use of simple numerical integration of the spin rate output over time to get the relative roll angle. The scale factor error associated with an accelerometer or gyroscope can only be mitigated if the acceleration or rate being measured oscillates, as in the case of the pitch and yaw angle rates and accelerations, which vary from very small values to very large values and then change direction. In the case of measuring a spin rate, however, all motion is in one direction and either increasing or decreasing, but not oscillating. The result is that the errors associated with scale factors continuously accumulate, and after a few rotations, the total error is enormous, making the integrated roll



$$A1 = \Omega^2 R + (X_1 \Theta_m'' - W') \cos(\Theta_{spin}) + (X_1 \Psi_m'' + V') \sin(\Theta_{spin})$$

$$A2 = \Omega^2 R - (X_1 \Theta_m'' - W') \cos(\Theta_{spin}) - (X_1 \Psi_m'' + V') \sin(\Theta_{spin})$$

$$A3 = \Omega^2 R + (X_1 \Theta_m'' - W') \sin(\Theta_{spin}) - (X_1 \Psi_m'' + V') \cos(\Theta_{spin})$$

$$A4 = \Omega^2 R - (X_1 \Theta_m'' - W') \sin(\Theta_{spin}) - (X_1 \Psi_m'' + V') \cos(\Theta_{spin})$$

Figure 9 -- Alternate Radially Oriented Accelerometer Configuration for Determining \dot{V} , \dot{W} , and Inertial Spin Rate

angle meaningless.

To overcome this problem, a unique approach was hypothesized, which involves using an accelerometer to measure the acceleration due to the downward gravity vector, and thus establish an absolute vertical each rotation of the projectile. By knowing the time difference between successive vertical passings, the roll rate of the projectile is corrected after each cycle and no errors can accumulate. Roll orientation during the interval can then be accurately determined. If successful, this technique provides a means of determining roll orientation for both fin and spin stabilized projectiles.

This technique is theoretically possible, since an accelerometer, as a spring-mass device, measures the force due to an acceleration, rather than the acceleration itself. For example, if an accelerometer is at rest on a table, it measures 1 g, despite the fact that there is no actual change in velocity of the point on the table where the accelerometer is located. On the other hand, an accelerometer in free fall in a vacuum will measure zero acceleration, despite the fact that it is falling at 32.17 ft/sec². Therefore, a vertically oriented accelerometer, mounted in a projectile in free flight, will always measure an acceleration due to gravity, in addition to many other accelerations, unless the location of the accelerometer is accelerating downward 1 g, at which time gravity has zero contribution to the measured acceleration.

The result of this characteristic of the accelerometer is that as the projectile spins, a radially oriented accelerometer will measure 1 g modulated by the roll orientation angle times the eulerian pitch angle of the projectile axis plus any other accelerations occurring at the location of the accelerometer:

$$\text{Acel measured} = 1 \text{ g} * \sin(P*t) * \sin(\Theta) + \text{Acel(others)} \quad (12)$$

where

P = spin rate

Θ = Eulerian pitch angle

Acel(others) = other accelerations along the sensitive axis of the accelerometer (e.g. $\ddot{\Theta}_m$, $\ddot{\Psi}_m$, \dot{V} , \dot{W})

Granted, the contribution of gravity to the measured acceleration is very small compared to the other accelerations which affect the projectile flight and yawing motion. However, the frequency at which these other accelerations occur is different from the frequency at which the gravity contribution occurs (i.e. the spin rate P). Although the amplitudes of the other accelerations can be several orders of magnitude greater than 1 g, as long as they occur at different frequencies, the frequency of the 1 g contribution can be isolated from the

accelerometer output. The electronic mechanism for isolating this spin rate frequency may be an analog filter bank, an FFT (Fast Fourier Transform) or a Phase Locked Loop (PLL) filter. All three mechanisms will spectrally filter out the roll motion using the fact that it is at a different frequency than the pitch and yaw accelerations of the projectile. In addition, these mechanisms will be able to track the spin rate as it varies during flight.

An alternate perspective on how the spin rate can be isolated from the radially oriented accelerometer output by isolating the g vector is to consider a mechanical analogy to the electronic filtering mechanism. The electronic filter can be considered a tuned mass oscillator (i.e. a spring with stiffness K and a mass M), which has a resonant frequency set to the spin rate of the projectile (i.e. $P = \sqrt{K/M}$). The g vector is then a forcing function at frequency P , the spin rate, in the form $F = g \sin(P \cdot t)$. The tuned oscillator, whose natural frequency is P , will always resonate at the frequency P in the presence of this forcing function, regardless of the presence of any other forcing functions at other frequencies, even if the other functions are at much greater amplitude. Monthly report number 4 gives an in-depth presentation of the mechanics of a tuned mass oscillator.

3.8 Accelerometer configurations for determining the nutation and precession rates of motion

Research performed by Mishra, Harrison, and Hepner⁶ showed that an accelerometer mounted on a spinning and coning platform measured peak accelerations at a characteristic frequency equal to the spin rate minus the coning rate. This finding is consistent with the expected frequency of radial alignment for circular, single-mode, prograde motion. Although the epicycle motion of spin and fin stabilized projectiles, as presented earlier, is dual-mode, and both prograde and retrograde, respectively, the characteristic rates of motion -- spin, nutation, and precession -- should appear in accelerometer traces in some form or another, as reported in Reference 6. The challenge will be to find the proper accelerometer orientations within the projectile, and to develop the data reduction techniques to isolate the characteristic frequencies.

3.9 Methodology for Amplitude Demodulating Sensor Outputs

After deriving the sensor configurations to achieve the necessary measurements, it is necessary to process the data in order to obtain the required motion. This has been done by various techniques, which are suitable for different situations and conditions. The demodulation techniques that have been applied are both AM and FFT based. These techniques are illustrated in

the following examples and analysis.

a) For Undamped Epicycle Motion of Spin Stabilized Projectile

In order to proceed with the analysis, the characteristics of the M107 projectile have been applied, although the results are applicable to any spin stabilized projectile. Figure 1 shows the undamped motion for an M107 projectile with launch conditions of Mach 2, +5 degrees pitch and yaw, and +5 radians/sec pitch and yaw rates. This motion is undamped in that the only aerodynamic force acting on the projectile is the pitching moment, characterized by the coefficient CMA. The expected spin, nutation, and precession rates for this projectile at this muzzle velocity are 1369.1, 144.8, and 13.8 radians/sec, respectively, as shown in Table 1. Figure 10 shows the change in the projectile total angle of attack over a .7 second portion of time during the simulation. This graph is generated from the pitch and yaw angle history calculated in the 6-DOF computer model, and the maximum and minimum values in this curve are what is to be determined by the data reduction in the yaw sensing telemetry. The characteristic frequency of the trace in Figure 10 is nearly exactly the nutation-precession frequency, 131 radians/sec, which is to be expected in prograde motion, but this rate is only arrived at by performing a moving average of several individual peak-to-peak and min-to-min cycles. There is considerable spread in the individual cyclic rates, indicating that there is additional modulation in the motion. This data reduction technique would be considered an A.M. demodulation of the signal.

Figure 11 shows the expected acceleration trace from one radially oriented accelerometer as calculated using the 6-DOF model for the undamped motion in Figure 1. It clearly shows two dominant frequencies. The fast mode is the continuous solid line traced by the measured acceleration, and the slower mode is represented by the large empty valleys between local maxima in the data. Performing a moving average of many individual fast mode cycles in this trace gives a rate of 1223.4 radians/sec. The data averaged to get this rate is very choppy, however, as shown in Table 3. This is partly due to the sharpness of the maximum and minimum points in the curve, and the integration time step of the model. Analysis of zero crossings, where the curve is very steep and without a sharp change in direction, gives more smoothness to the data, as shown in Table 4. The average rate is nearly the same, but the data clearly shows additional modulation about this average. This rate is also nearly the expected spin rate minus the nutation rate ($1369.1 - 144.8 = 1224.3$).

Figure 12 shows the vector sum of two orthogonal radial accelerometers, as configured in Figure 4. Each accelerometer gives a similar trace to Figure 11, but with a 90 degree phase shift due to their orientation. Therefore, taking the square root of the sum of the squares of each acceleration value eliminates the fast mode seen in Figure 11, and isolates the slow mode seen as voids in

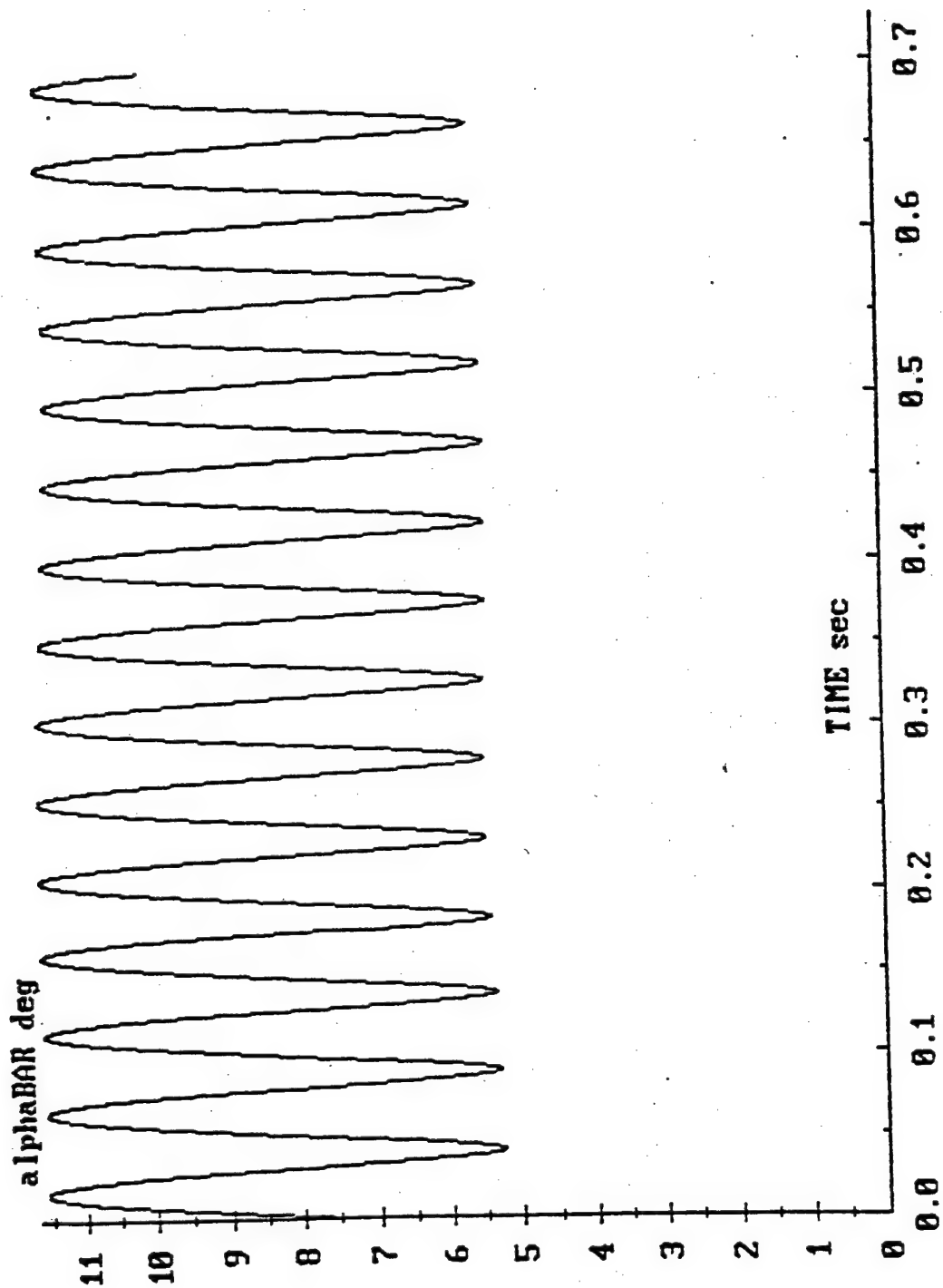


Figure 10 -- Total Yaw Angle History for Figure 1

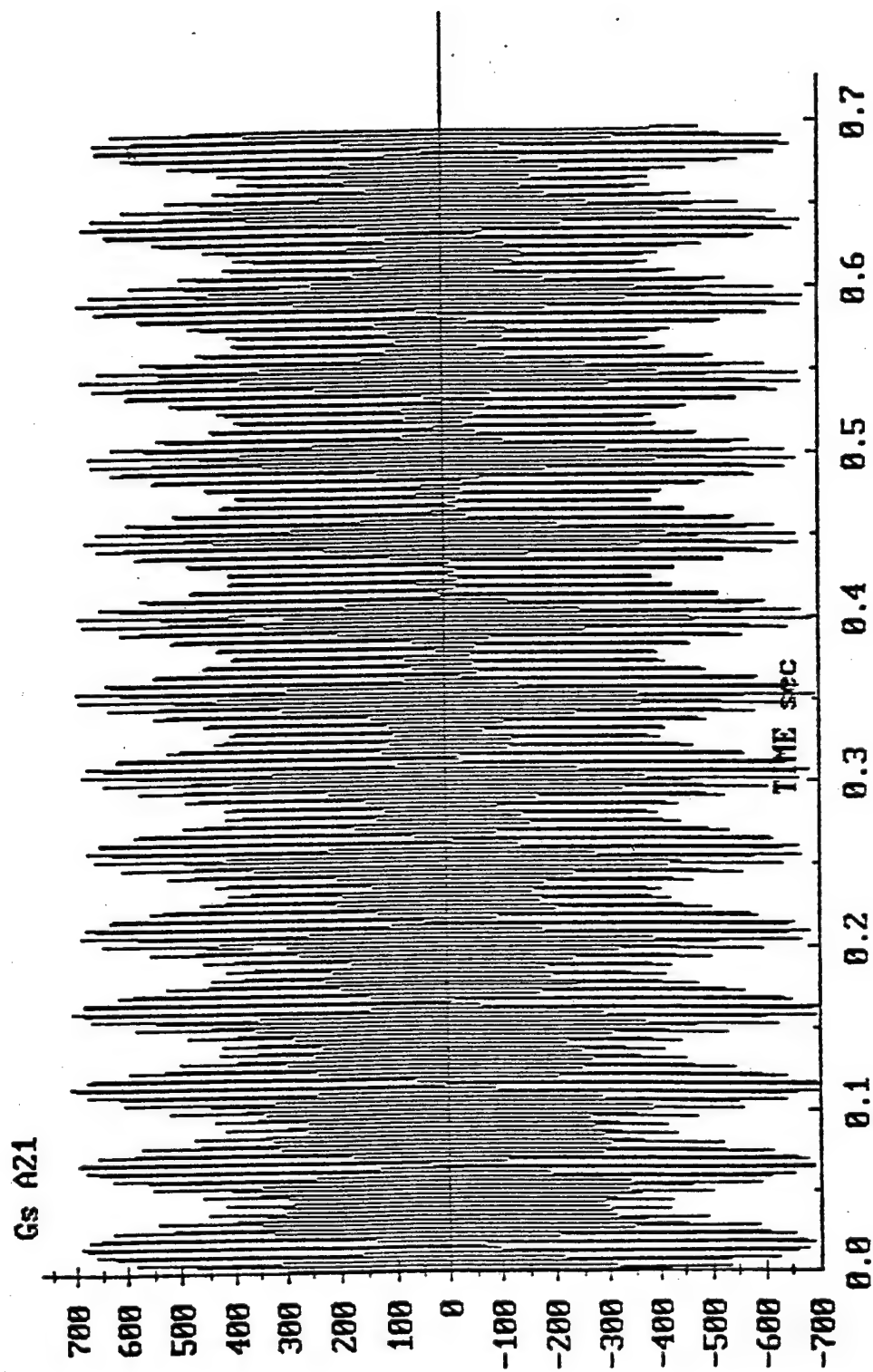


Figure 11 -- Output from One Radial Accelerometer for Figure 1

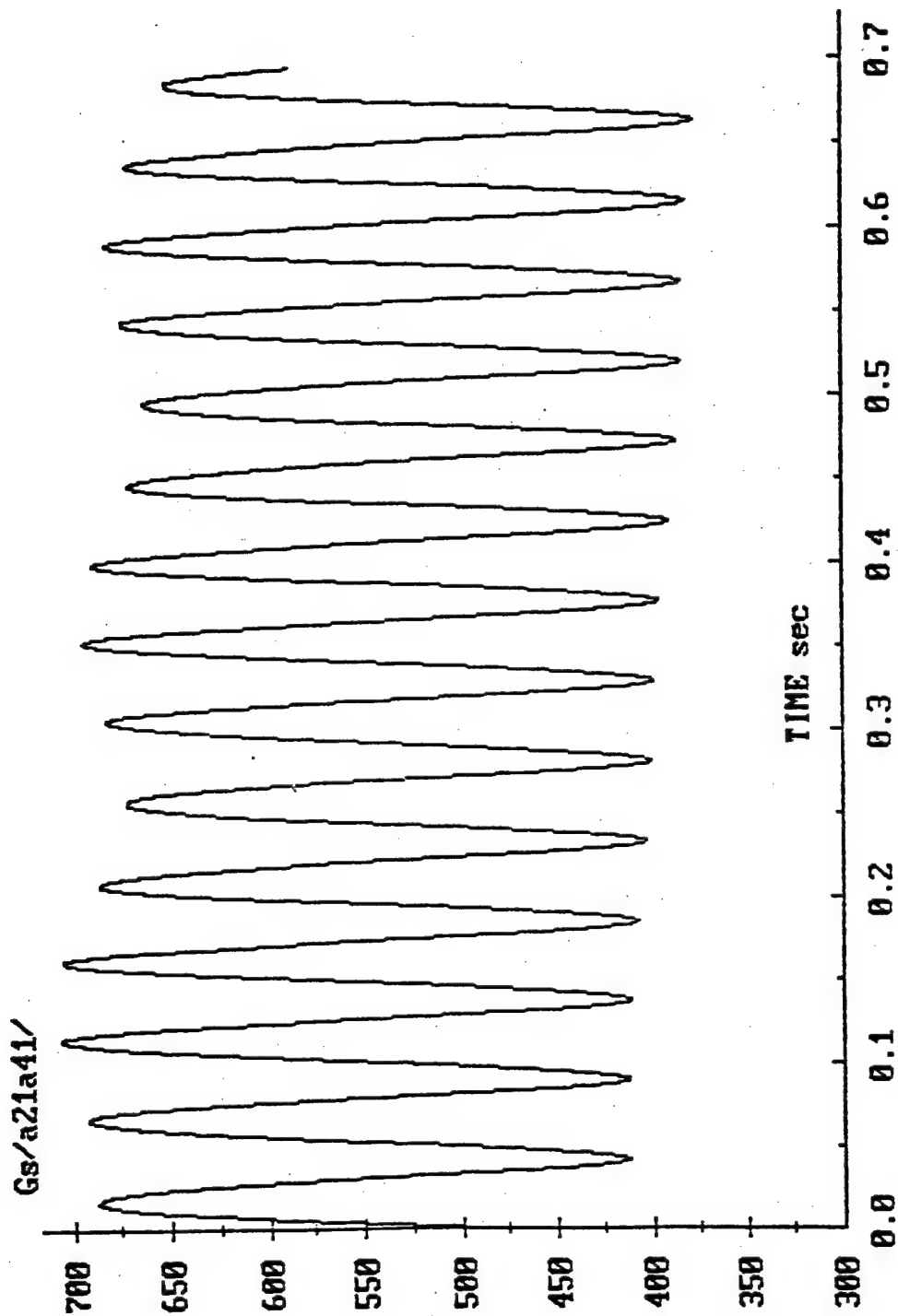


Figure 12 Vector Sum of Two Orthogonal Radial Accelerometers for Figure 1

MAX	MIN	AVG	MAXIMUMS: AVG DELTA TIME, .005200	AVG RATE (RAD/S)
.00600	486.2773	.003200	-487.4365	1208.303892
.005800	493.8347	.005100	-505.1206	1231.996125
.010900	519.5625	.008300	-535.2141	1231.996125
.016000	551.5291	.013500	-567.7187	1231.996125
.021100	580.2079	.018600	-588.0468	1231.996125
.026200	588.6087	.023700	-580.1792	1208.303892
.031300	565.9134	.028800	-545.2135	1231.996125
.036400	523.9108	.033900	-503.4265	1231.996125
.041600	485.7041	.039000	-472.3070	1231.996125
.046800	464.1365	.044200	-461.5940	1208.303892
.052000	464.5447	.049400	-473.0831	1208.303892
.057100	486.0358	.054500	-502.1603	1231.996125
.062300	519.4730	.059700	-536.9193	1231.996125
.067400	551.2826	.064800	-559.8096	1231.996125
.072500	560.5910	.069900	-554.4261	1208.303892
.077600	540.5734	.075000	-524.4756	1231.996125
.082700	505.4368	.080100	-487.1962	1208.303892
.087800	470.7083	.085200	-456.4928	1231.996125
.093000	445.9360	.090400	-440.0867	1231.996125
.098200	439.5662	.095600	-444.5503	1231.996125
.103400	454.6881	.100800	-468.9766	1208.303892
.108500	486.7127	.105900	-503.9791	1231.996125
.113600	517.1849	.111100	-526.5664	1231.996125
.118700	527.9048	.116200	-524.0700	1231.996125
.123800	514.7224	.121300	-502.3549	1208.303892
.128900	487.7259	.126400	-472.5741	1208.303892
.134100	456.4877	.131500	-442.1200	1231.996125
.139200	430.1429	.136600	-421.4987	1208.303892
.144400	417.4617	.141800	-418.8899	1231.996125
.149600	426.0446	.147000		1208.303892

20 POINT MOVING AVERAGE

MAXIMUMS: AVG DELTA TIME, .005137

MINIMUMS: AVG DELTA TIME, .005137

29 POINT MOVING AVERAGE

MAXIMUMS: AVG DELTA TIME, .005136

MINIMUMS: AVG DELTA TIME, .005136

Table 3 -- Amplitude and Rate Output for One Radial Accelerometer for Figure 1 Motion

Table 3 -- Amplitude and Rate Output for One Radial Accelerometer for Figure 1 Motion

ZEROS:	DELTA TIME,	RATE (RAD/S)
	.005125	1226.077067
	.005081	1236.490315
	.005052	1243.593240
	.005036	1247.744364
	.005027	1249.780321
	.005025	1250.447919
	.005026	1250.088999
	.005032	1248.527968
	.005046	1245.199580
	.005070	1239.403054
	.005106	1230.536127
	.005156	1218.549048
	.005217	1204.395552
	.005277	1190.652354
	.005317	1181.811349
	.005316	1181.937808
	.005275	1191.130362
	.005213	1205.233694
	.005153	1219.274348
	.005106	1230.505390
	.005074	1238.410321
	.005052	1243.658261
	.005038	1247.124141
	.005030	1249.257436
	.005026	1250.113350
	.005029	1249.413497
	.005040	1246.737729
	.005060	1241.672868
	.005092	1234.004678
	.005135	1223.653614
	.005188	1211.043367
	.005247	1197.542752
	.005297	1186.141942
	.005319	1181.241447
	.005300	1185.531486
	.005249	1196.959800
	.005190	1210.516173

AVERAGE RATE =	1233.90274928600000
MAX --	1250.44791911690000 MIN --
	1181.24144743600000

Table 4 -- Zero Crossings and Rates from One Radial Accelerometer for Figure 1 Motion

Figure 11. A moving average of the peak-to-peak and min-to-min cycles in Figure 12 gives the expected nutation minus precession rate of 131 radians/sec. This is consistent with the observed frequency in the angle of attack history, Figure 10.

A additional observation to be made using the results of the undamped motion is the profound oscillation in the maximum values in Figure 12. Isolating the slow mode motion in Figure 11, which resulted in Figure 12, has brought out an unseen third slower mode riding on the crests of the acceleration trace in Figure 12. There is not enough of a density of data points in Figure 12 to allow direct extraction of the peaks and valleys in this surface wave. Therefore, in order to accurately determine a local maximum or minimum in the cycle, the five or six points surrounding each maximum or minimum were used as the basis for a discrete polynomial interpolation, which was then evaluated at a much smaller time increment. Figure 12 shows two clear intervals between maximum values, and one clear interval between minimums. Using the interpolation routine to find more accurate peaks and valleys, the angular rates for the two maximum cycles are 27.49 and 27.98 radians/sec, respectfully, and the rate for the one minimum cycle is 27.69 radians/sec. These three rates average to 27.72, which is for all intents and purposes twice the precession rate (i.e. 27.6).

This method of isolating the spin-nutation, nutation-precession, and precession rate was retested by running the simulation at Mach 3 conditions, where the spin, nutation, and precession rates are considerably different from the Mach 2 conditions (see Table 1). We had the same results. Spin-nutation is isolated by one radially oriented accelerometer. Nutation-precession is isolated in the vector sum of two orthogonal radially oriented accelerometers, and the waviness at the top of the latter acceleration curve is twice the precession rate.

The moment of inertia values for this projectile were then changed and the center of gravity shifted rearward, in order to increase the nutation and precession rates with respect to the spin rate. The spin rate of the projectile was also decreased to further enhance this effect. These changes were made to test this analysis technique on a much less stable projectile configuration. Table 5 shows the aerodynamic and stability parameters employed in the six-degree-of-freedom simulation. Damping was turned off and the muzzle velocity was chosen as Mach 4, giving a projectile spin rate of 1369.1 radians/sec. The expected nutation rate for these launch conditions increases to 263.12 and the expected precession rate becomes 54.54 radians/sec. Figure 13 shows the resulting epicyclic motion of the projectile with initial conditions of +5 degrees and +5 radians/sec in both the pitch and yaw directions.

SPIN-73
IX>>IY

TOTAL LENGTH	NOSE LENGTH	BOAT TAIL LENGTH	CG (FM NOSE)	MEPLATE DIAMETER	BAND DIAMETER	NOSE RADIUS	BOOM LENGTH
4.510	2.450	0.450	4.000	0.088	1.020	10.750	0.000

DIAMETER INCHES	IX LB-IN-SQ	IY LB-IN-SQ	WEIGHT LBS	GUN TWIST CAL/TURN	ACTUAL TWIST CAL/TURN	GUN-BORE INCHES	TEMPERATURE DEG-F	AIR DENSITY SLUGS/FT**3
6.090	1000.000	4310.000	95.000	40.000	40.394	6.150	59.000	0.00238

AERODYNAMIC COEFFICIENTS														
MACH	CX	CX2	CNA	CNA	CPN	CYPA	CNPA	CNPA3	CNPA5	CPF*1	CPF*5	CNPA*5	CN2	CLP
0.010	0.141	2.362	1.763	5.169	1.068	-0.767	-1.321	87.779	-840.289	2.277	3.312	-0.527	10.549	-0.030
0.600	0.141	2.362	1.763	5.191	1.056	-0.767	-1.321	87.779	-840.289	2.277	3.312	-0.527	10.549	-0.030
0.800	0.143	2.858	1.783	5.407	0.968	-0.767	-1.177	79.761	-760.111	2.465	3.406	-0.455	10.549	-0.028
0.900	0.161	3.371	1.831	5.902	0.831	-0.957	-1.030	58.213	-544.533	2.797	3.413	-0.503	7.711	-0.024
0.950	0.219	3.728	2.035	6.078	1.013	-1.082	-1.075	45.686	-419.355	3.096	3.390	-0.660	5.177	-0.021
1.000	0.325	4.177	2.151	6.008	1.208	-0.992	-0.865	31.153	-274.033	3.128	3.414	-0.591	1.140	-0.020
1.050	0.386	4.663	2.232	5.863	1.373	-0.902	-0.673	18.626	-148.755	3.254	3.444	-0.502	1.437	-0.019
1.100	0.383	5.192	2.279	5.978	1.421	-0.857	-0.584	13.113	-93.633	3.318	3.461	-0.462	0.141	-0.019
1.200	0.374	5.684	2.350	6.000	1.447	-0.767	-0.469	9.205	-54.547	3.388	3.501	-0.383	-1.485	-0.019
1.300	0.357	5.113	2.466	5.988	1.571	-0.767	-0.455	7.601	-38.511	3.406	3.501	-0.383	-3.950	-0.019
1.500	0.342	4.542	2.591	6.057	1.654	-0.767	-0.448	6.799	-30.493	3.416	3.501	-0.383	-8.452	-0.019
1.750	0.318	3.979	2.690	5.994	1.772	-0.767	-0.441	5.998	-22.475	3.425	3.501	-0.383	-8.452	-0.018
2.000	0.299	3.443	2.770	5.951	1.852	-0.767	-0.433	5.196	-14.458	3.435	3.501	-0.383	-8.452	-0.018
2.500	0.266	2.784	2.998	5.545	1.983	-0.767	-0.426	4.394	-6.440	3.444	3.501	-0.383	-8.452	-0.017
3.000	0.242	2.312	2.849	5.611	2.030	-0.767	-0.419	3.592	1.578	3.454	3.501	-0.383	-8.452	-0.016
4.000	0.204	1.990	2.749	5.496	2.000	-0.767	-0.419	3.592	1.578	3.454	3.501	-0.383	-8.452	-0.016
5.000	0.182	1.469	2.649	5.376	1.970	-0.767	-0.419	3.592	1.578	3.454	3.501	-0.383	-8.452	-0.016

STABILITY ANALYSIS														
MACH	GYRO	SBAR	RECIP	SBAR*5	RECIP*5	SPIN	W1	W2	L1	L2	L1*5	L2*5	DELT	DISP
0.010	1.869	0.514	1.309	-0.506	-0.789	3.4	0.67	0.13	0.000188	0.000019	0.000355	-0.000148	0.4702	0.412
0.600	1.861	0.514	1.309	-0.506	-0.789	205.4	40.03	7.62	0.000189	0.000019	0.000356	-0.000149	0.0078	0.409
0.800	1.787	0.518	1.869	-0.616	-0.621	273.8	52.85	10.69	0.000222	-0.000017	0.000378	-0.000173	0.0059	0.388
0.900	1.665	0.192	2.887	-1.028	-0.321	308.1	58.33	13.15	0.000141	-0.000033	0.000261	-0.000153	0.0054	0.350
0.950	1.590	0.465	1.401	-3.882	-0.044	325.2	60.70	14.75	0.000027	-0.000021	0.000125	-0.000119	0.0052	0.350
1.000	1.608	0.456	1.421	1.211	1.047	342.3	64.13	15.29	-0.000097	-0.000040	-0.000031	-0.000106	0.0049	0.360
1.050	1.648	1.079	1.006	1.572	1.486	359.4	67.83	15.55	-0.000038	-0.000096	0.000001	-0.000135	0.0046	0.380
1.100	1.644	0.961	1.001	1.199	1.041	376.5	71.01	16.34	-0.000072	-0.000109	-0.000044	-0.000136	0.0044	0.389
1.200	1.610	0.901	1.010	1.021	1.000	410.7	76.98	18.31	-0.000114	-0.000126	-0.000094	-0.000146	0.0041	0.390
1.300	1.614	0.708	1.093	0.777	1.052	462.1	86.66	20.55	-0.000216	-0.000116	-0.000199	-0.000133	0.0036	0.418
1.500	1.595	0.513	1.312	0.553	1.250	513.4	95.94	23.18	-0.000409	-0.000082	-0.000394	-0.000098	0.0033	0.435
1.750	1.612	0.551	1.253	0.586	1.207	599.0	112.30	26.67	-0.000403	-0.000097	-0.000390	-0.000110	0.0028	0.469
2.000	1.623	0.580	1.214	0.610	1.179	684.6	128.63	30.20	-0.000399	-0.000108	-0.000387	-0.000120	0.0024	0.496
2.500	1.653	0.621	1.167	0.647	1.143	855.7	161.66	36.88	-0.000392	-0.000125	-0.000382	-0.000135	0.0019	0.545
3.000	1.722	0.619	1.169	0.641	1.148	1026.8	196.26	41.99	-0.000387	-0.000125	-0.000379	-0.000134	0.0016	0.579
4.000	1.758	0.605	1.185	0.626	1.162	1369.1	263.12	54.54	-0.000388	-0.000117	-0.000380	-0.000125	0.0012	0.585
5.000	1.797	0.597	1.206	0.608	1.181	1711.4	330.77	66.31	-0.000388	-0.000109	-0.000380	-0.000117	0.0009	0.588

Table 5 -- Aerodynamic, Mass, and Stability Parameters for Modified Projectile

The trace from one radially oriented accelerometer is shown in Figure 14. The vector sum of two orthogonal radial accelerometers is shown in Figure 15, and the angle of attack history from the simulation is plotted in Figure 16. Performing a moving average on the accelerometer trace in Figure 14 gives an average rate of about 1105.3 radians/sec, which is nearly the expected spin-nutation rate of 1105.98. Analysis of zero crossings showed nothing different from what has been reported in the previous analysis. The average rate for the trace in Figure 14 is about 210.5, which is close to the expected nutation-precession rate of 208.58. Analysis of the slow mode surface wave on top of the acceleration trace in Figure 14 shows two peak-to-peak cycles and two min-to-min cycles. Using interpolation to find the relative mins and maxs, and averaging each rate yields a half-cycle frequency of 51.54 rads/sec, which is nearly the expected precession rate of 54.54 rads/sec.

b. For Damped Epicycle Motion of Spin Stabilized Projectile

This same technique was applied to the analysis of the traces from a damped simulation, to see the effect on detecting the characteristic rates of motion. Figure 17 shows the damped epicyclic motion of the M107 projectile, for the initial conditions of Mach 2, +5 degrees pitch and yaw, and +5 radians/sec pitch and yaw rates. Figure 18 is the trace of one radially oriented accelerometer. Figure 19 shows the vector sum of two orthogonal radial accelerometers. Figure 20 shows the angle of attack history from the simulation.

Repeating the technique, the fast mode frequency is isolated by performing a moving average of the peak-to-peak intervals between local maxima and minima in Figure 18. For this projectile, the fast mode is expected to be 1224.3 radians/sec, which is the difference between the spin and nutation rates (1369.1 and 144.8 rads/s, respectfully). A 19 point moving average of Figure 18 gives a consistent rate of 1224 rads/s, which is nearly exactly what is expected. The data, however, which forms the basis for the moving average is very choppy, as previously reported, but smoothes out when analyzing zero crossings. A moving average of the trace in Figure 19 also gives the expected nutation minus precession rate of 131 radians/sec.

Whereas the slow mode trace in the undamped simulation (Figure 12) showed a clear surface wave riding on the peak values, in Figure 19, the corresponding damped motion trace, the surface wave is much more subtle. Figure 21 shows the damped acceleration trace in Figure 19 with the peak values connected by straight lines. There is clearly an oscillation on top of the steadily decreasing peak amplitudes. This oscillation is not as clean as in the undamped case (see Figure 12), and all of the peak values are less than the previous one, so simply interpolating relative maxima and minima is not

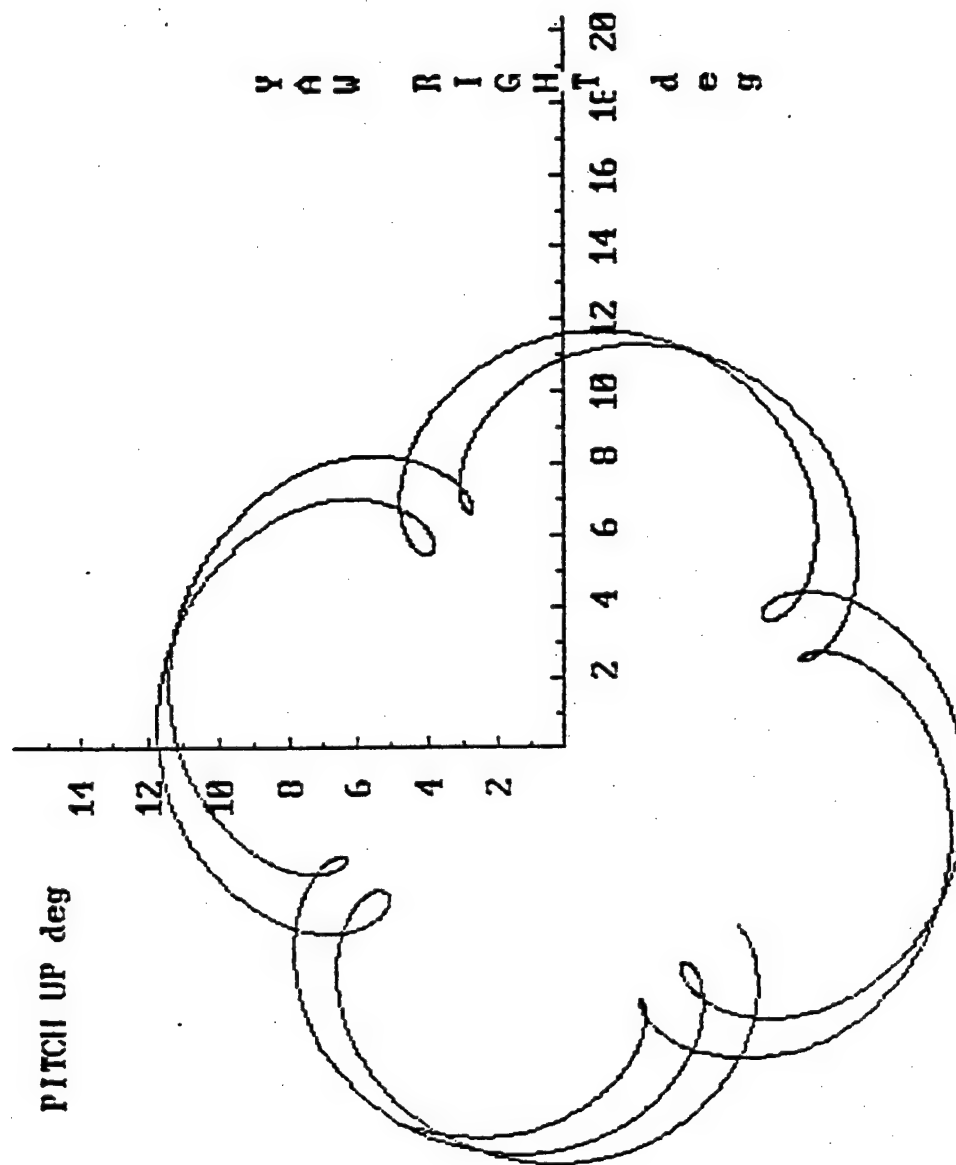


Figure 13 -- Undamped Motion for Modified Projectile with the same Initial Conditions as Figure 1

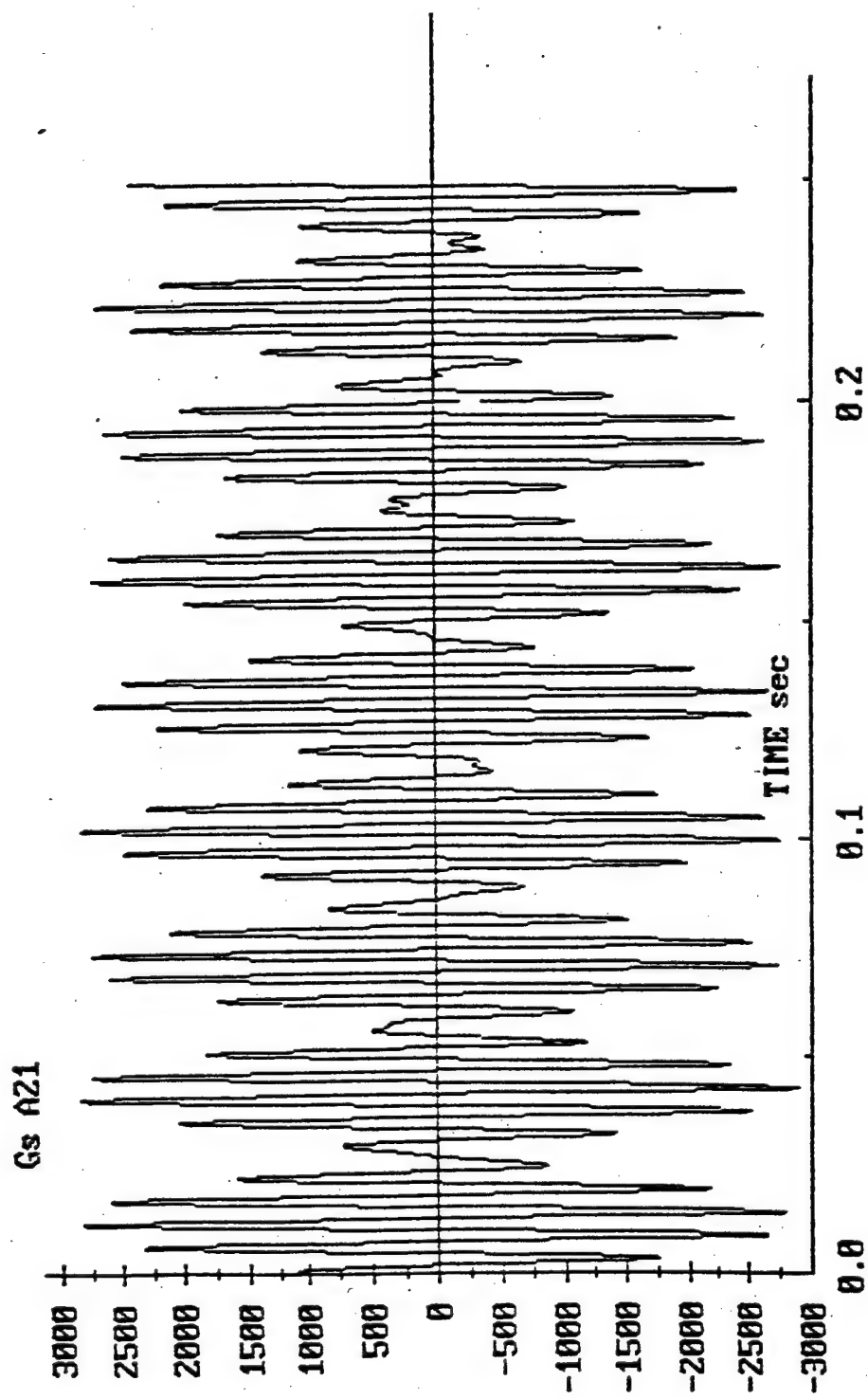


Figure 14 -- Output from One Radial Accelerometer for Figure 13

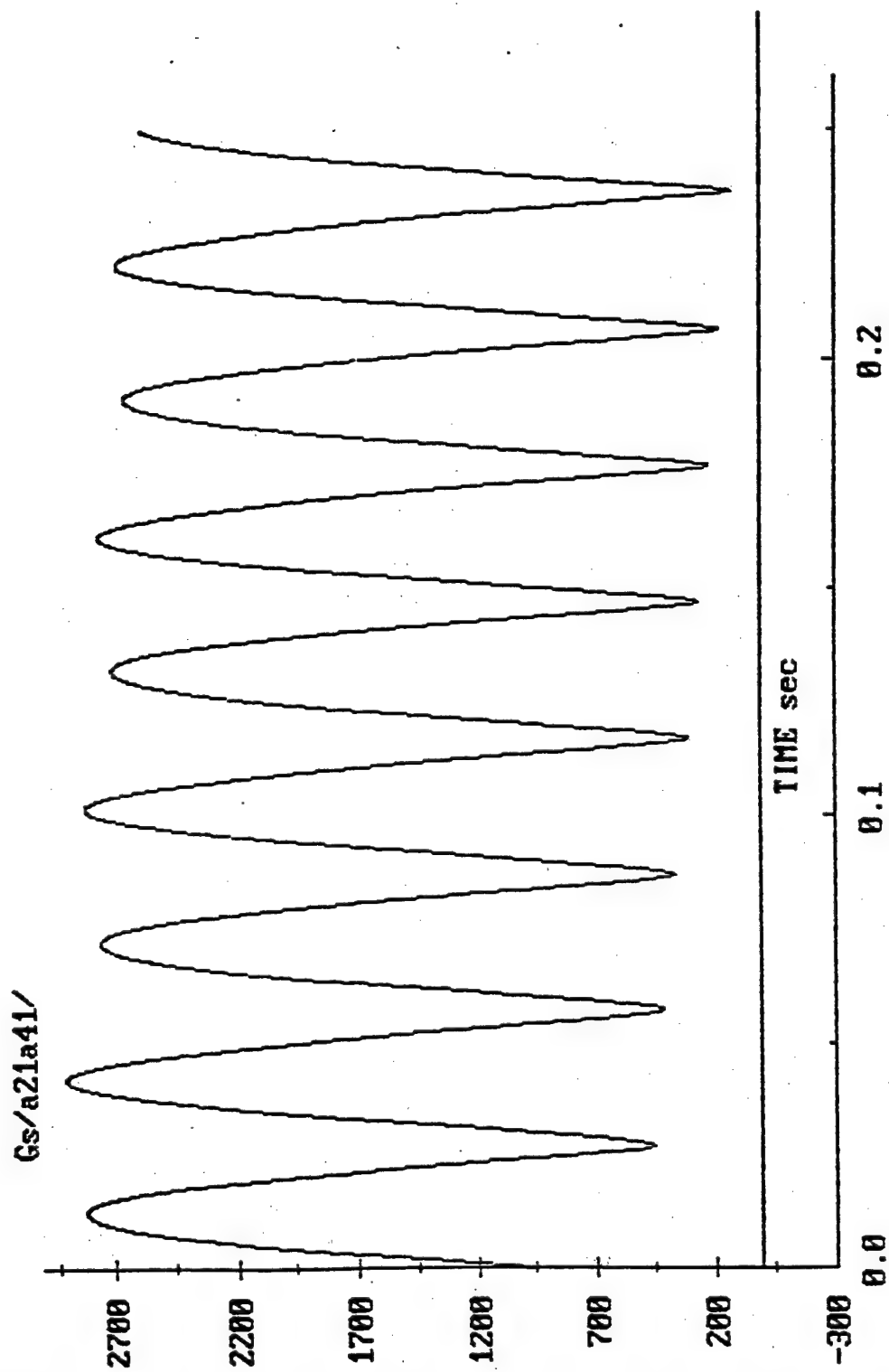


Figure 15 -- Vector Sum of Two Orthogonal Radial Accelerometers for Figure 13

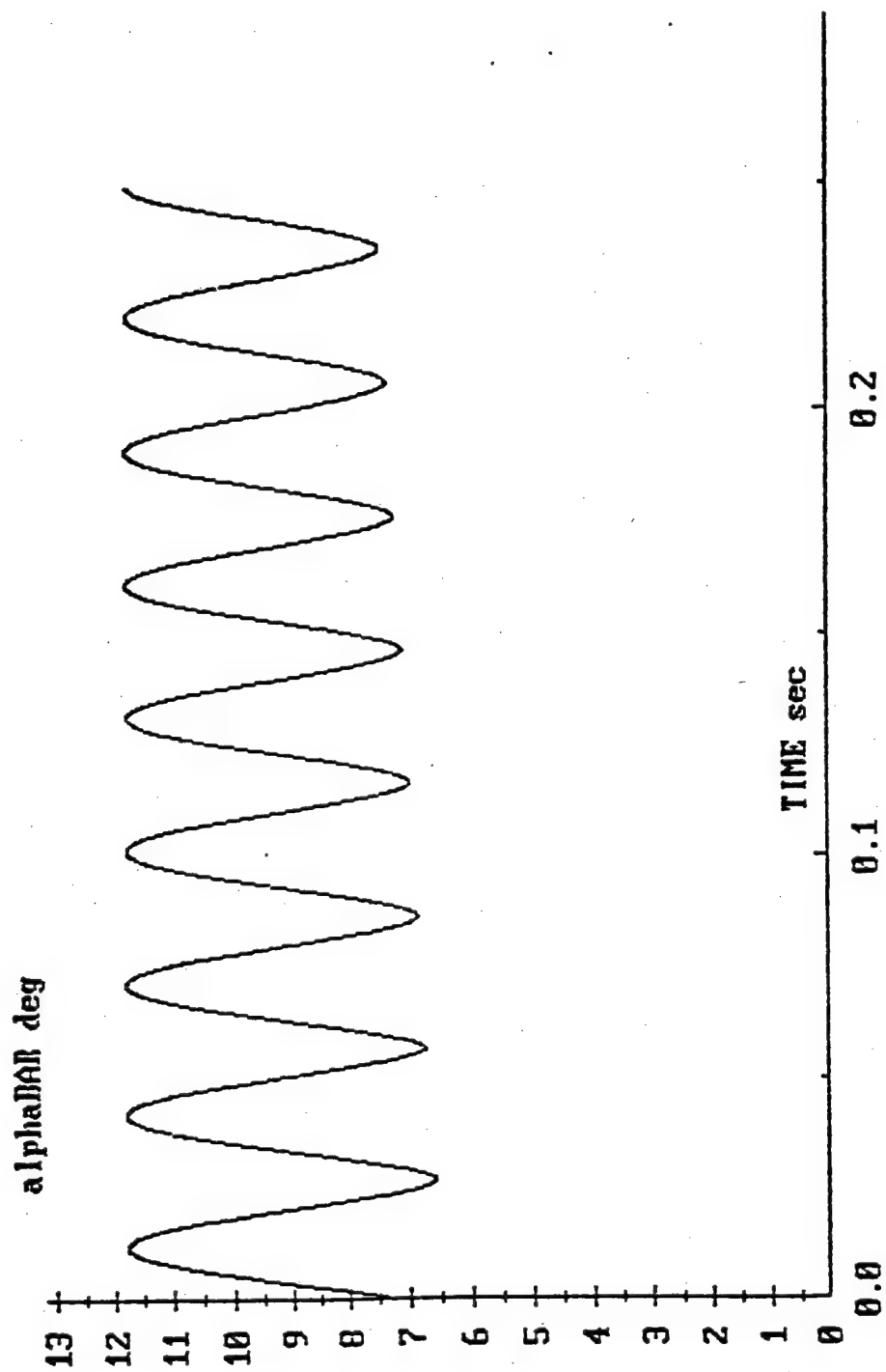


Figure 16 -- Total Yaw Angle History for Figure 13

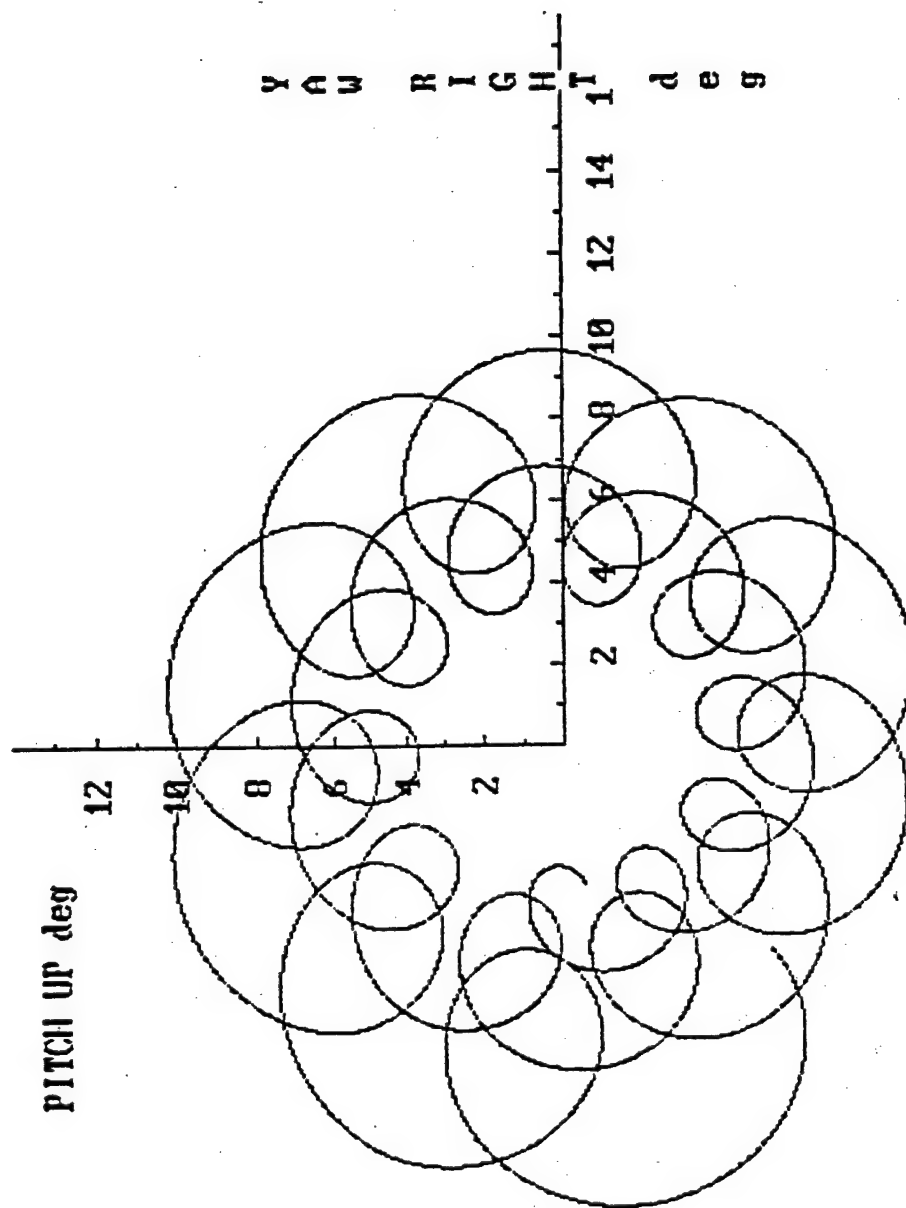


Figure 17 -- Damped Epicycle Motion of M107 at Mach 2 and +5 Degrees and +5 Radians/Sec Pitch and Yaw

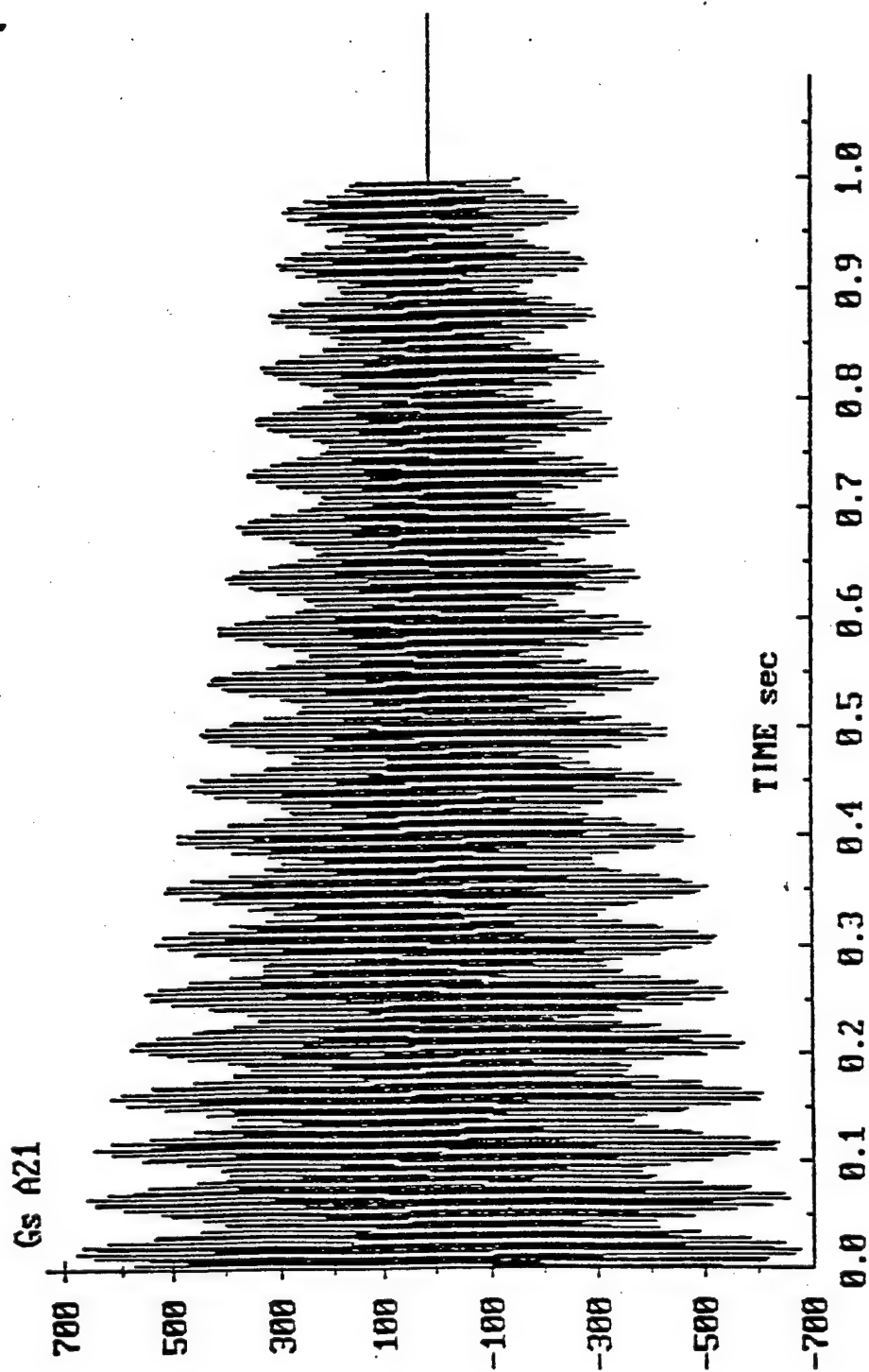


Figure 18 -- Acceleration Trace from One Radial Accelerometer for Figure 17

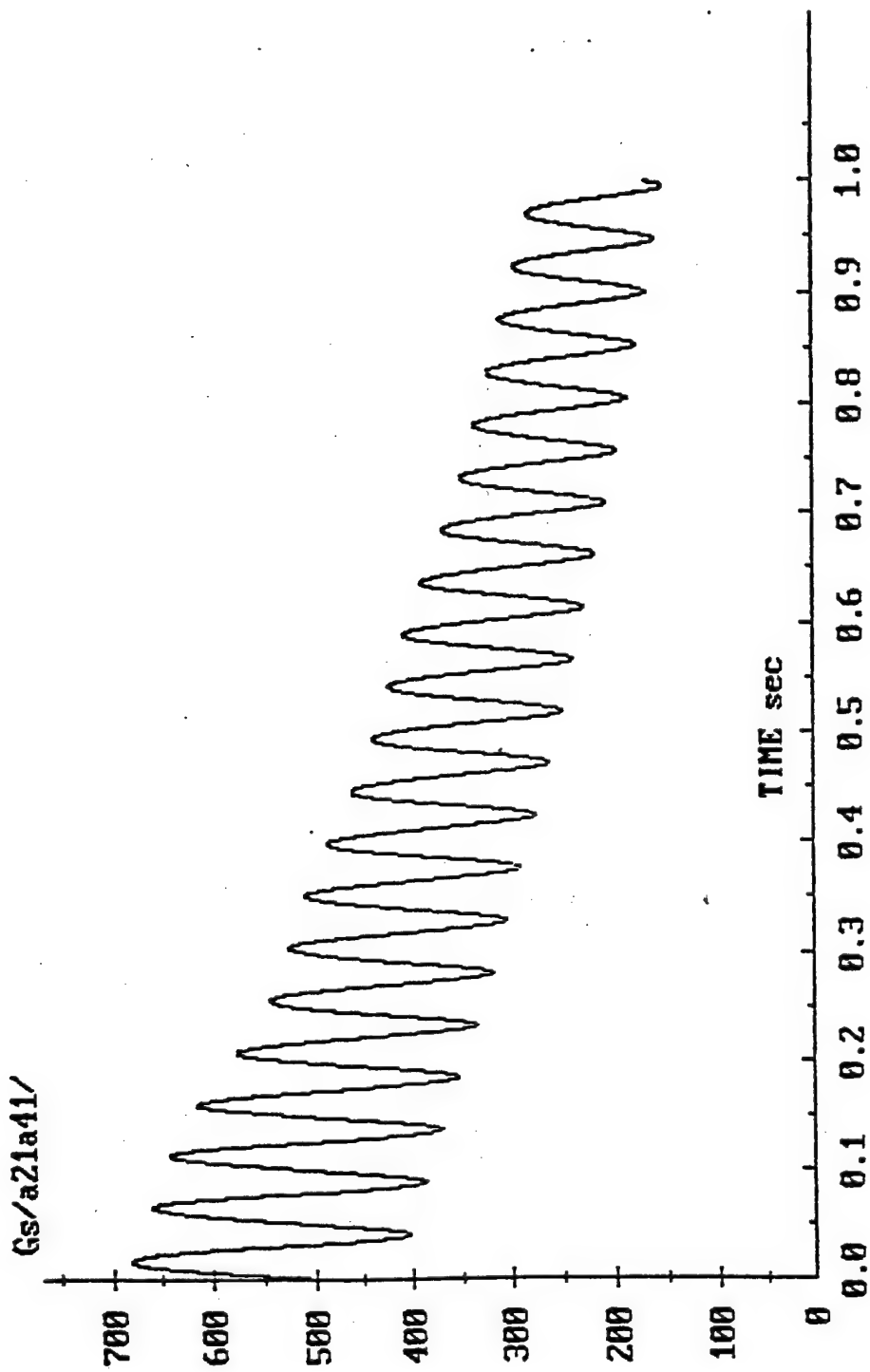


Figure 19 -- Vector Sum of Two Orthogonal Radial Accelerometers for Figure 17

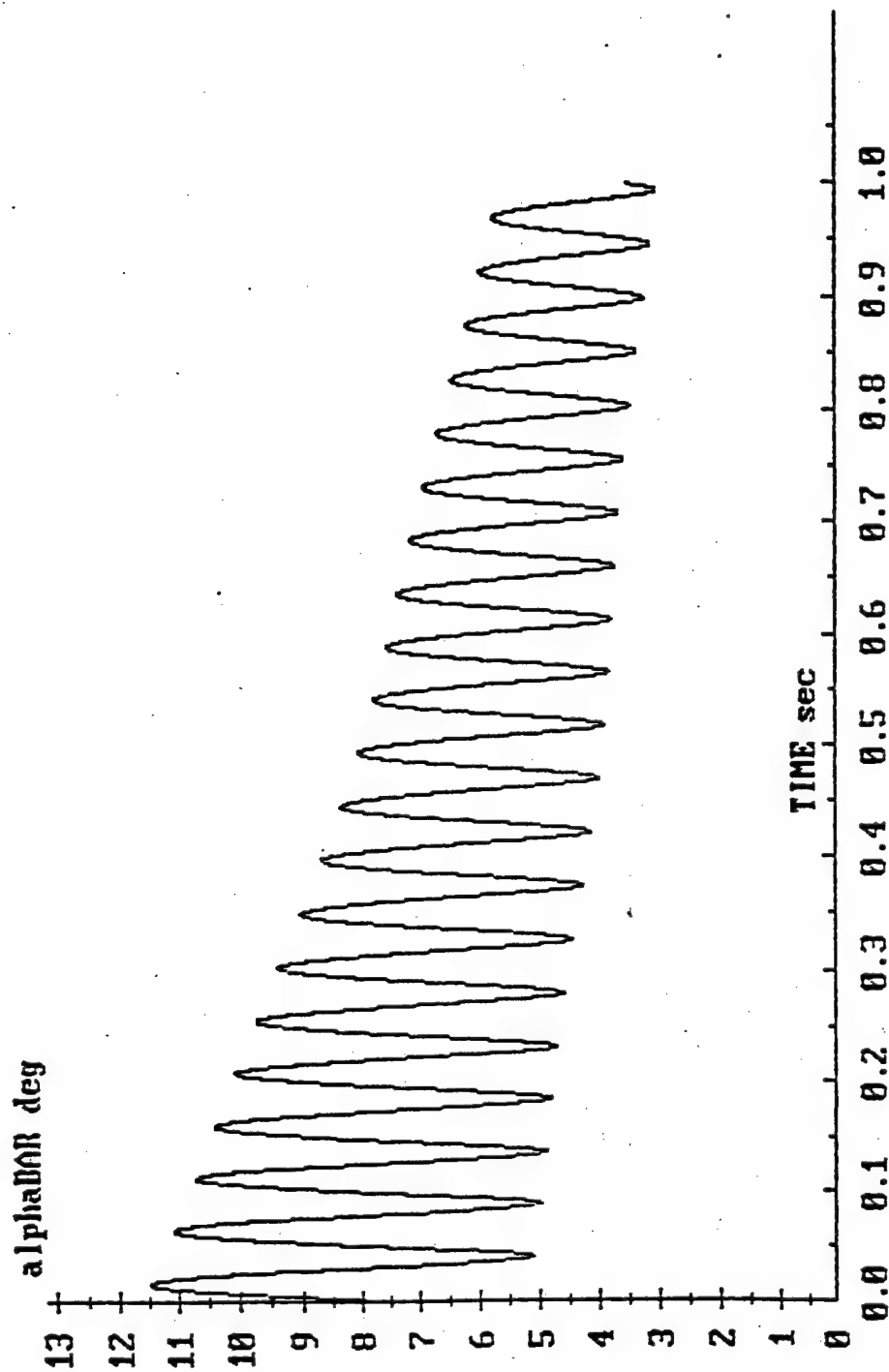


Figure 20 -- Total Angle of Attack (Yaw) History for Figure 17

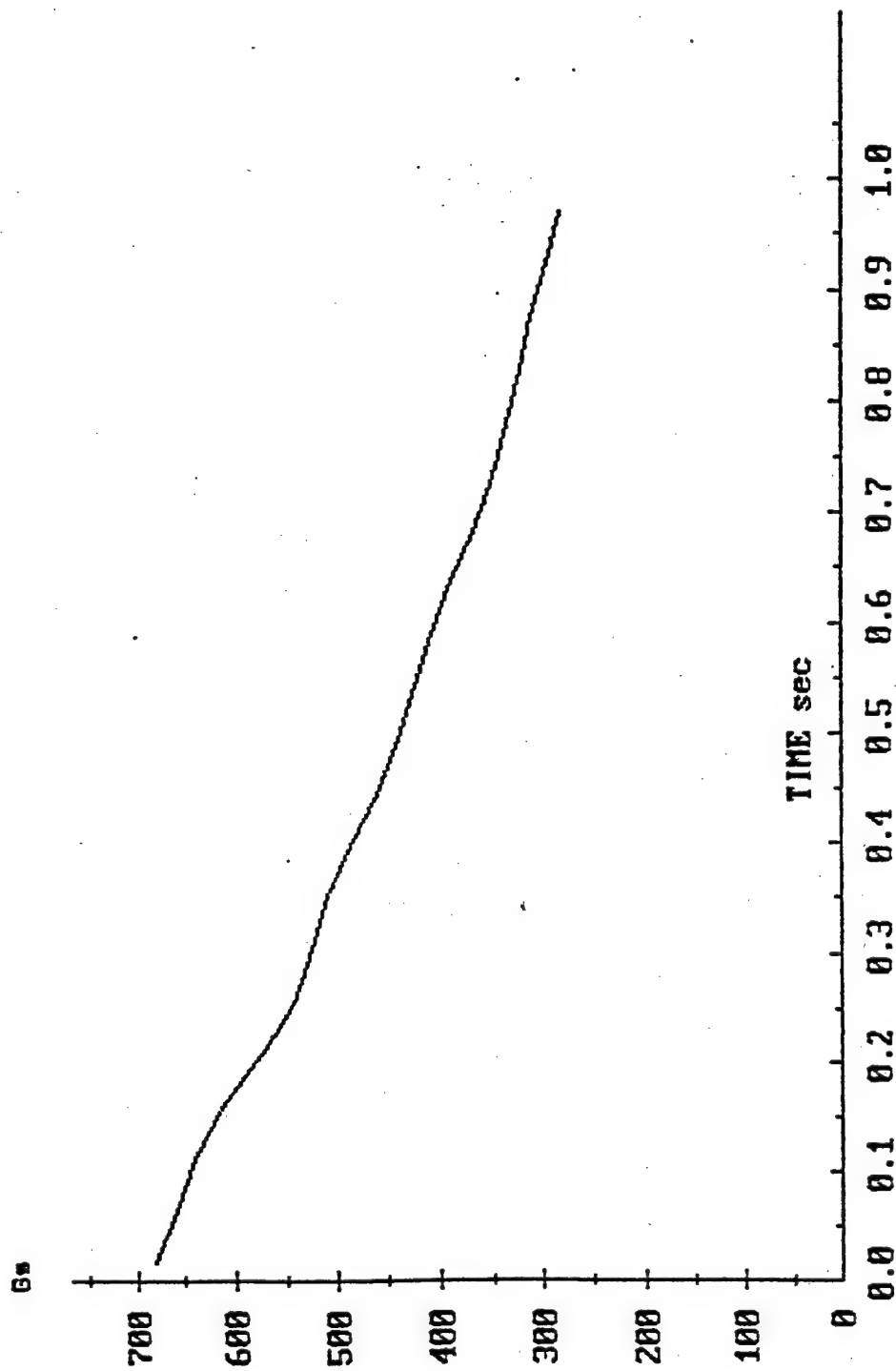


Figure 21 -- Peak Values from Damped Acceleration Trace, Figure 19

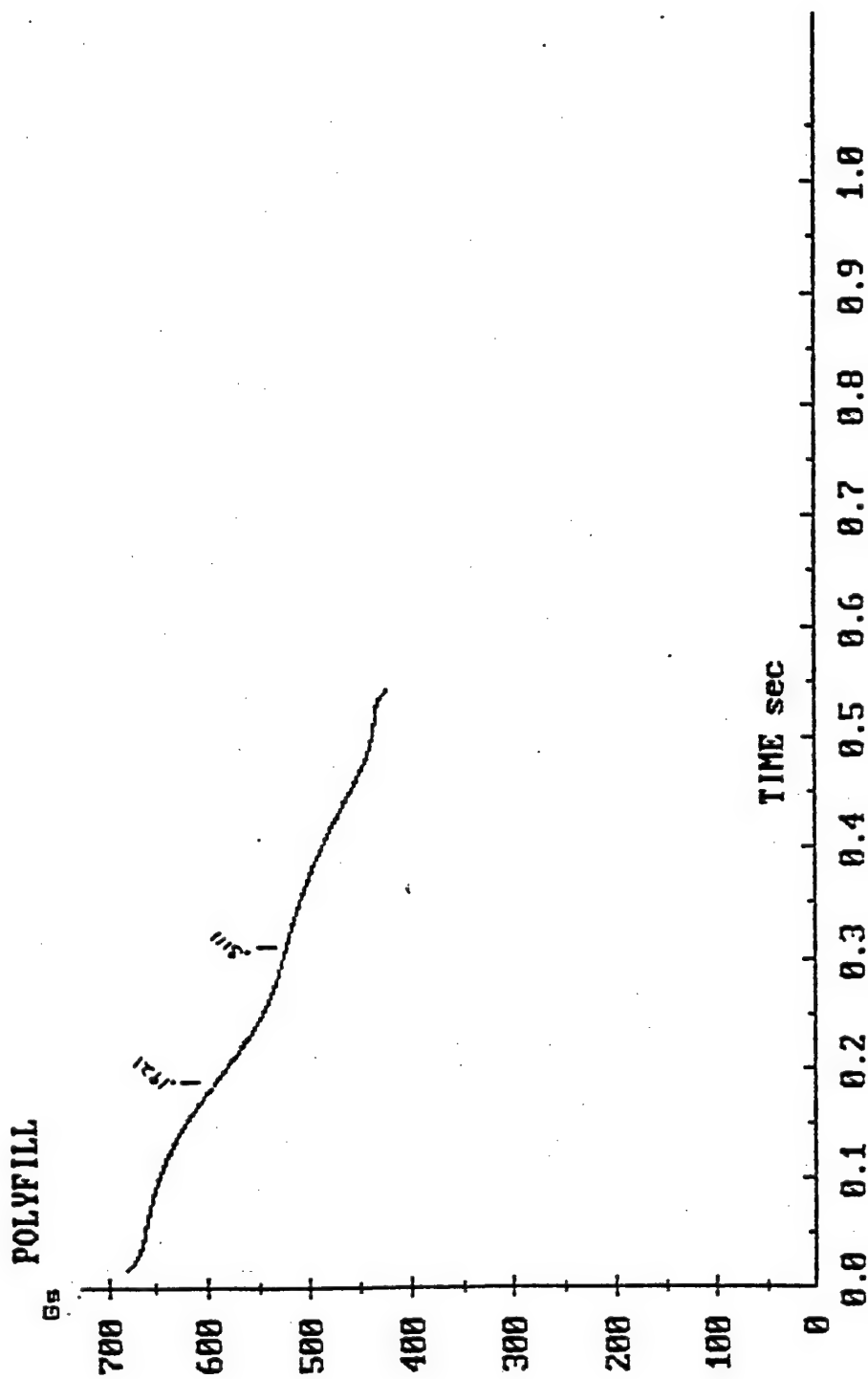


Figure 22 -- Polynomial Interpolation of Peak Values from the Front Portion of Figure 21

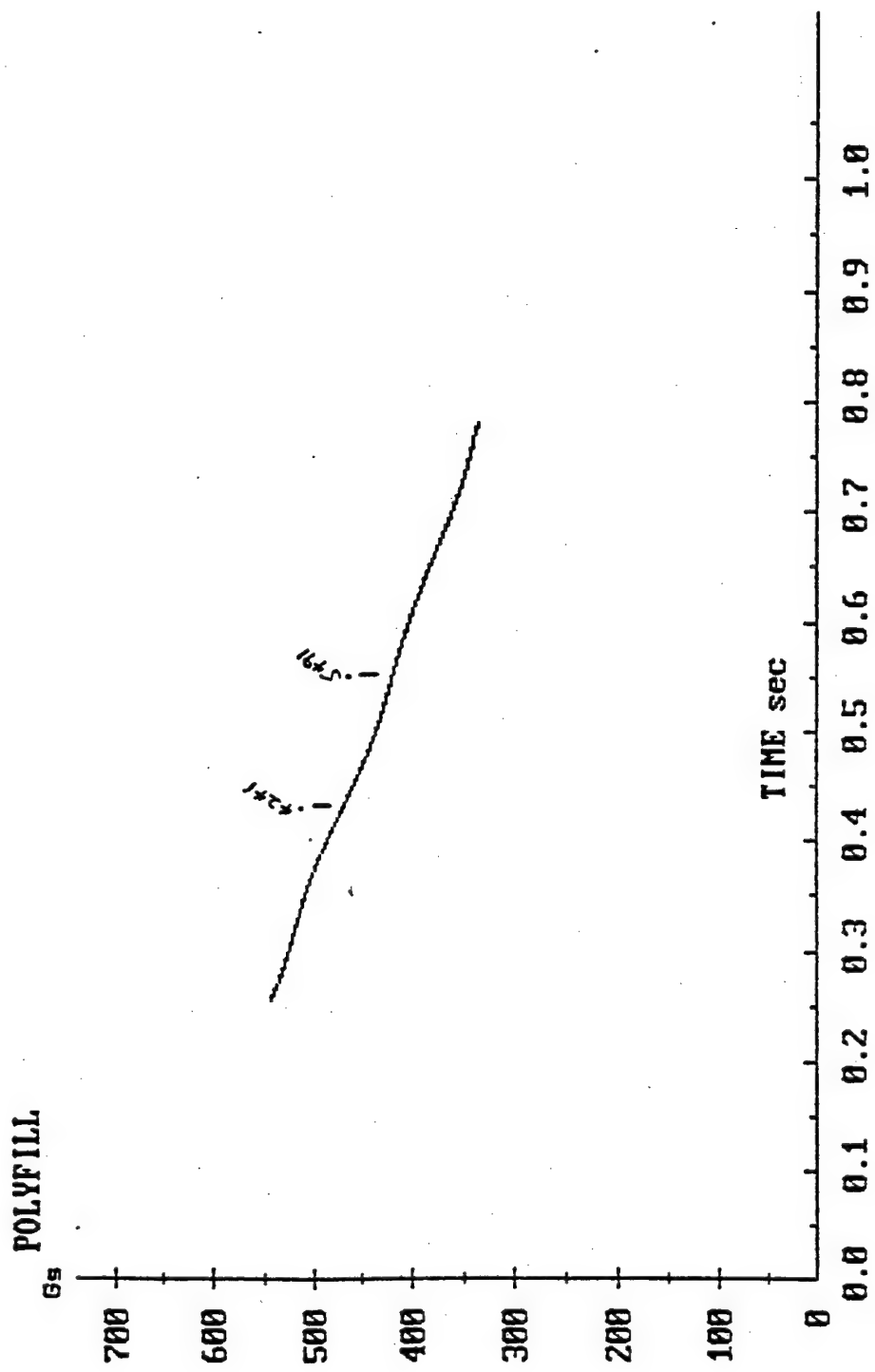


Figure 23 -- Polynomial Interpolation of Peak Values from the Central Portion of Figure 21

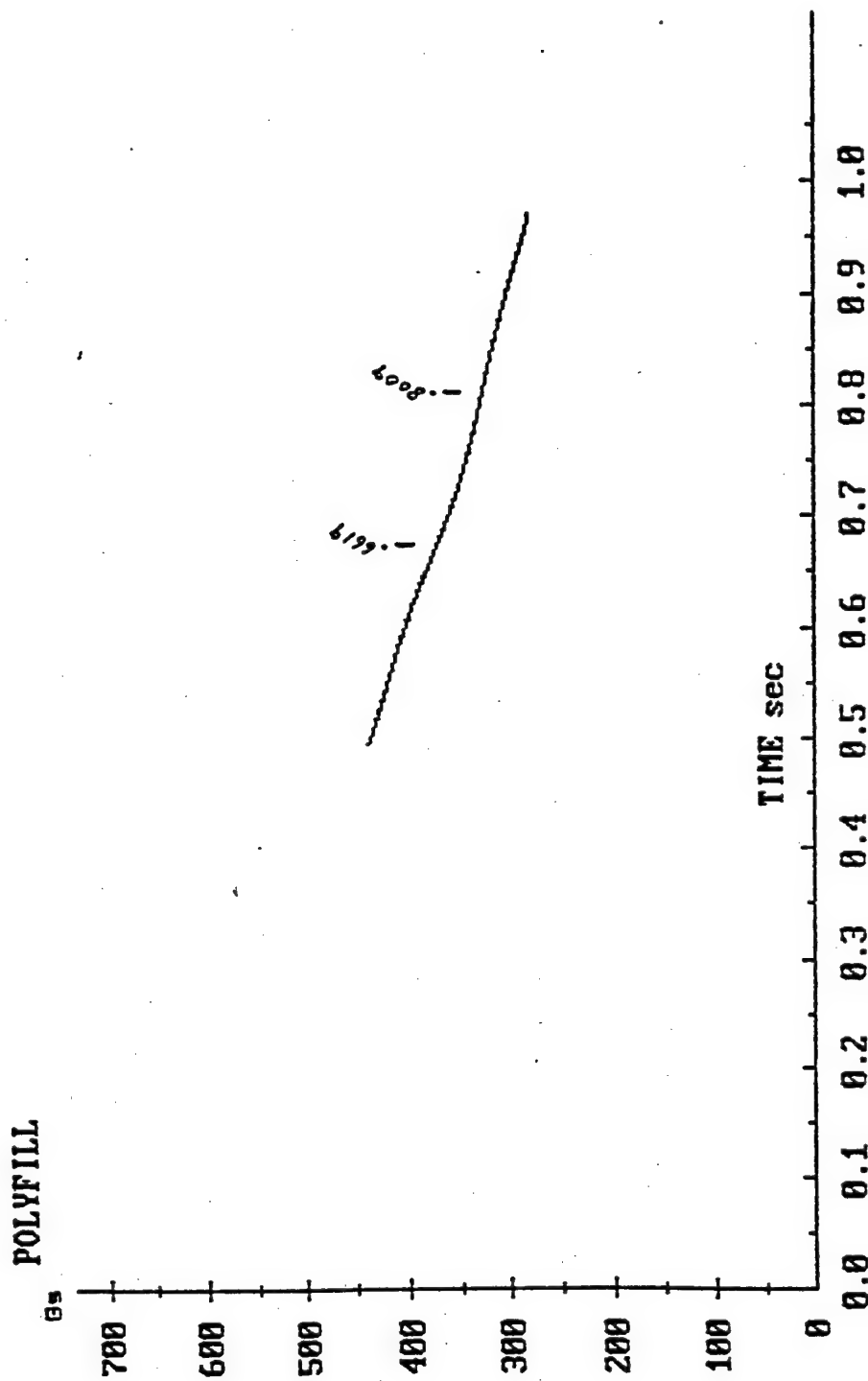


Figure 24 -- Polynomial Interpolation of Peak Values from the Tail Portion of Figure 21

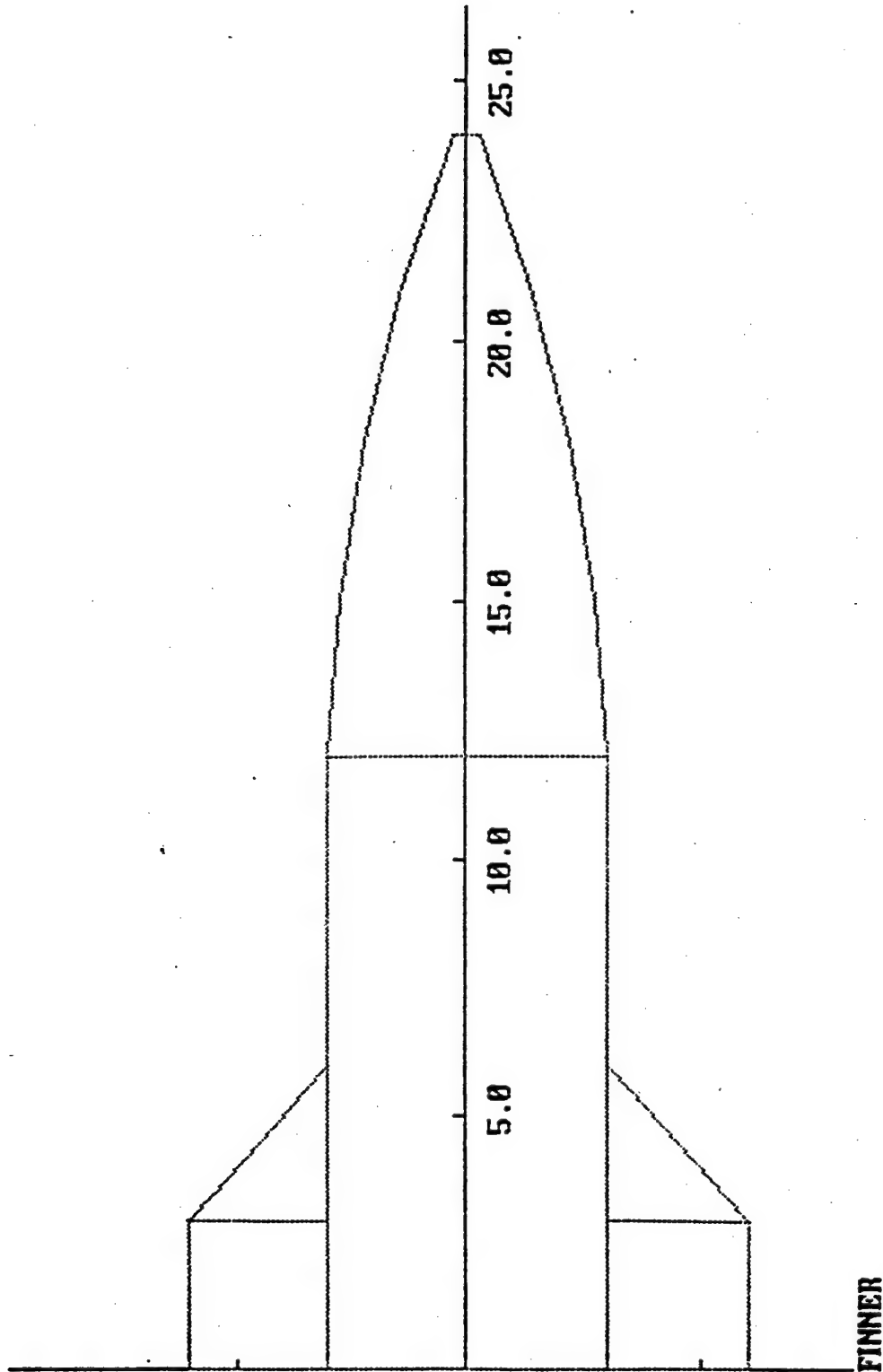


Figure 25 -- Generic Fin Stabilized Projectile Design

possible.

To overcome this lack of maxima and minima in the surface wave, the peak data points were interpolated for inflection points. Figures 22, 23, and 24 show the interpolated curves generated over three incremental and overlapping time intervals. Only the inflection points identified in the central region of each curve are considered valid, since the end conditions introduce greater interpolation errors at the tails of each curve. Rates were determined for intervals between succeeding downward inflections and upward inflections. Two pairs were identified and the average rate for all four cycles was 26.21 radians/sec. Half of this is 13.1, which is slightly under the expected precession rate of 13.8. It is possible that aerodynamic drag has reduced the effect of the pitching moment on the precession rate, and this may explain the lower identified rate. Other errors may involve the interpolation interval and time increment. A .0001 second interpolation interval was applied to the data points.

c. For Undamped Epicycle Motion of Fin Stabilized Projectile

Figure 25 shows a fin stabilized projectile, designed to have a low static margin, and perhaps some dramatic yawing modes. Table 2 shows the mass properties of this projectile and its aerodynamic coefficients. Table 6 shows the relevant mass and aerodynamic properties, the applicable stability equations from reference 1, and the resulting rates of motion for a Mach 2 launch condition and 50 Hz spin rate.

Table 6
Calculation of Expected Nutation and Precession Rates

I_x	=	227.8 lb-in ²	
I_y	=	1833 lb-in ²	
D_{ref}	=	6 inches	
C_{ma}	=	-1.05	pitching moment coefficient at Mach 2
P	=	50 Hz spin rate (314 rads/sec)	
ρ	=	.002378 slugs/ft ³	air density
V	=	2234 ft/sec	

W_1	=	$[P \cdot I_x / (2 \cdot I_y)] \cdot (1 + \sigma)$	nutation rate
W_2	=	$[P \cdot I_x / (2 \cdot I_y)] \cdot (1 - \sigma)$	precession rate

where,

$$\sigma = (1 - 1/Sg)^{1/2}$$

and,

$$Sg = 2 * I_x * P^2 / (\pi * I_y * \rho * C_{ma} * D_{ref}^3 * V^2)$$

yields:

Expected nutation rate	=	63.42	radians/sec
Expected precession rate	=	-24.38	radians/sec

As can be deduced from the negative precession rate, the precession is retrograde to the nutation and spin rate of the projectile. This launch condition was simulated using the 6DOF computer program, and the resulting epicycle motion for a one second time of flight is shown in Figure 6. Damping was turned off for the simulation, so the only coefficient used was C_{ma} . The projectile was given an initial velocity of Mach 2 and +5 degrees and +5 radians/sec initial conditions in the pitch and yaw directions. In the motion of Figure 26, the nutation rate is clockwise, beginning at the origin with zero pitch and yaw amplitude. This nutation is superimposed upon the precession, which is counter-clockwise. Therefore, the projectile makes all loops beginning with number 1 in a clockwise path, yet all motion between loops is swept out counter-clockwise about the origin, as can be observed by following the successive loop numbers. We can see that nearly 14 loops are generated, or approximately 13.75 loops, and this rate calculates to about 86.4 radians per second. This rate is approximately the expected nutation minus the expected precession rate for the projectile (i.e. 87.8 rads/sec). What is interesting to notice at this point is that both the motions for the spin and fin stabilized projectiles contain the same characteristic frequency of nutation minus precession, despite the fact that one is prograde and the other is retrograde motion.

Figure 27 shows the total angle of attack history from the 6DOF simulation, and performing a moving average of the cyclic rate gives approximately 87 radians/sec. Figure 28 shows the vector sum of two orthogonal radially oriented accelerometers, and its rate is also about 87 radians/sec. All of these rates are just slightly below the expected nutation-precession rate of 87.8 radians/second.

Figure 29 shows the output trace from one radially oriented accelerometer. A moving average of its peak-to-peak and min-to-min intervals shows a frequency of about 237 radians/sec. Averaging zero crossings gives a rate of 238 radians/second. As with the spin stabilized case, one would expect this rate to be the spin minus the nutation rate, or in this case about 251 radians/sec. This, however, is not the case, or at least if it is, there is a very large error.

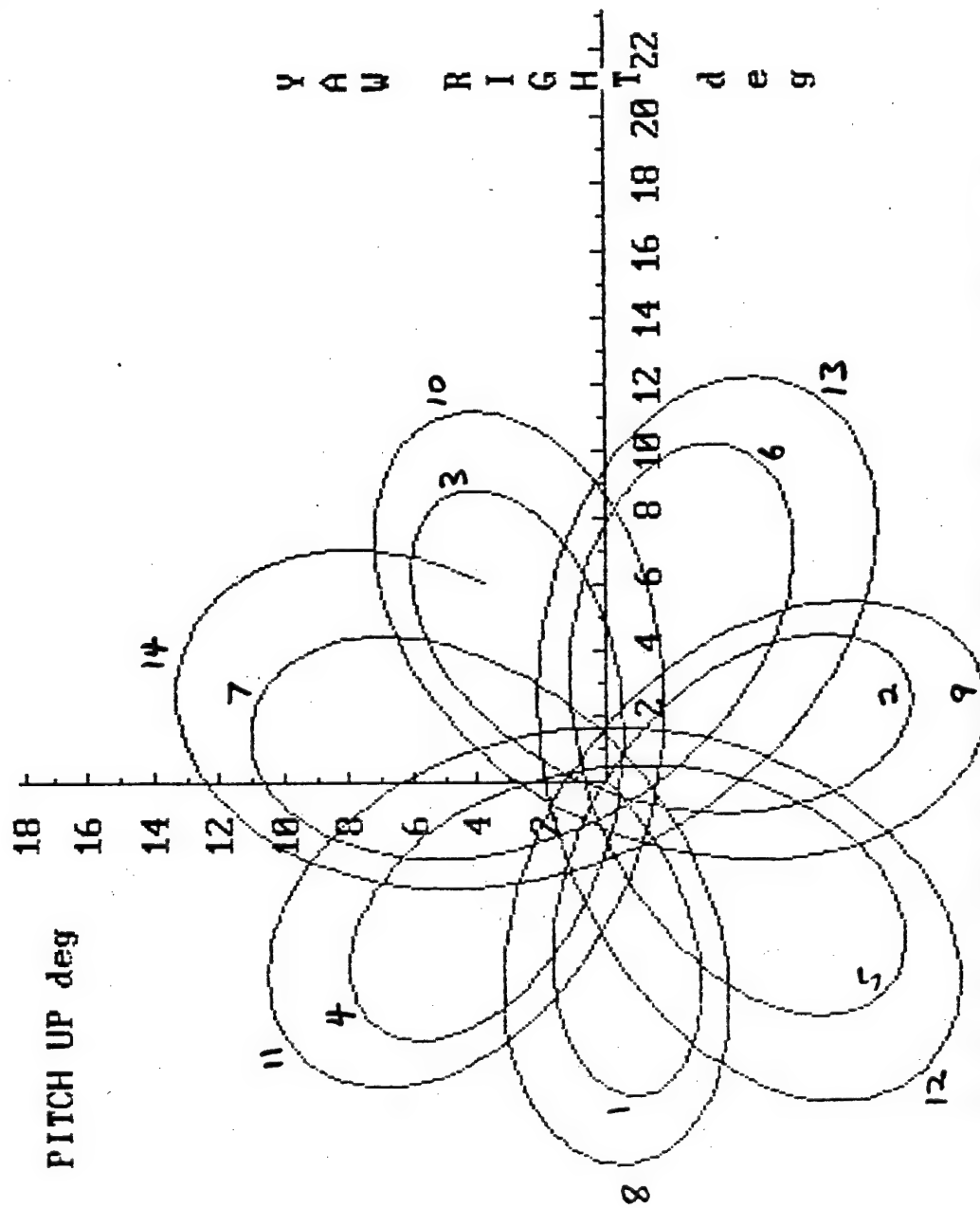


Figure 26 -- Epicycle Motion of Finner with 50 Hz Spin Rate

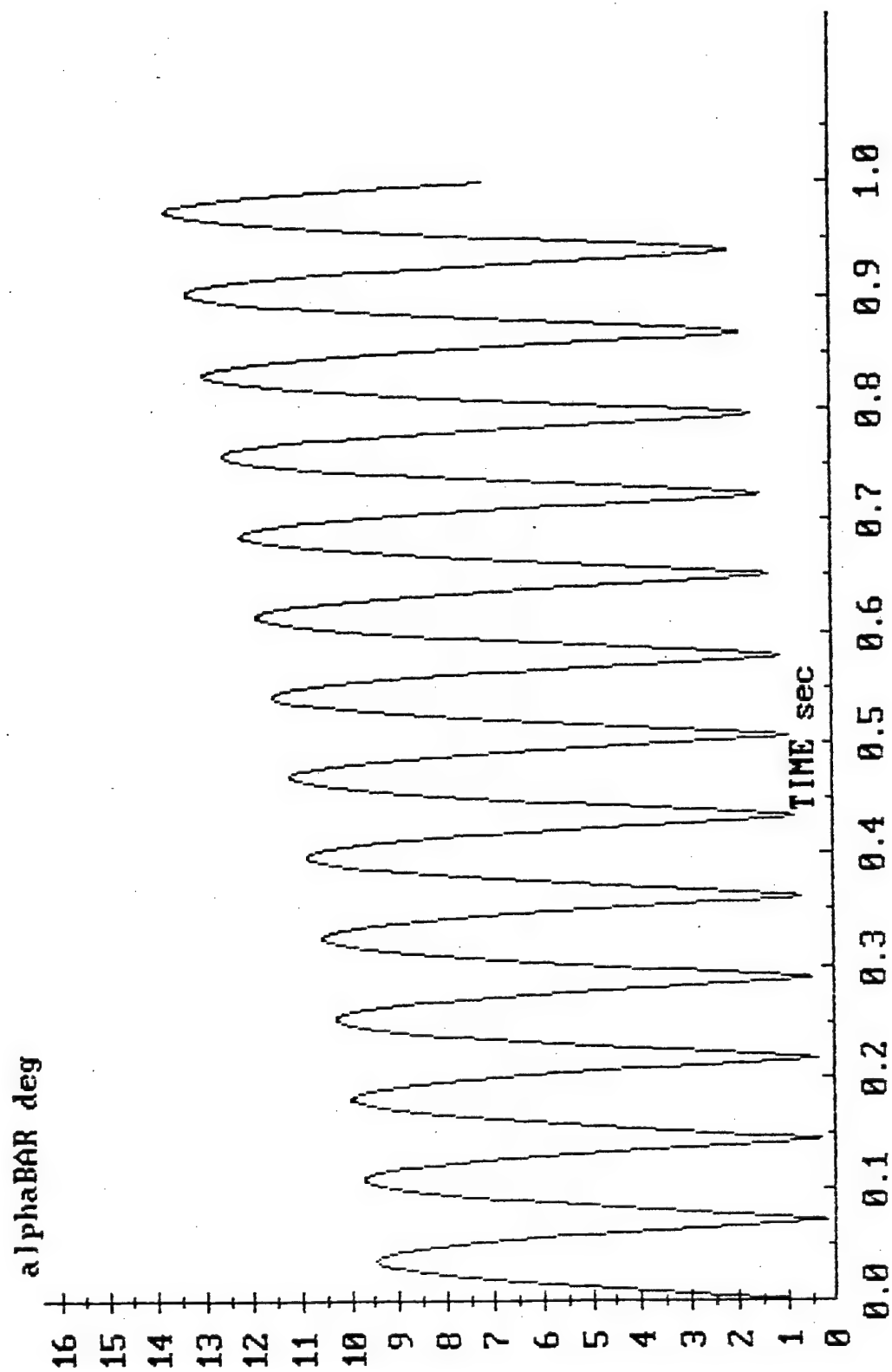


Figure 27 -- Angle of Attack History for Figure 26 Epicycle Motion

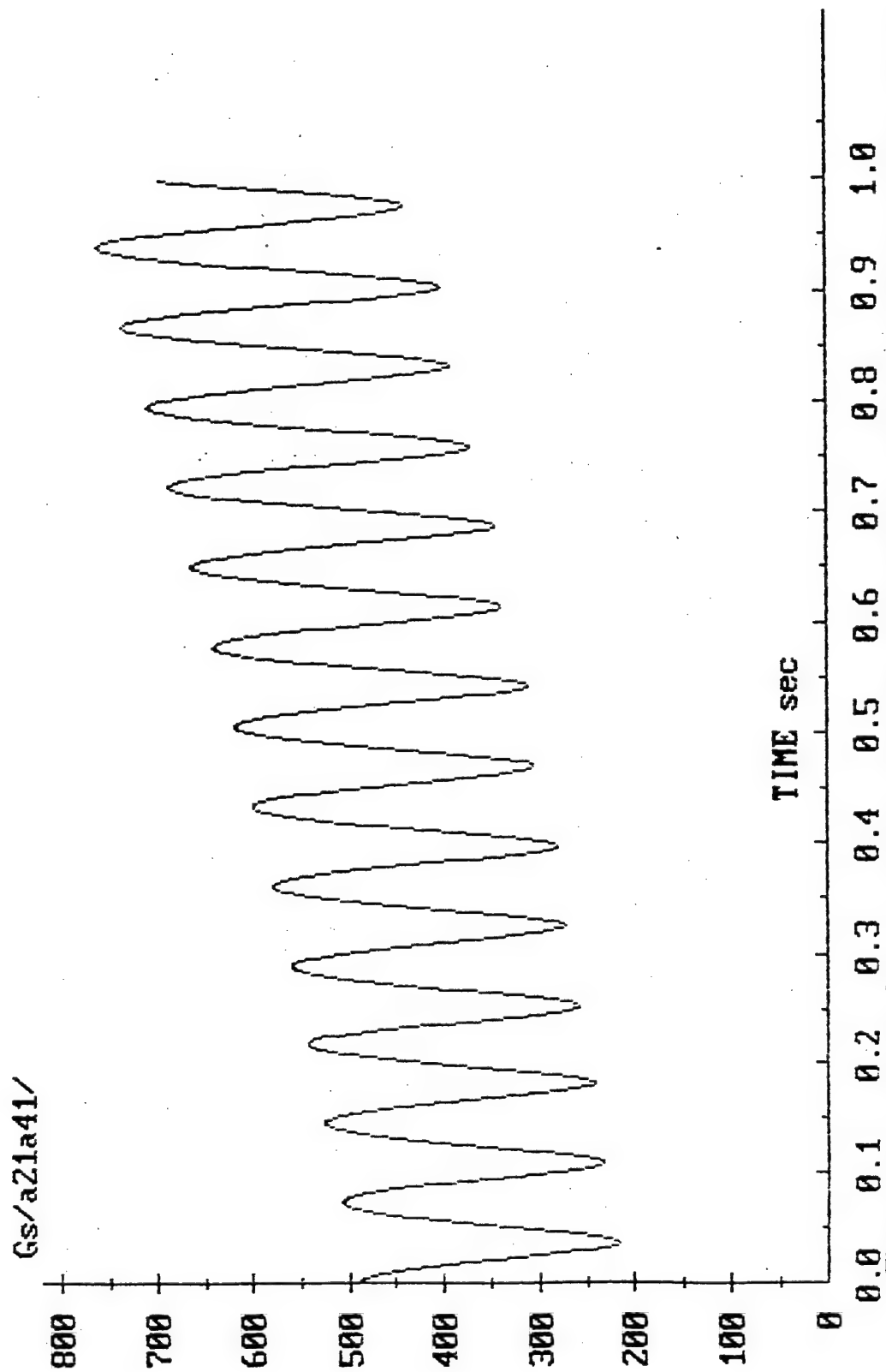


Figure 28 -- Vector Sum of Output from Two Orthogonal Radial Accelerometers for Figure 26

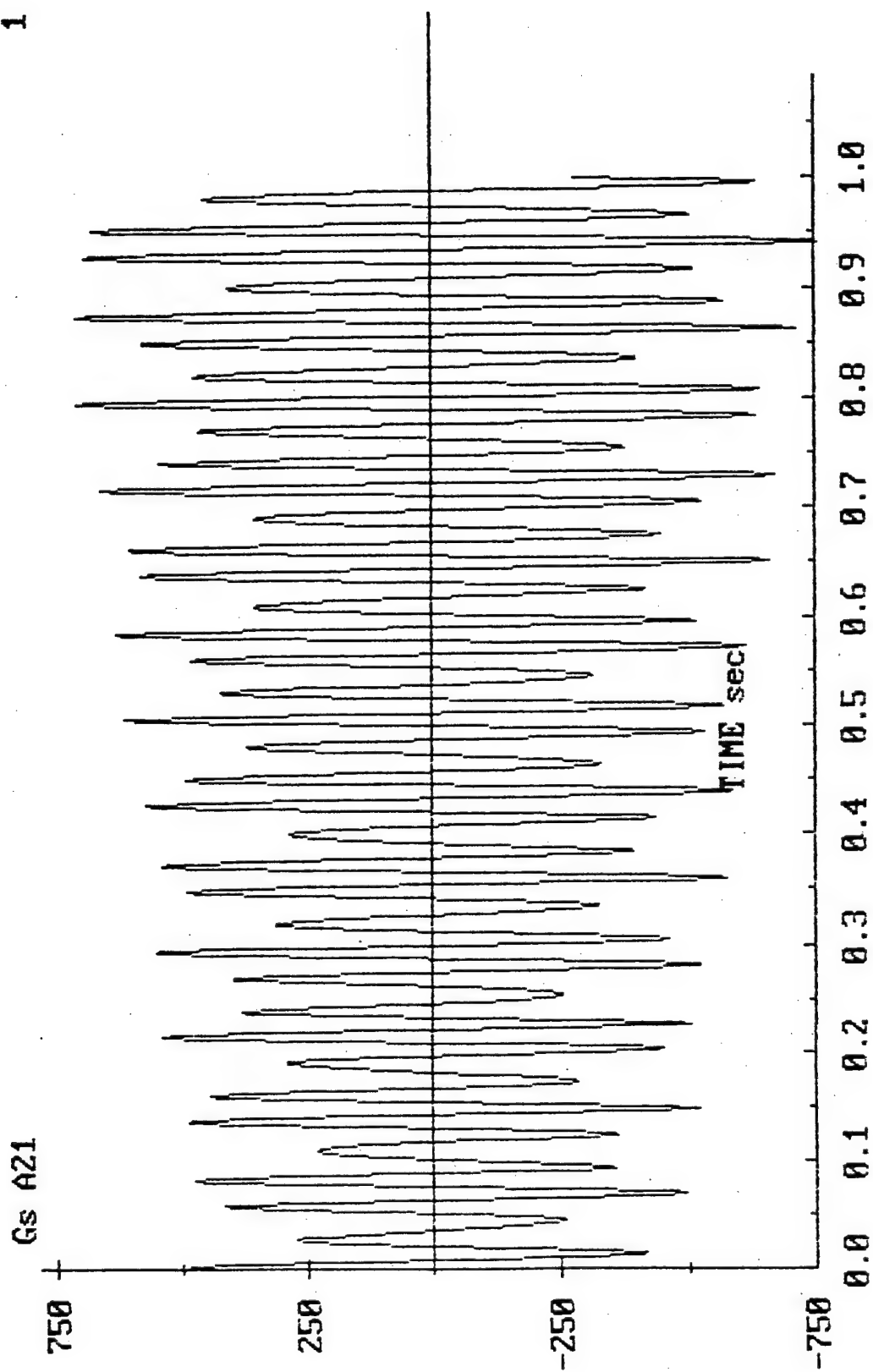


Figure 29 -- Output from One Radial Accelerometer for Figure 26

Looking closer at Figure 29, one can see two additional frequencies in the trace. The most apparent is the one generating the large valleys between local maxima in the data. In Figure 30, these maximum values are isolated and connected by straight lines. Averaging the time intervals between maxs and mins yields a rate of about 87 radians/sec. This is nearly the expected nutation-precession rate and is surprisingly accurate for such choppy data. In Figure 30, there is still a surface wave apparent, riding on the peak values. In Figure 31, the peak values from Figure 30 are isolated and connected by straight lines, and this second frequency is clearly visible. Calculating the time intervals between the maxima and minima in the data in Figure 31 gives a consistent 21.6 radians/sec. This number is intriguingly close to the expected precession rate of 24.38 radians/sec.

Since Figure 31 consists of the choppy peak value data from the accelerometer trace in Figure 29, we did a polynomial interpolation about these points to see if the characteristic frequency was indeed the precession rate. Figures 32 through 36 show the resulting discrete interpolation curves for the data, and Table 7 presents the resulting maxima and minima points.

Table 7
Maxima and Minima in the Interpolated Data

Maximum Point Time	Minimum Point Time
.276	.338
.572	.626
.838	

The average of the two maximum point intervals and the one minimum point interval gives a rate of 22.2 radians/sec. This a little better than the results from the course data, but not close enough for confidence that this technique identifies the precession rate. Realizing that the technique which ultimately proved successful for the damped spin stabilized case involved averaging the rates between inflection points in the data, and since the curve in Figure 31 has a gradient which may affect the location of maxima and minima as with damped motion, we identified inflection points in the interpolated curves and measure rates between these. The inflection points are presented in Table 8.

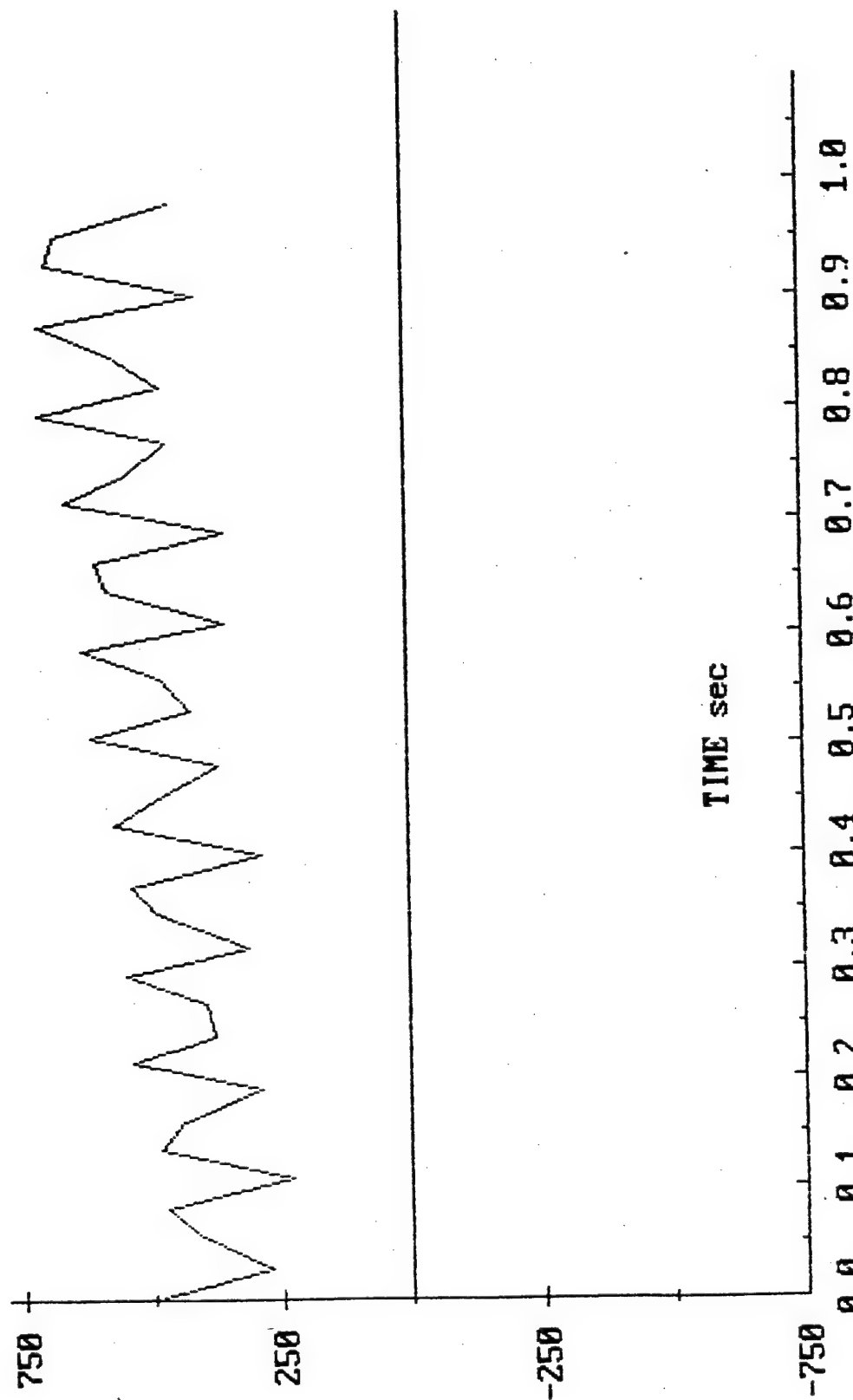


Figure 30 -- Peak Values from Figure 29

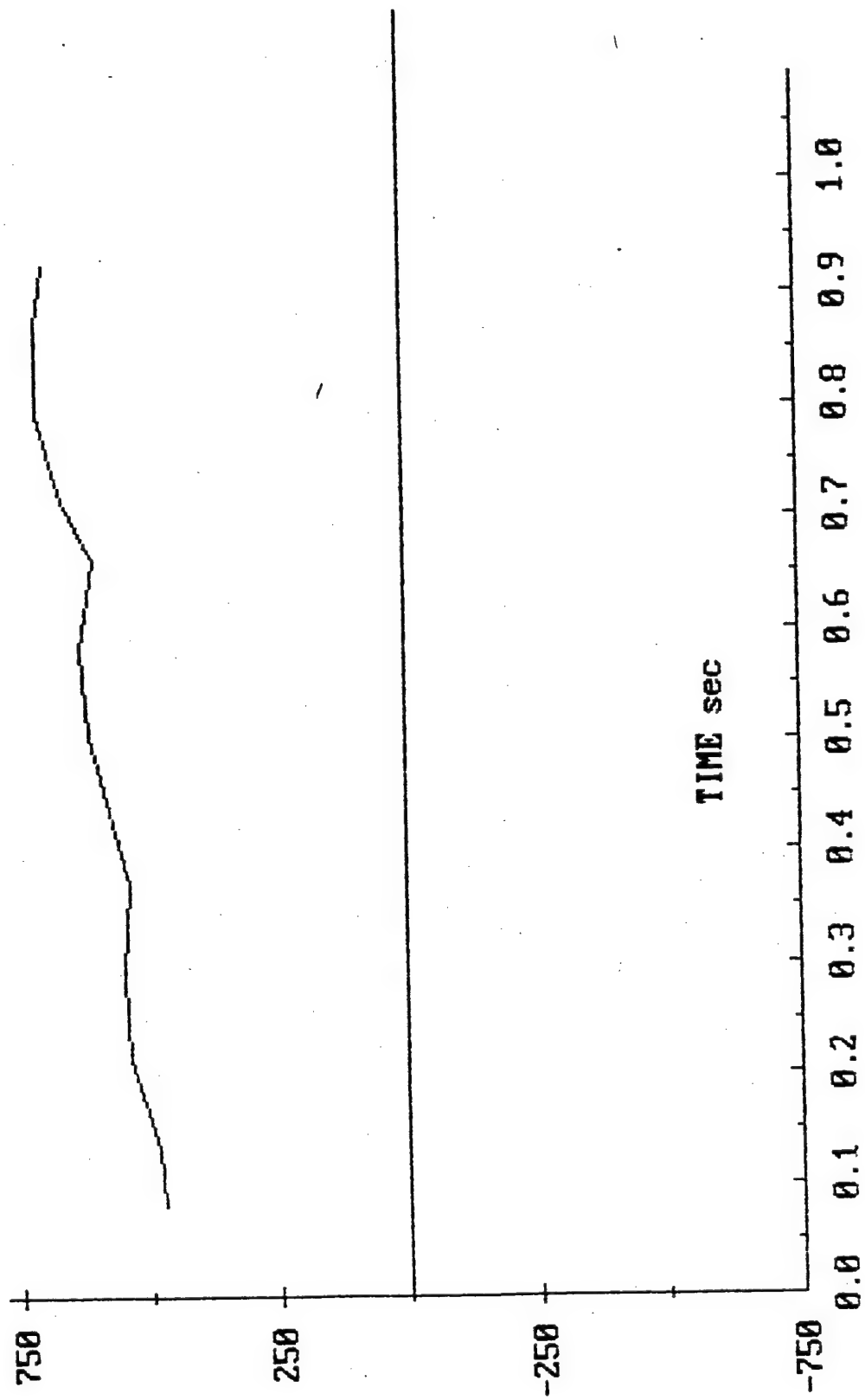


Figure 31 -- Peak Values from Figure 30

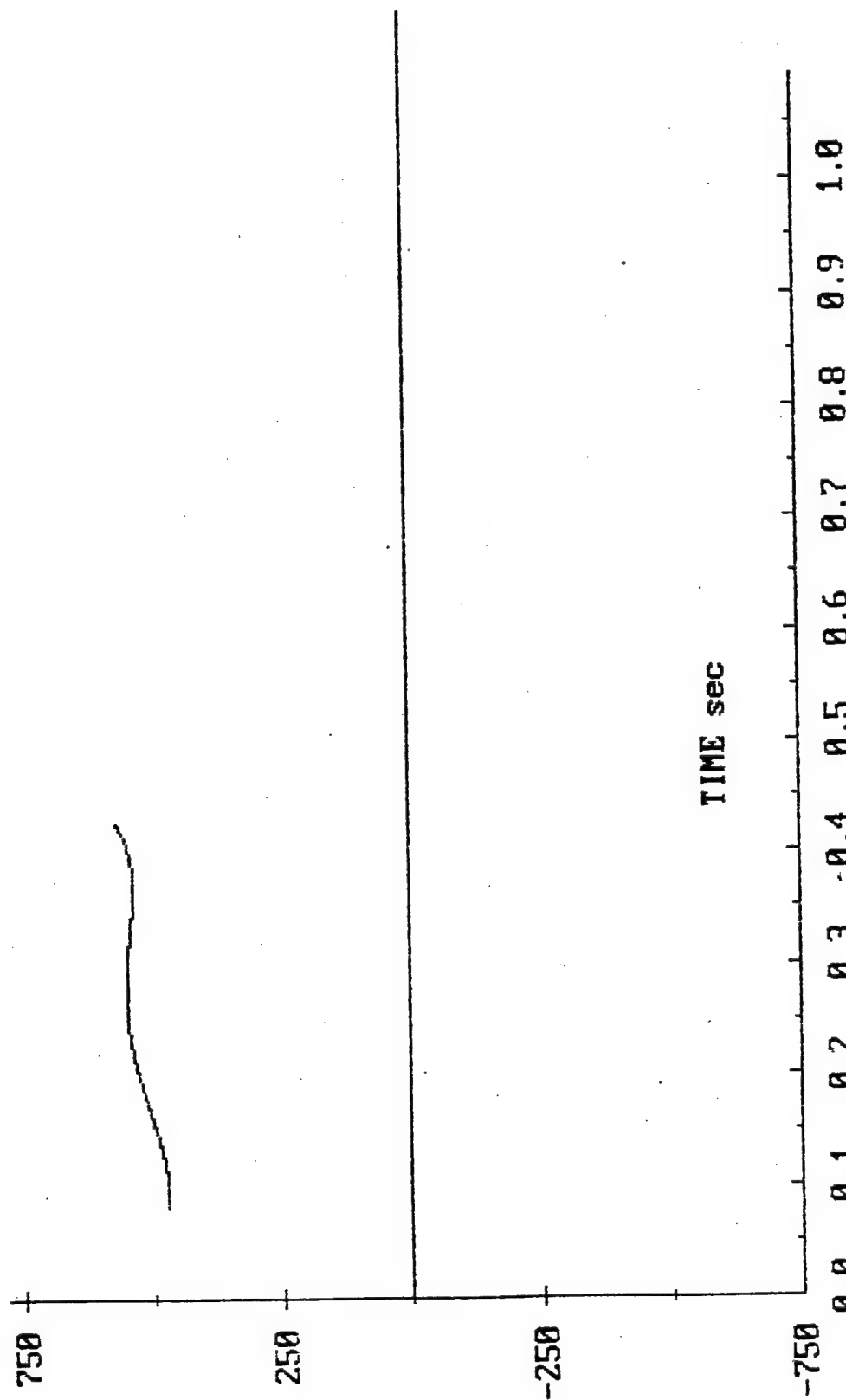


Figure 32 -- Polynomial Interpolation of Figure 31 Data

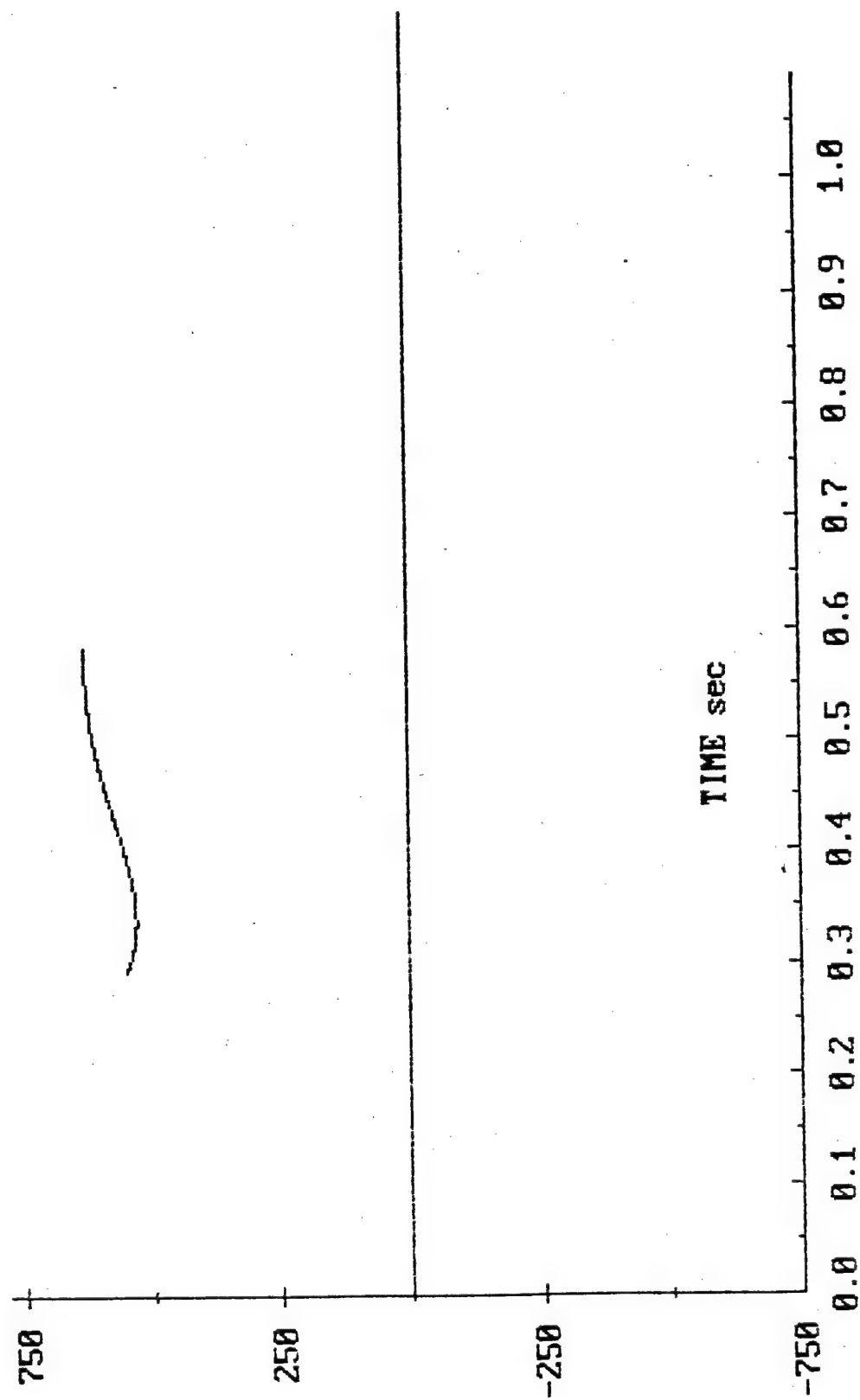


Figure 33 -- Polynomial Interpolation of Figure 31 Data, cont.

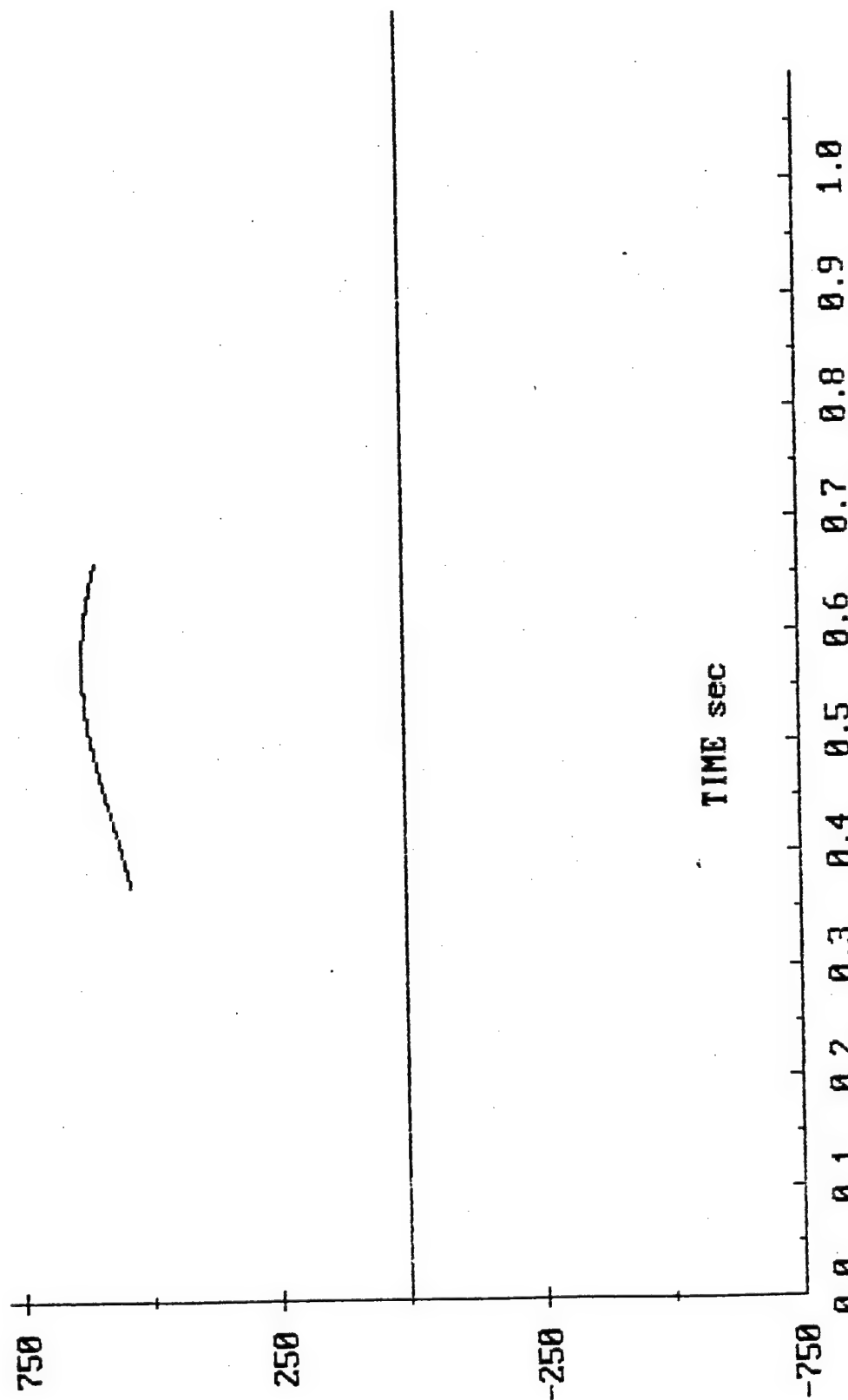


Figure 34 -- Polynomial Interpolation of Figure 31 Data, cont.

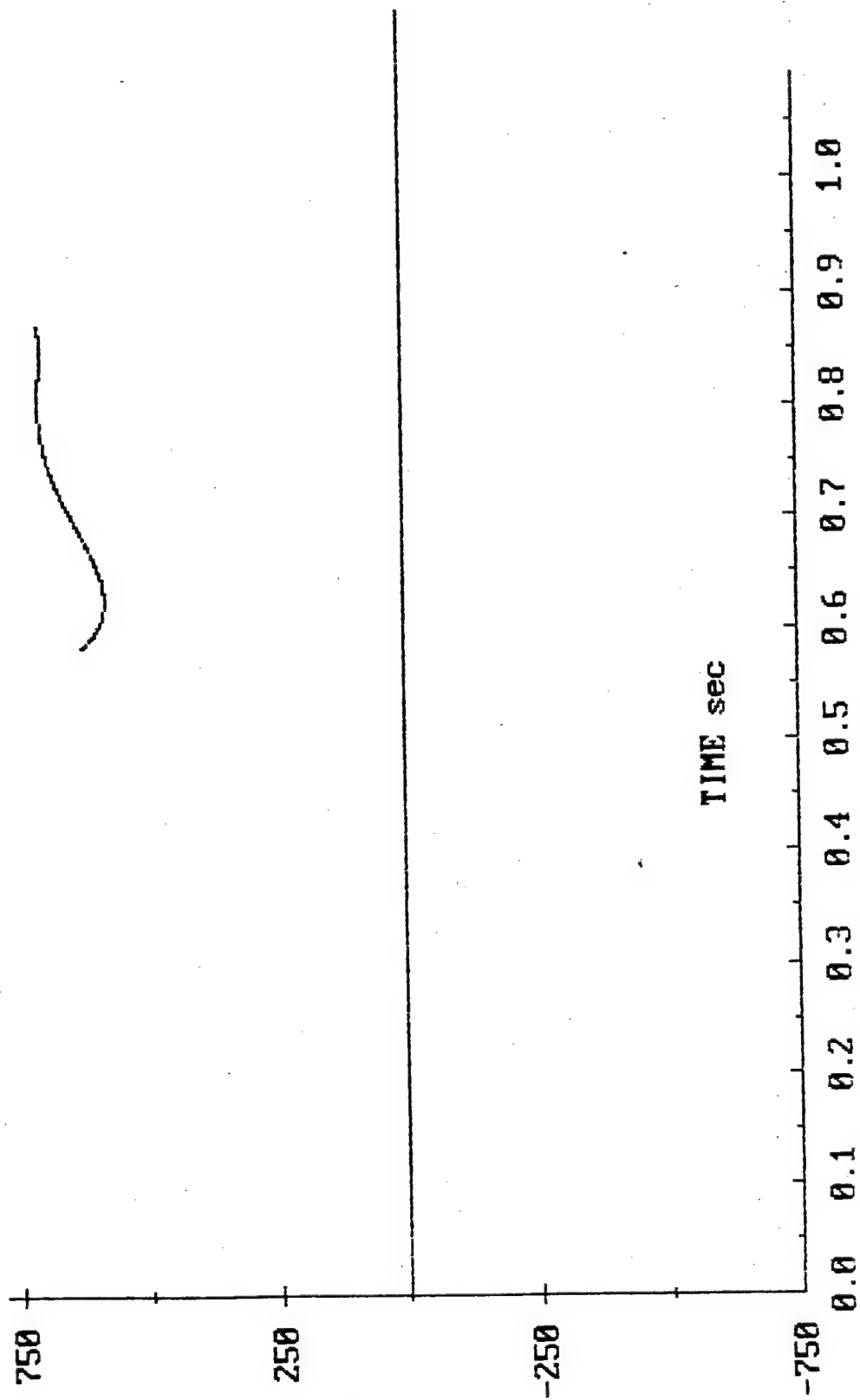


Figure 35 -- Polynomial Interpolation of Figure 31 Data, cont.

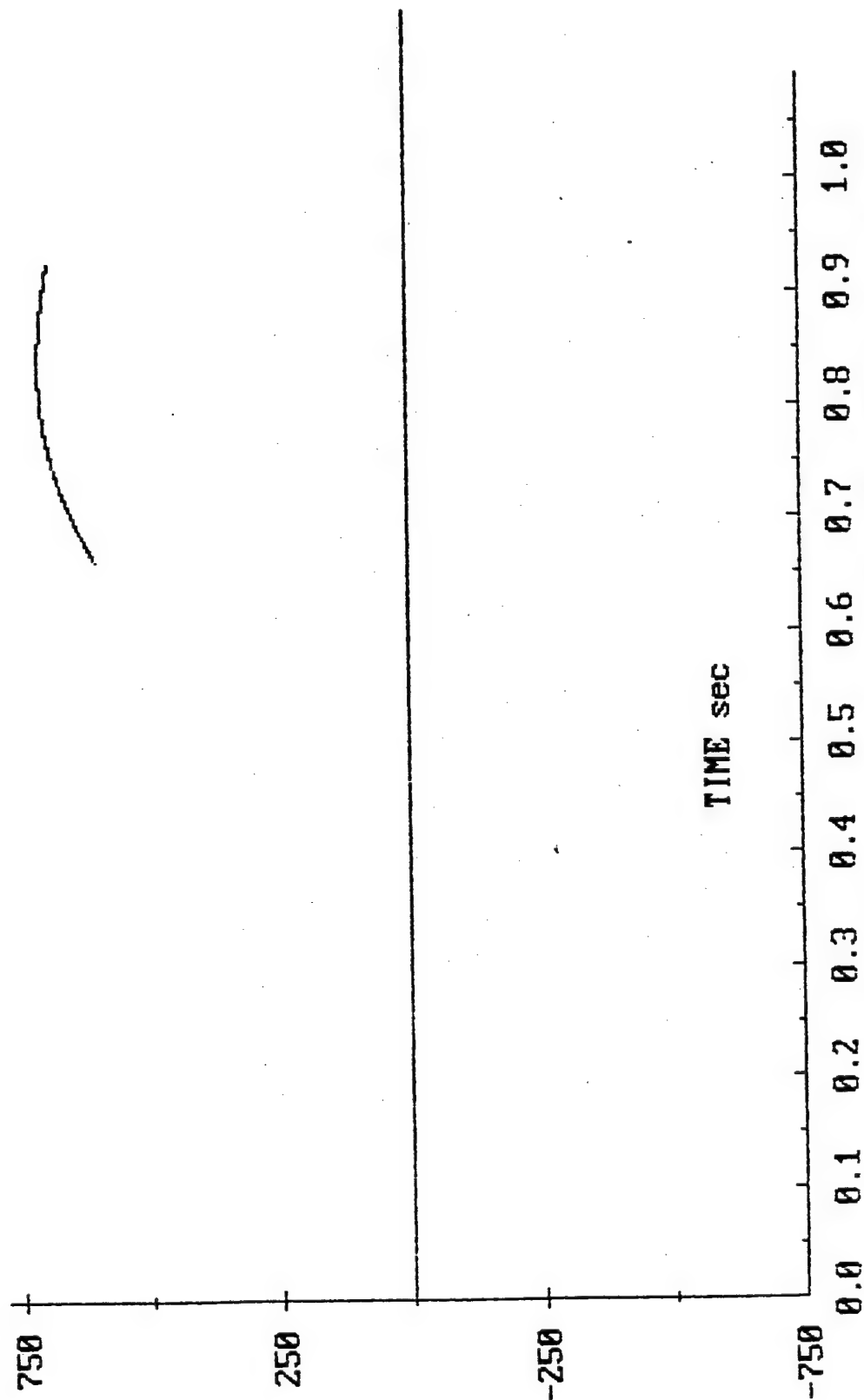


Figure 36 -- Polynomial Interpolation of Figure 31 Data, concluded

Table 8
Inflection Points in the Interpolated Data

Up Inflection Point Time	Down Inflection Point Time
.167	.329
.430	.578
.685	

The average rate for the two up inflection point intervals and the one down inflection point interval is 24.6 radians/sec and is just about the expected precession rate of 24.4 radians/sec.

To further test this finding, we changed the spin rate of the projectile to 75 Hz (471.2 rads/sec), which would result in different expected nutation and precession rates, and tried again. Under this spin condition the expected nutation rate is 78.3 rads/sec and the expected precession rate is -19.7 rads/sec. The initial conditions were also changed to give an initial angle of attack of +2.5 degrees pitch and +2.5 degrees yaw. Since the precession rate is lower than in the previous run, the elapsed time of flight was increased to 1.6 seconds, to give a reasonable number of precession cycles. Figure 37 shows the resulting epicycle motion. The nutation cycle is again clockwise, and the precession counter-clockwise.

Figure 38 shows the output trace from one radially oriented accelerometer. Its average rate is about 392.5 rads/sec using peak-to-peak and min-to-min intervals, and about 395.7 rads/sec using zero crossings. The expected spin minus nutation rate is 392.9 rads/sec. As one would expect, this rate falls out of the accelerometer data very accurately. Success in this case, however, does not explain the large error in the previous case.

Following the procedure used in the previous case, the maximum values from Figure 38 are isolated and plotted in Figure 39. The average rate for this course data is about 98.3, and is nearly the expected nutation minus precession rate of 98 rads/sec. In Figure 40, the maximum data from Figure 39 are again isolated and plotted. The waviness of this curve is not as apparent, but inflection points, nevertheless, do exist even in the course data, and they are presented in Table 9.

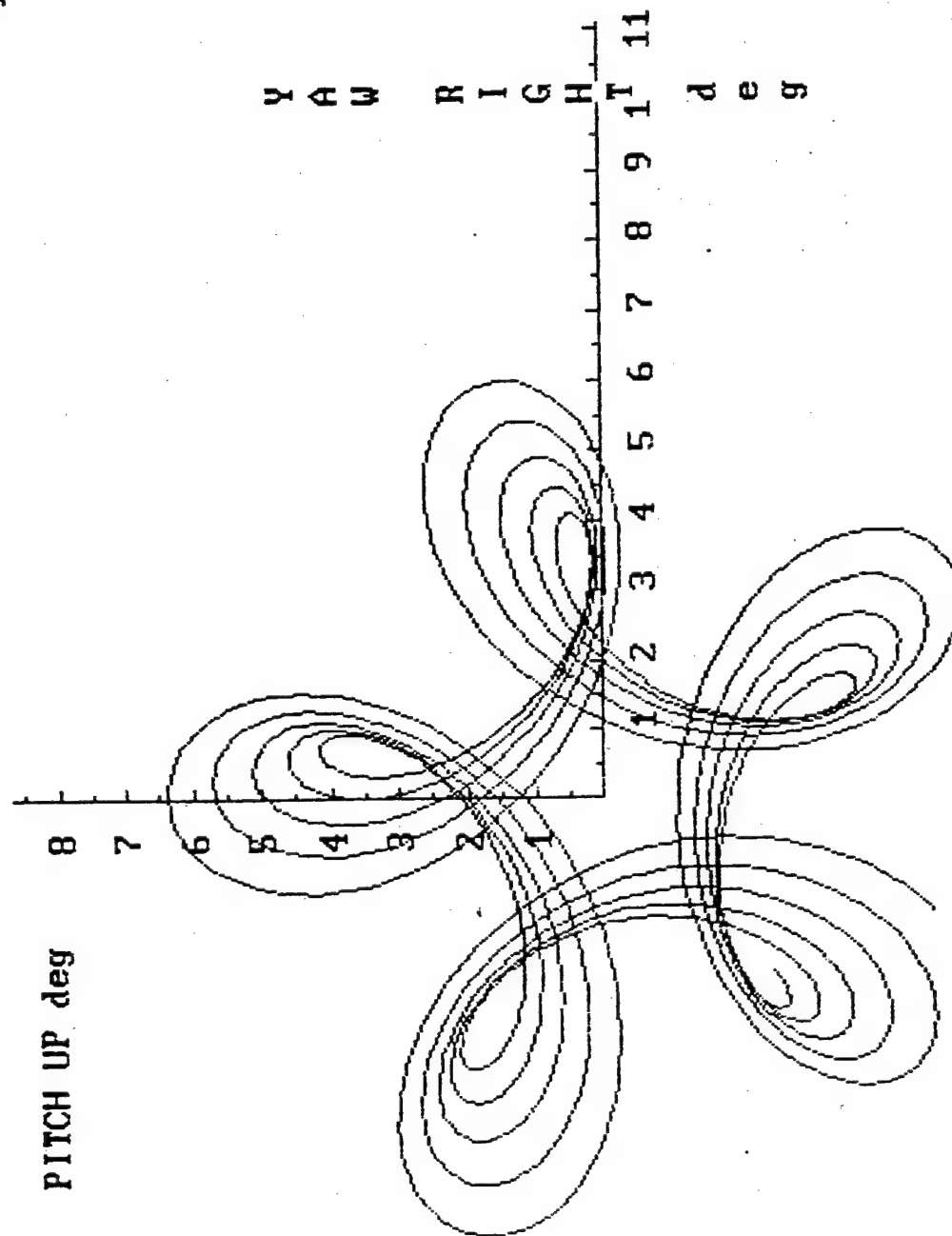


Figure 37 -- Epicycle Motion of Finner with 75 Hz Spin Rate

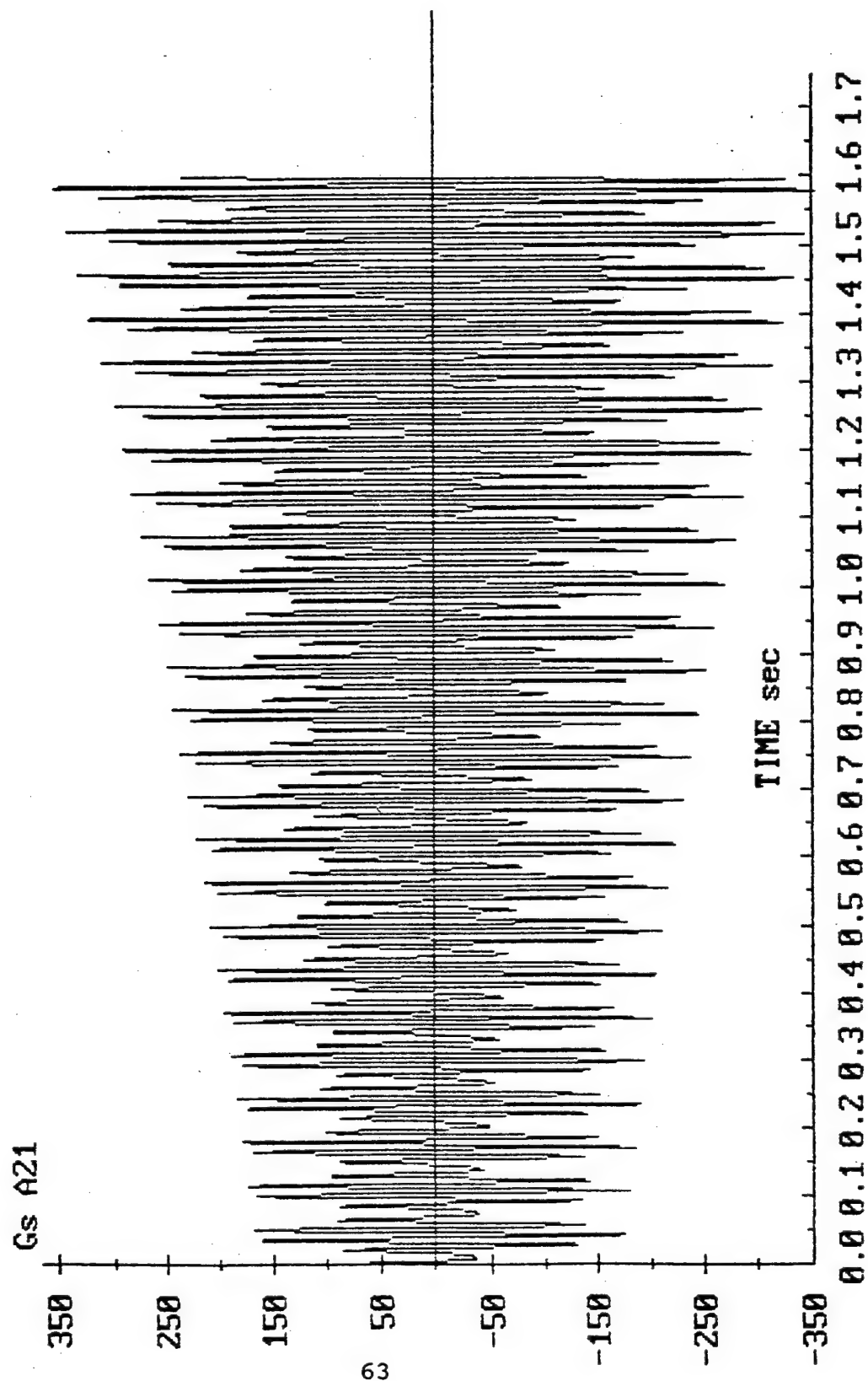


Figure 38 -- Output from One Radial Accelerometer for Figure 37

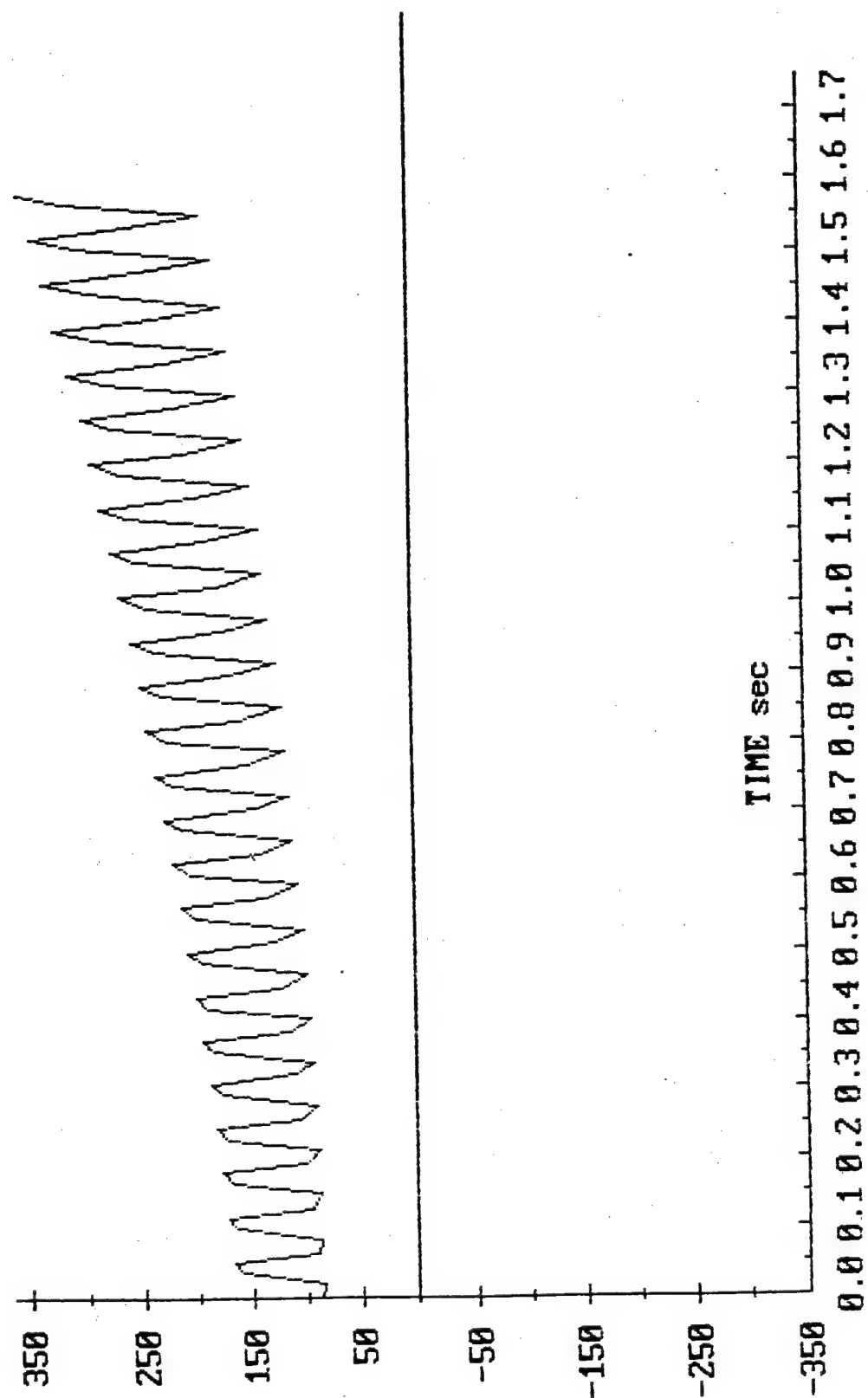


Figure 39 -- Peak Values from Figure 38

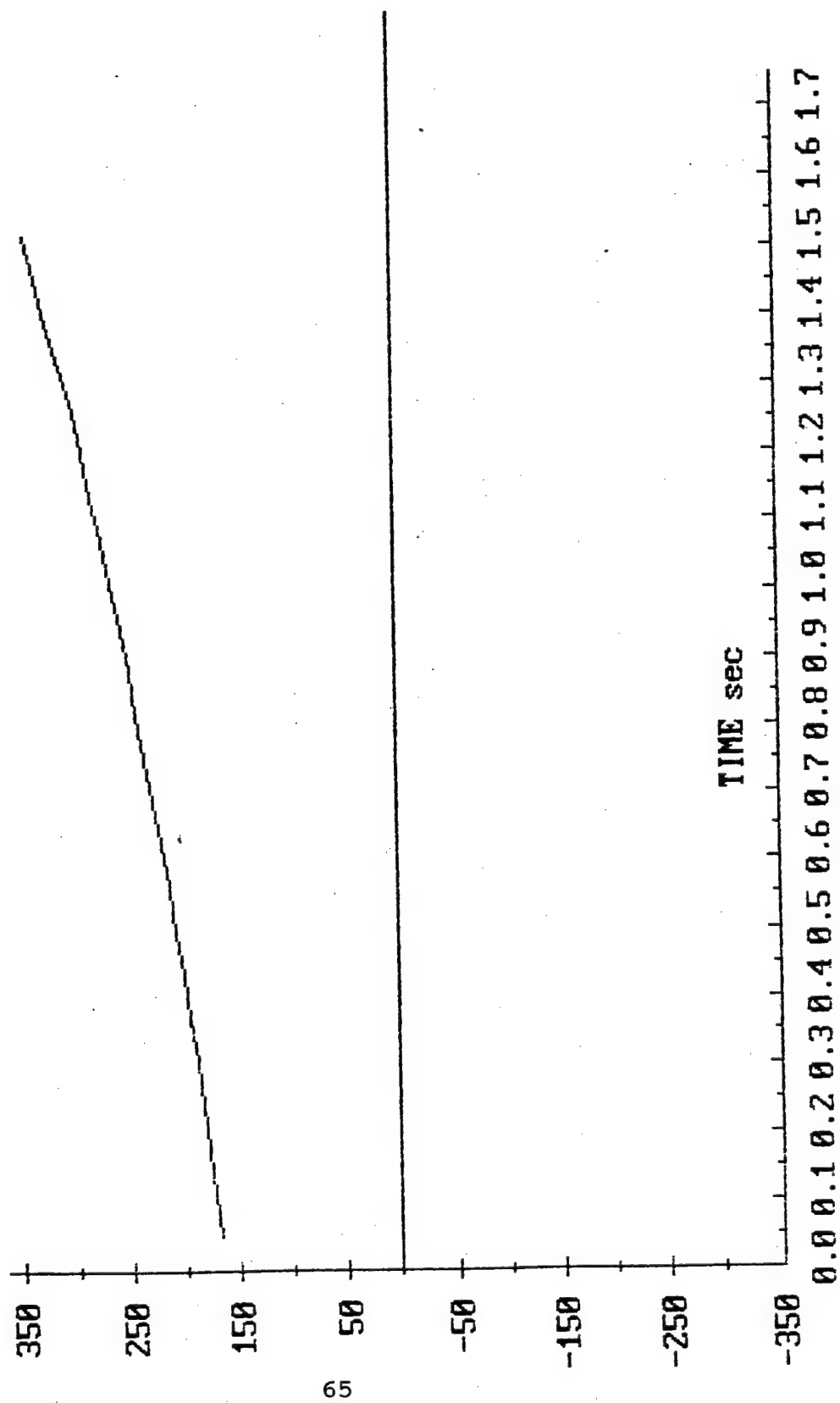


Figure 40 -- Peak Values from Figure 39

Table 9
Inflection Points from Course Data

Up Inflection Point Time	Down Inflection Point Time
.435	.243
.755	.563
1.075	.883
	1.203

Each of these time intervals is the same and calculates to 19.63 radians/second. The expected precession rate is 19.7 rads/sec. Using polynomial interpolation on the first two down and up inflection points gives the data shown in Table 10.

Table 10
Inflection Points from Interpolated Data

Up Inflection Point Time	Down Inflection Point Time
.398	.238
.719	.554

The average rate for these two intervals is 19.73 radians/sec and is nearly the expected rate of 19.7 rads/sec.

Trying something a little different this time, we went to the trace of the vector sum of two orthogonal radial accelerometers to see if the same surface wave existed on the peak values. Figure 41 shows the accelerometer trace and Figure 42 is the peak values from Figure 41. There is clearly a surface wave on Figure 41, and averaging time intervals between inflection points for just this course data gives an average rate of about 19.6 radians/sec.

It seems that for a fin stabilized projectile of the design considered in this analysis the precession rate can be identified as a surface wave on the trace of one radially oriented accelerometer or on the trace of the vector sum of two orthogonal radially oriented accelerometers. This in turn allows determination of the nutation rate, since the nutation-precession frequency is also determinable from either of these two acceleration traces. The technique presented here is identical to the one used for determining the nutation and precession rates for a spin stabilized projectile. The only difference is that in the outcome of the frequency analysis, the surface wave for the spin stabilized case is twice the

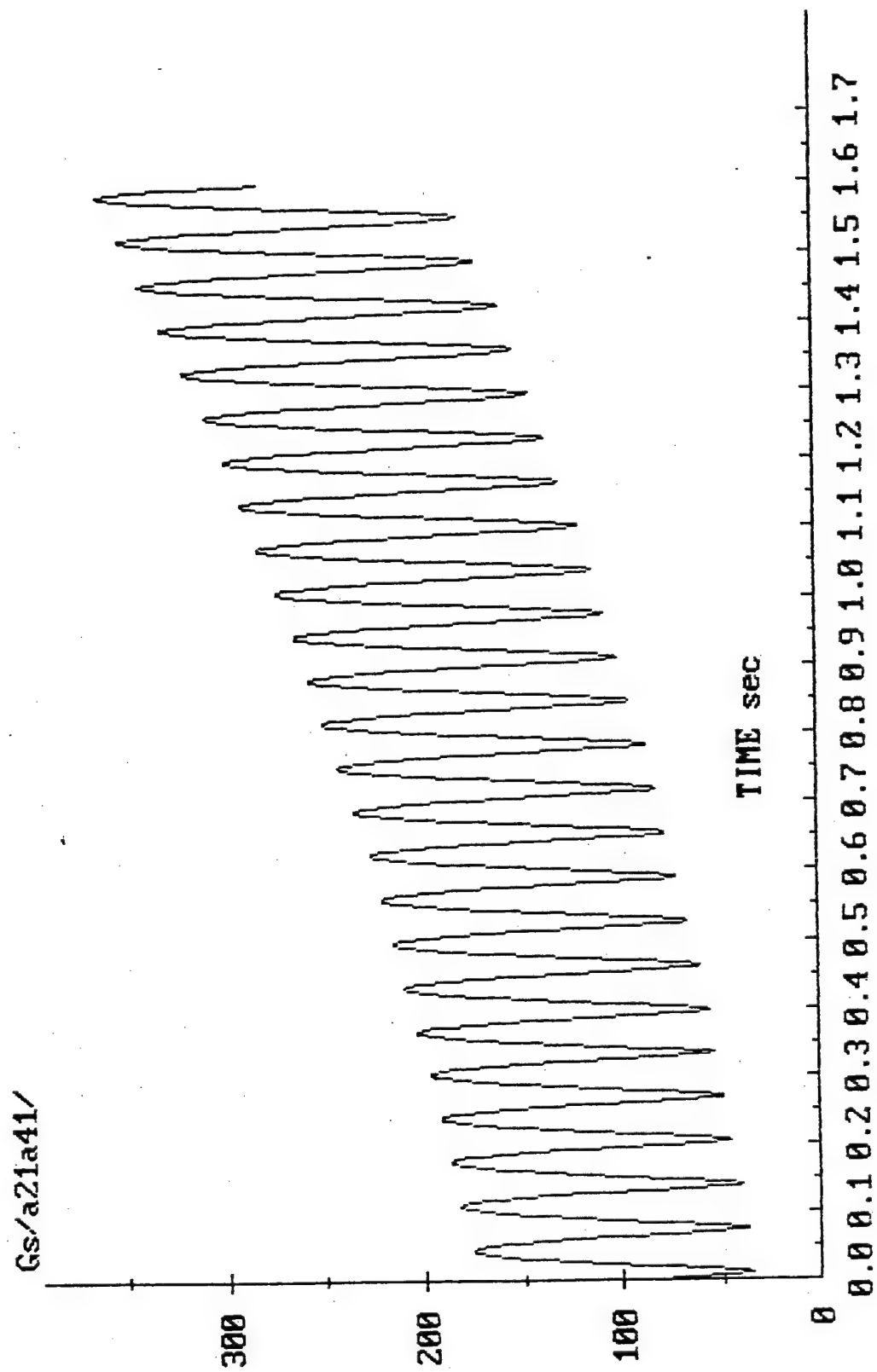


Figure 41 -- Output from Two Orthogonal Radial Accelerometers for Figure 37

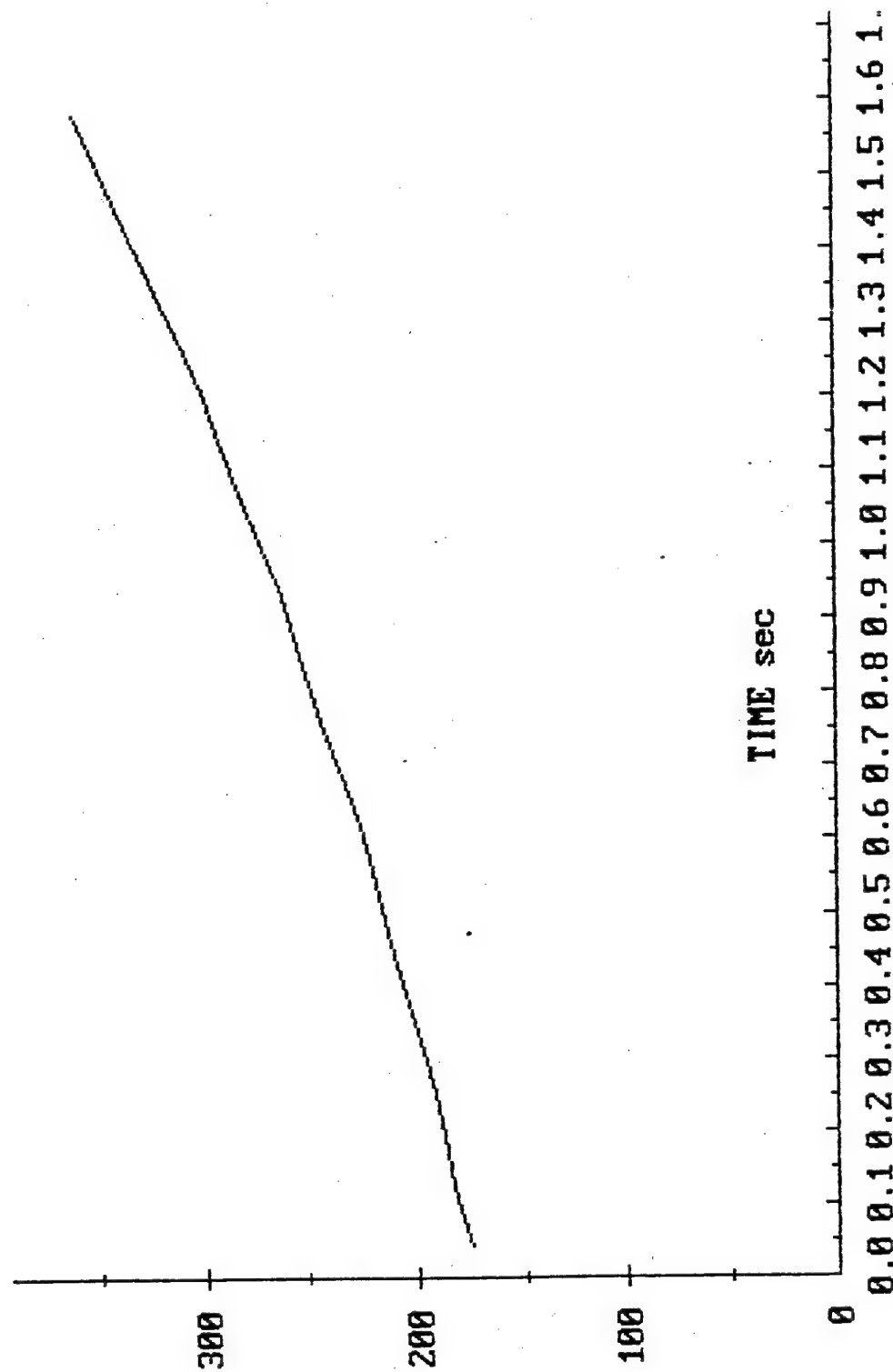


Figure 42 -- Peak Values from Figure 41

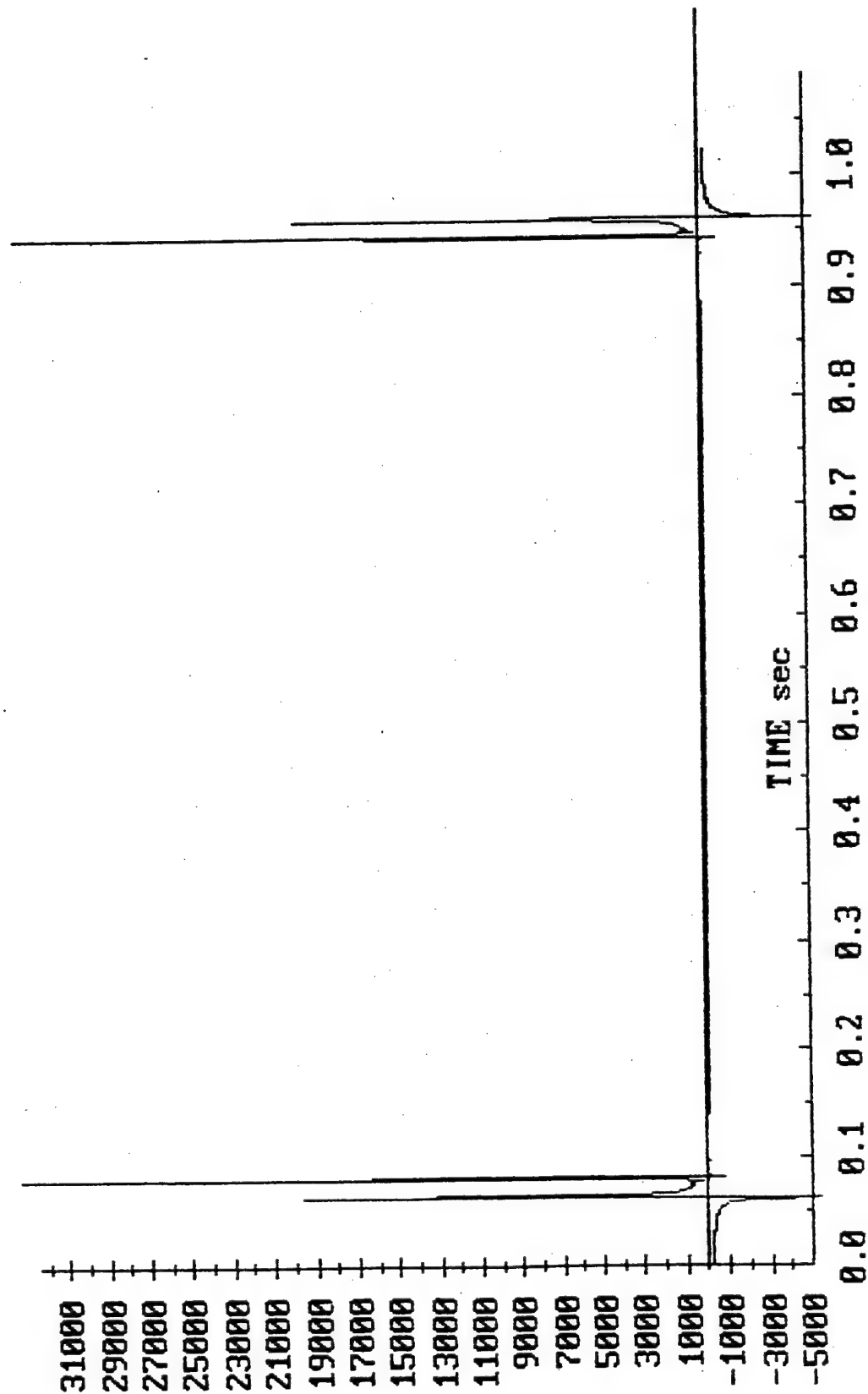


Figure 43 -- FFT Output for Figure 14 -- One Radially Oriented Accelerometer

precession rate, as opposed to just the precession rate in the fin stabilized case. The reason for this difference remains, as yet, unexplained.

3.10 Qualitative Assessment of Projectile Stability

An interesting secondary observation which can be made from the accelerometer traces just presented for the damped spin stabilized projectile and the undamped fin stabilized projectile is that these projectiles' stability is clearly seen in the output of just one or two radially oriented accelerometers. Figure 18 shows the one radially oriented accelerometer output for the motion in Figure 17. The damping nature of the very large amplitude swings clearly states that the projectile nutation arm is dampening out. Looking at Figure 19, the two radially oriented accelerometer trace, one sees the same nutation damping, as well as a general downward trend in the trace, indicating precession damping. These indication of damping in the motion are all signs of stable projectile flight.

Looking at the accelerometer traces for the undamped finner in Figure 37, just the opposite is seen. Figures 38 and 41 show that all accelerations are growing, clearly indicating instability in the projectile motion. Therefore, if the amplitude of yaw is not necessarily required from the telemetry, but rather a qualitative answer on the projectile stability is the goal, a very simple sensor configuration presents itself, with no complicated data reduction.

3.11 Fourier Analysis of Accelerometer Traces (F.M. Demodulation)

Utilizing fast fourier analysis software (the IEEE FFT842 subroutine), we had very encouraging results in identifying characteristic frequencies in the accelerometer output. More detailed presentation of this software is contained in monthly report number 6. Significant findings of this effort are reported here.

Analysis of a radially oriented accelerometer trace using FFT techniques identified the spin-nutation and the spin-precession rates of motion. Figure 38 shows the output from one radially oriented accelerometer for the undamped 75 Hz spin rate fin stabilized case. Figure 43 is the FFT output for the first 1024 data points, or about the first 1 second of flight. FFT software requires data sets of magnitudes 2^n , so 1024 data points were used ($2^{10} = 1024$). Figure 43 shows two peaks toward the left side in the FFT output time series, the first at time .064 and the second at time .080. The same two peaks appear on the right side, representing the imaginary components in the fourier transform.

The FFT routine employed performs an in-place transform of the

accelerometer trace time series data and outputs the characteristic frequencies in the same time space. Therefore, the times at each peak value correspond to a frequency using the following relationship:

$$f / (2\pi) / 1000. = 1000. * t / 2^n \quad (13)$$

where

$$n = 1024$$

and

$$t_1 = .064$$

$$t_2 = .080$$

Using (13), these two time points calculate to frequencies of 392.7 and 490.9 radians/sec, respectfully. Figure 43.2 plots the FFT time series converted to angular rates using equation (13). The first frequency, 392.7 is nearly exactly the spin rate minus the nutation rate ($471.2 - 78.3 = 392.9$), and the second is exactly the spin rate minus the precession rate ($471.2 - 19.7 = 490.9$). Whereas our moving average analysis technique has identified in this trace (Figure 38) the three frequencies of spin-nutation, nutation-precession, and precession for the fin stabilized case, the FFT has identified only one of these, spin-nutation, and the additional frequency of spin-precession.

3.12 Frequency and Amplitude Analysis of Outputs from Longitudinally Oriented Sensors

The longitudinally oriented accelerometer and gyroscope sensors presented in Figures 7 and 8, respectively, allow measurement of the rate of change of the total angle of attack, $\dot{\Omega}$. The maximum and minimum values of $\dot{\Omega}$, coupled with the measured nutation and precession rates of motion, allow determination of the yaw arms during the projectile flight, using equations (8) and (9).

The rate of change of the total angle of attack as determined from two longitudinal accelerometers or one longitudinal gyroscope is presented in Figure 44, for the undamped spin stabilized motion shown in Figure 1. The characteristic frequency for this trace is found by averaging many individual cycles to be the expected nutation minus the precession rate. This is the same result for the trace of two orthogonal radially oriented accelerometers (Figure 12).

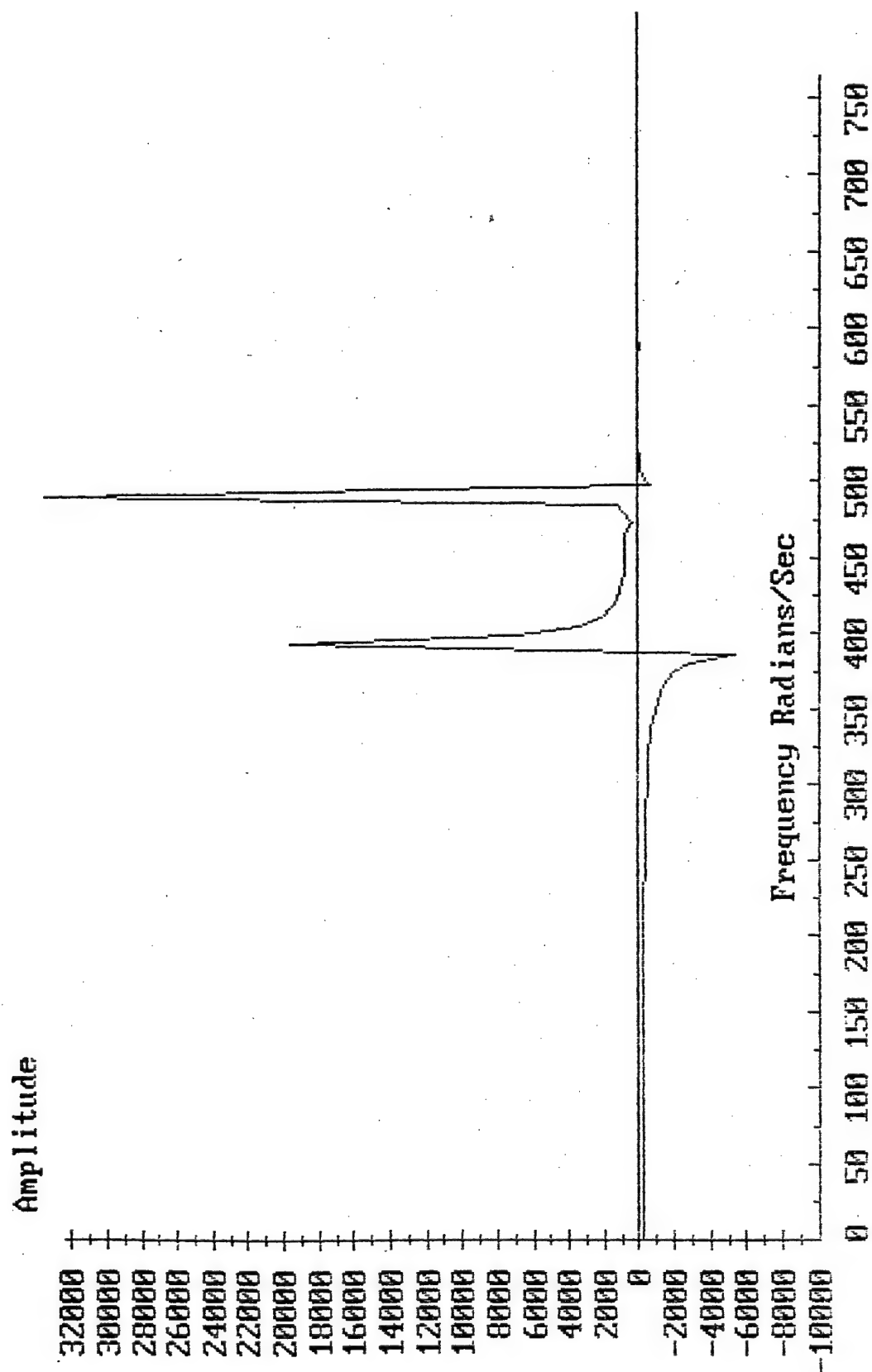


Figure
43.2 -- Angular Rate Output from FFT for Figure 43

For the first complete cycle in Figure 44, the maximum value is about 10.05 radians/sec and the minimum about 5.95 radians/sec. Given that the nutation and precession rates are determinable from the radial accelerometer configuration and are 144.8 and 13.8 radians/sec, respectfully, the yaw arms may be calculated using equations (8) and (9). The resulting nutation arm calculates as 3.17 degrees, and the precession arm as 8.51 degrees. These arms give a maximum yaw of 11.7 degrees, and a minimum yaw of 5.34 degrees, which is just about what is seen in the corresponding epicycle motion in Figure 1 and the angle of attack history in Figure 10.

Figure 45 shows the rate of change of total angle of attack from the longitudinal sensor configuration for the damped spin stabilized motion shown in Figure 17. For this motion the nutation rate is also 144.8 radians/sec, and the precession rate remains 13.8 radians/sec. This motion just includes damping. Similar analysis gives the maximum and minimum yaws found in Figure 17 and the angle of attack history in Figure 20.

For the undamped fin stabilized case shown in Figure 26, the analysis technique comprising equations (8) and (9) are correct, as well. For this fin stabilized case, the nutation rate is 63.42 radians/sec, and the precession rate is -24.38. Figure 46 is the measured rate of change of total angle of attack from the longitudinal sensor, and calculations give the same maximum and minimum yaws found in Figure 26 and Figure 27. Analyzing the undamped fin stabilized motion in Figure 37 also validates equations (8) and (9). Figure 47 shows the rate of change of angle of attack history for Figure 37. Figure 48 is the angle of attack history for Figure 37, and Table 11 shows the maximum and minimum values taken from Figure 48. The nutation rate for this motion is 78.3 radians/sec, and the precession rate is -19.7 radians/sec. Calculations using equations (8) and (9) give accurate results for the maximum and minimum yaws.

3.13 Direct Integration of Acceleration Traces

For fin and spin stabilized projectiles, both damped and undamped motion, we investigated the possibility of extracting epicycle motion information from the direct integration of accelerometer traces, without regard for the direction of the acceleration. This analysis effort revealed interesting similarities between the form of the acceleration output integrals and the yaw angle histories, but no absolute yaw values could be deduced. Monthly report number 5 gives a complete presentation of the analysis performed, and will not be restated in this report.

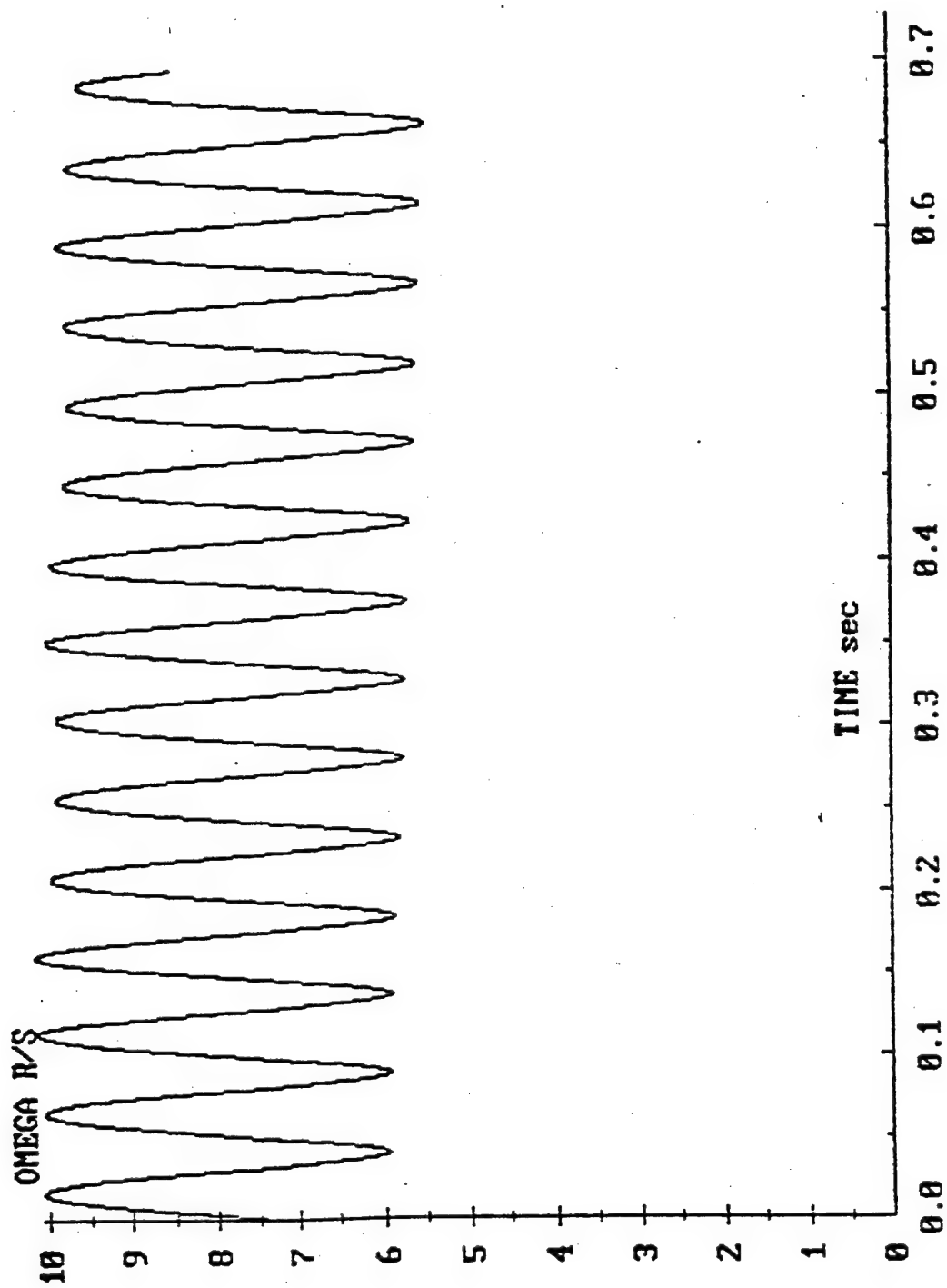


Figure 44 -- Total Yaw Angular Rate from Longitudinal Sensor for Figure 1

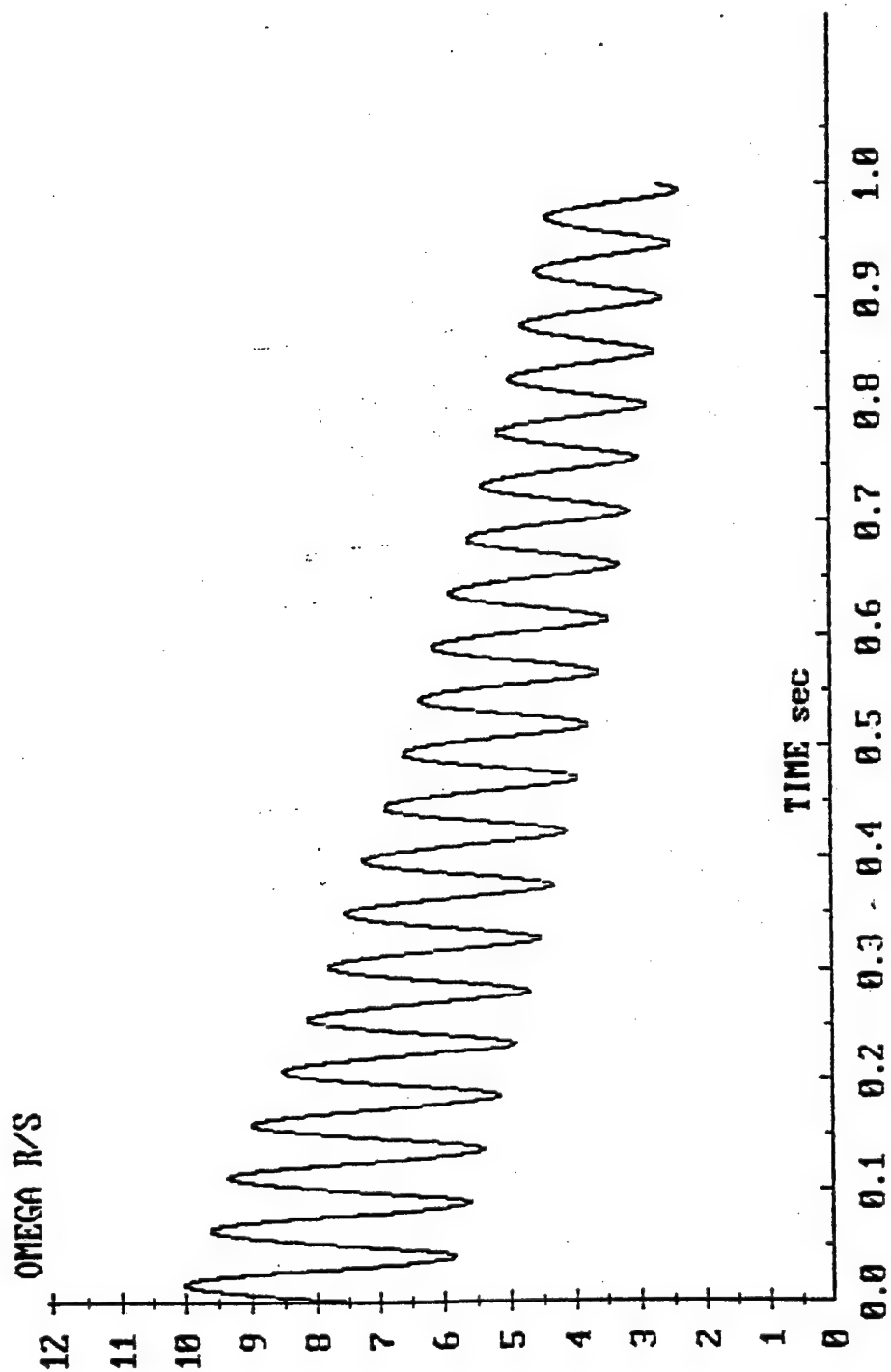


Figure 45 -- Total Yaw Angular Rate as Measured by Longitudinal Sensor

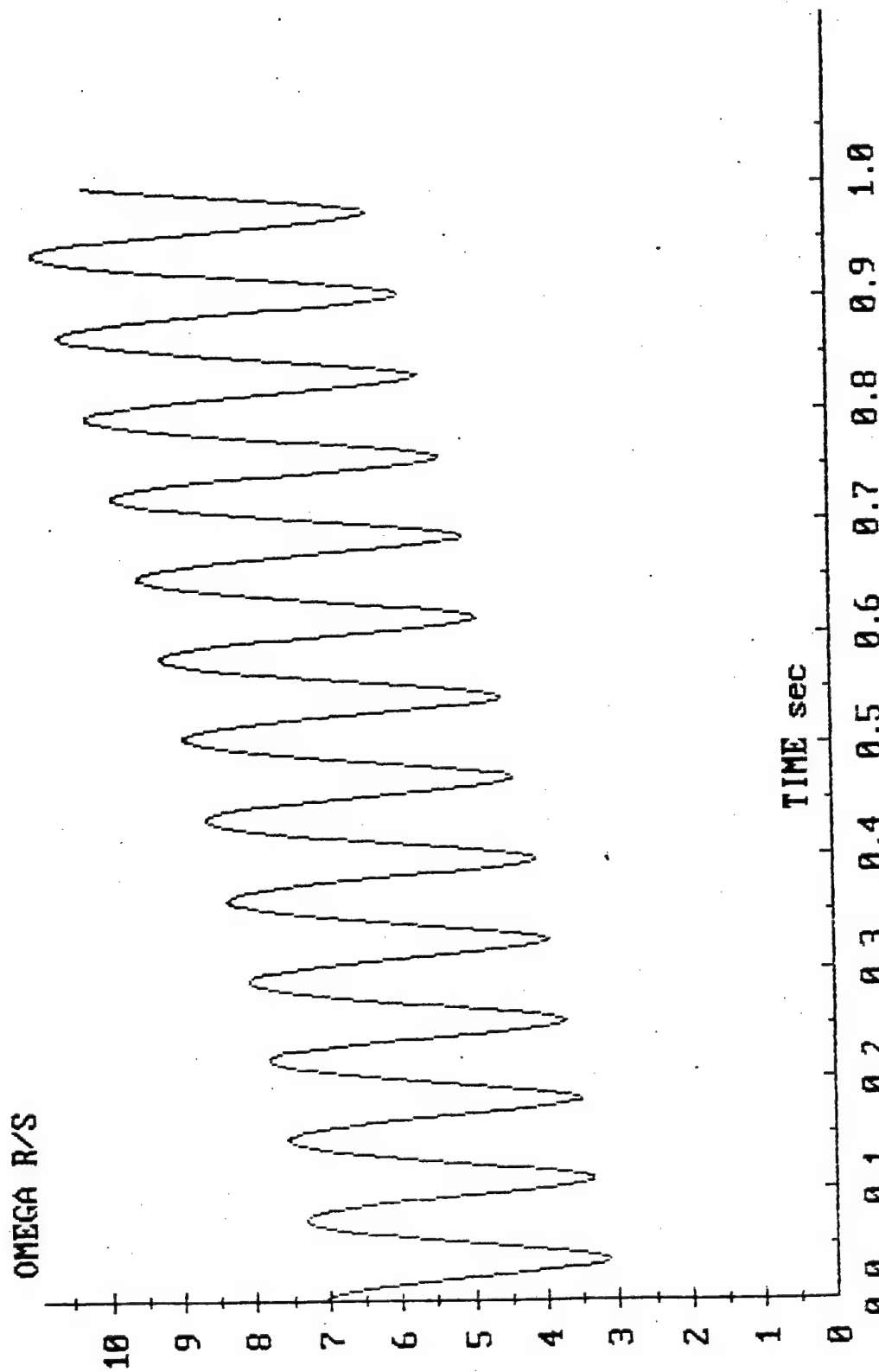


Figure 46 -- Rate of Change of Angle of Attack from Two Longitudinal Accelerometers for Figure 26

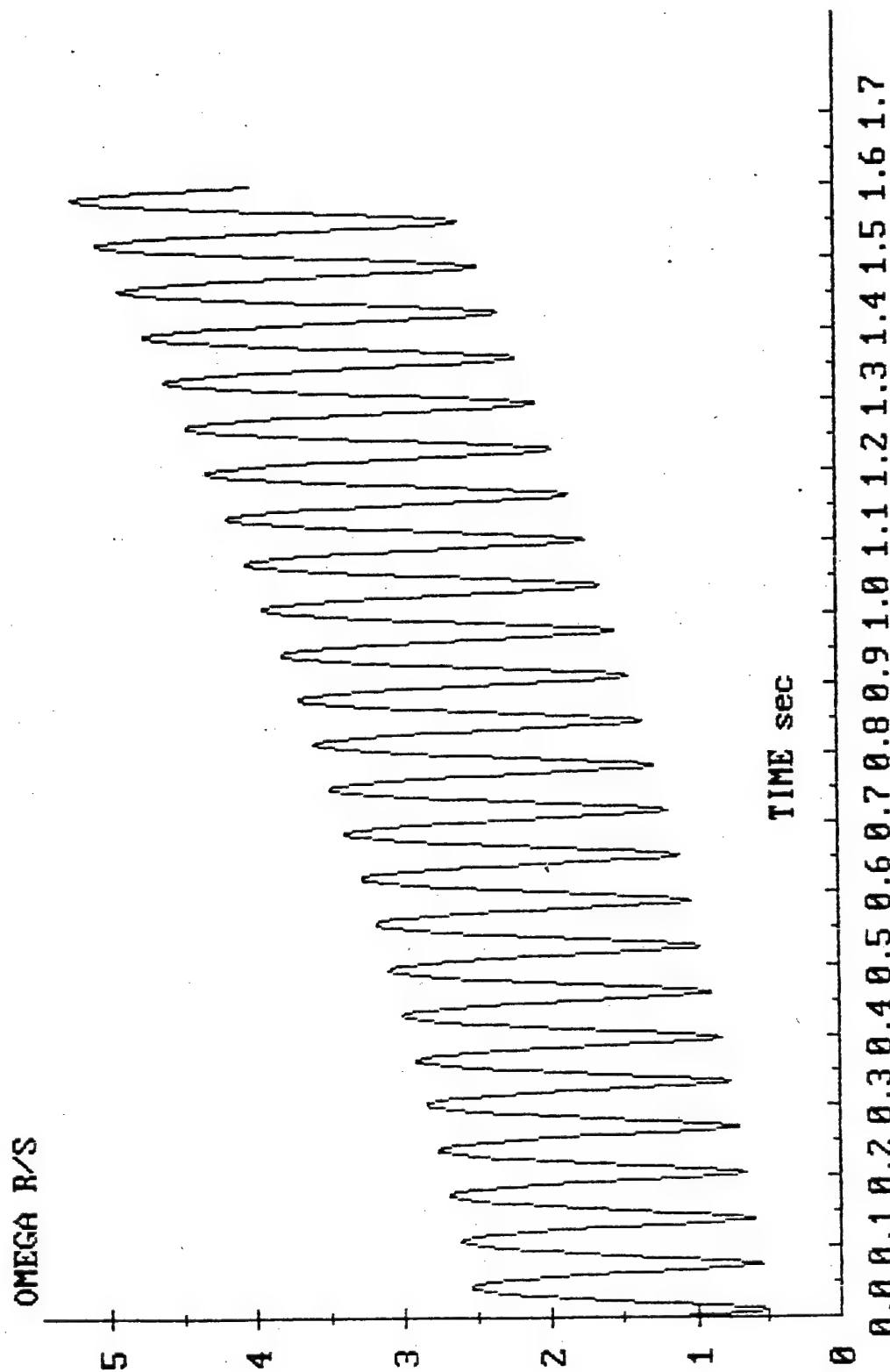


Figure 47 -- Rate of Change of Angle of Attack from Two Longitudinal Accelerometers for Figure 37

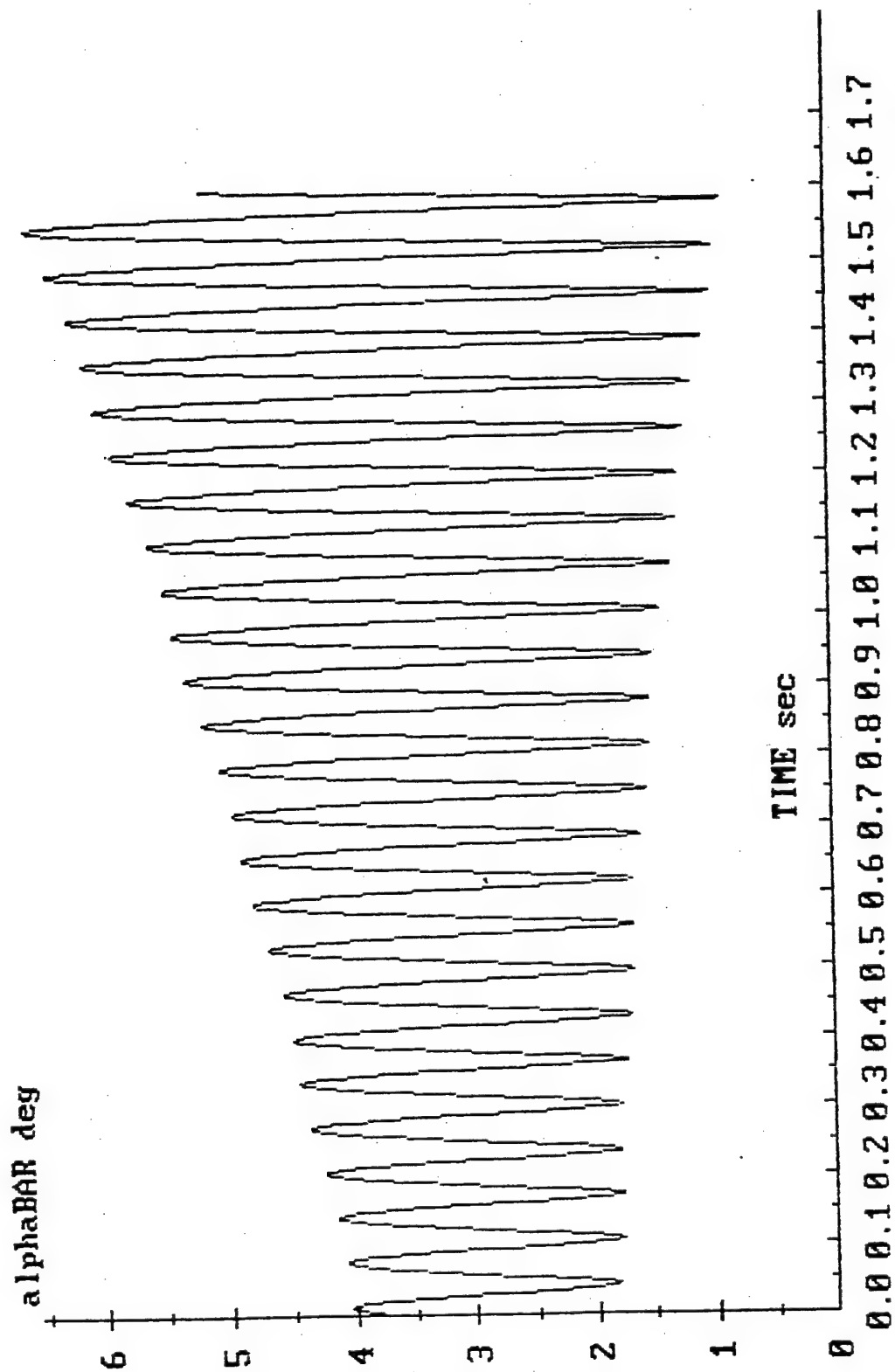


Figure 48 -- Angle of Attack History from 6DOF Simulation for Figure 37

3.14 Simultaneous Integration of Sensor Outputs

If the inertial roll orientation can be accurately determined during flight, the component missile accelerations, \dot{U} , \dot{V} , and \dot{W} , as measured by radially oriented accelerometers, can be numerically integrated to reconstruct the entire epicycle motion of the projectile. This integration technique can be similarly applied to the telemetry output from two radially oriented gyroscopes, which measure $\dot{\Psi}_m$ and $\dot{\Theta}_m$. These two data processing techniques are described in great detail in the second monthly report, and will not be repeated here. Suffice it to say that if roll orientation is known without error, nearly exact epicycle plots result from the integration. Figure 49 shows the known epicycle motion, from the 6-DOF simulation, of a spin stabilized projectile with 5 degrees initial yaw. In Figure 50, the motion is reconstructed using the simultaneous numerical integration of the sensor outputs. The motions are for all intents and purposes identical, except for the offset due to the unknown initial conditions. Nevertheless, the initial conditions become obvious after the integration of one precession cycle.

What does warrant repeat in this report, with respect to this data reduction technique, is the error in the reconstructed motion, if roll orientation is not known very well. Figures 51 through 56 show the resulting reconstructed motion for errors ranging from 10% to .1% in the spin rate used to calculate the relative roll orientation angle for each integration step. Clearly, the reconstructed motion does not begin to approach reality until the spin rate error is below .25%, and even with .1% error, the measured errors in pitch and yaw amplitude are approximately 10% from the actual.

Over a .25 second interval, with a spin rate of 1369 radians/sec and a spin rate error of .1%, the resulting cumulative angular error in roll orientation approaches 20 degrees. Following the trend in the results, a .01% roll error should give a 1% error in reconstructed pitch and yaw angles. This is probably an acceptable error, but it means that cumulative roll orientation errors cannot exceed about 2 degrees, for the total duration of the integration. A reasonable integration period would be at least one precession cycle. With spin rates about 100 times the precession rate, such required roll accuracy is a serious challenge.

The yawsonde is reported to be able to give inertial roll rates with accuracies less than .1 Hz and expected to be able to give accuracies to less than .05 Hz (private communication with Dave Hepner). Measurement of inertial roll rate, as opposed to the eulerian roll rate, is accomplished by setting the optical slits straight up and down so that they are sigma insensitive. The extreme accuracy is possible because the rate measurement is taken from the sun angle, which is a fixed reference point from which to re-zero the

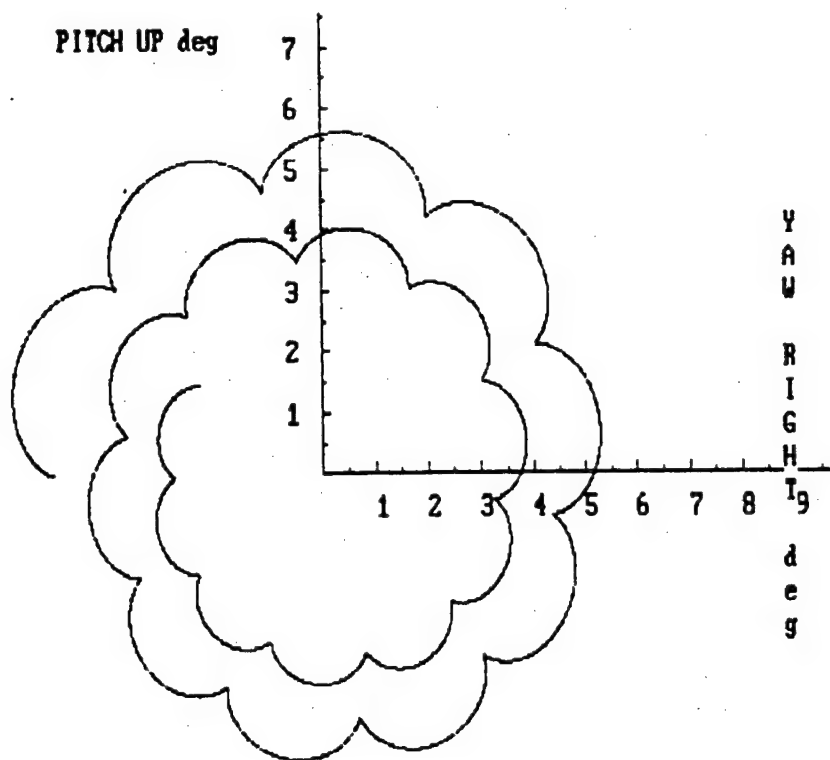


Figure 49 Original Epicycle Motion from 6-DOF Simulation

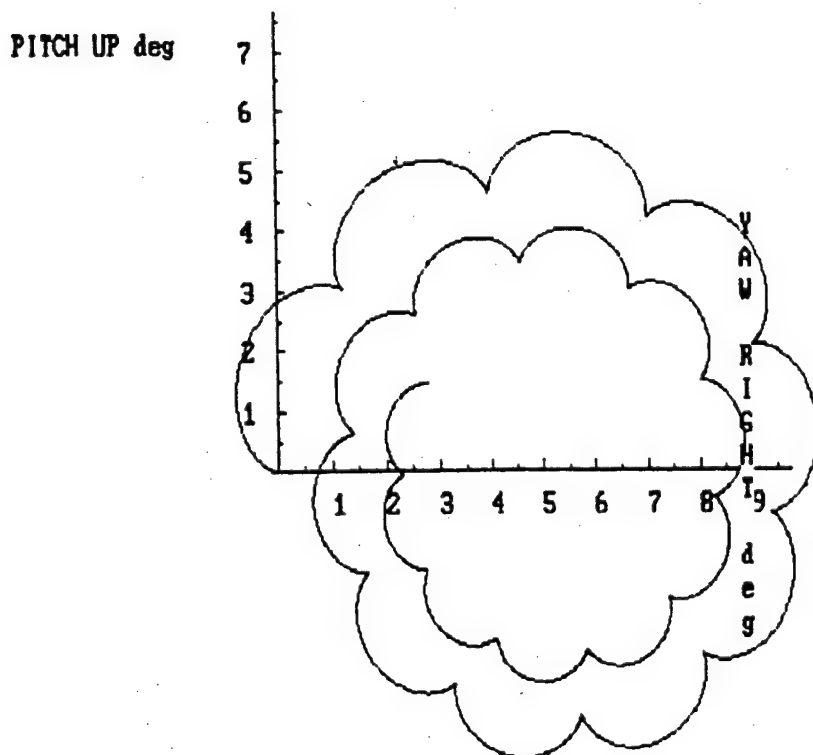


Figure 50 Reconstructed Motion with zero Spin Rate Error

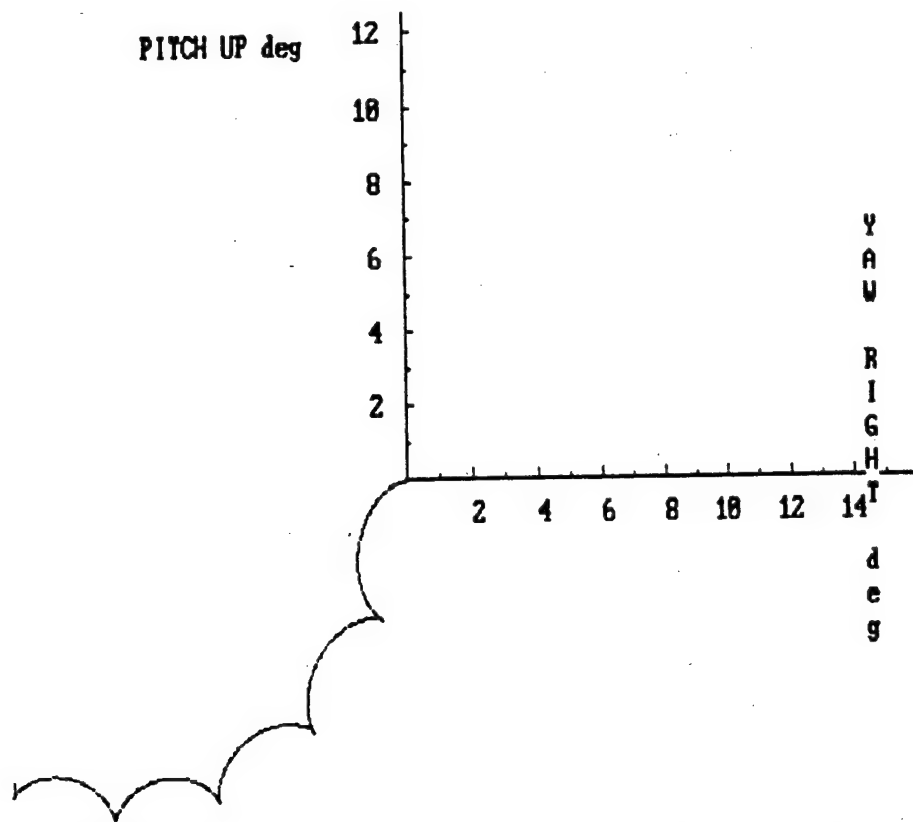


Figure 51 Reconstructed Motion with 10% Spin Rate Error

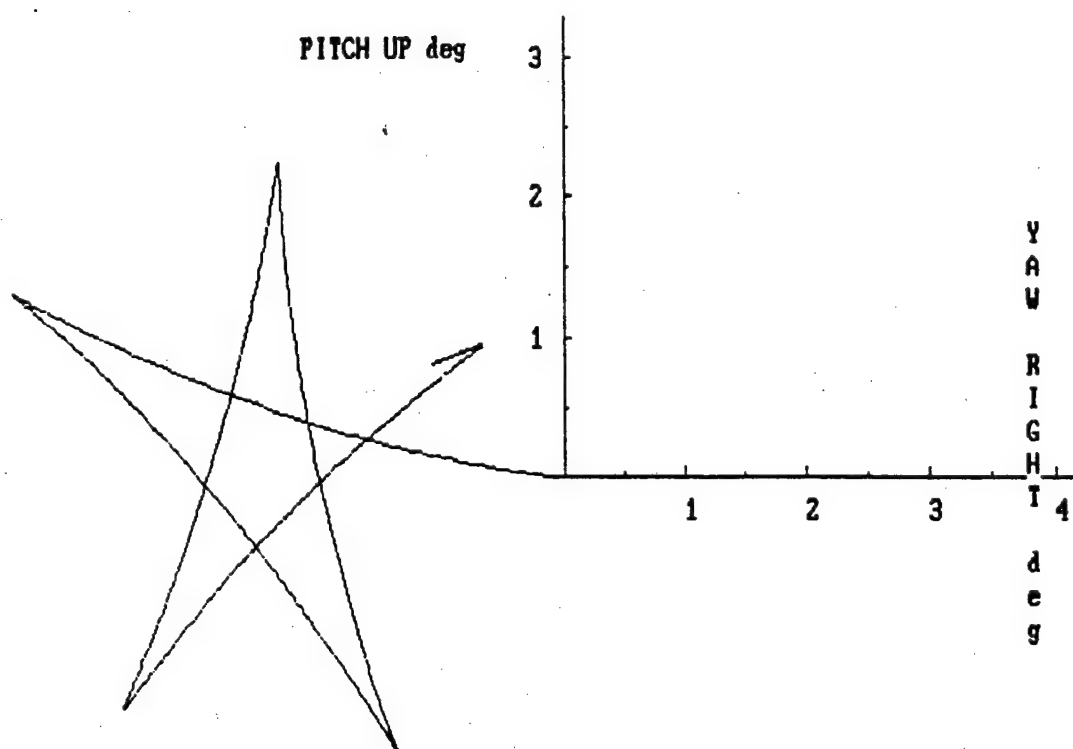


Figure 52 Reconstructed Motion with 5% Spin Rate Error

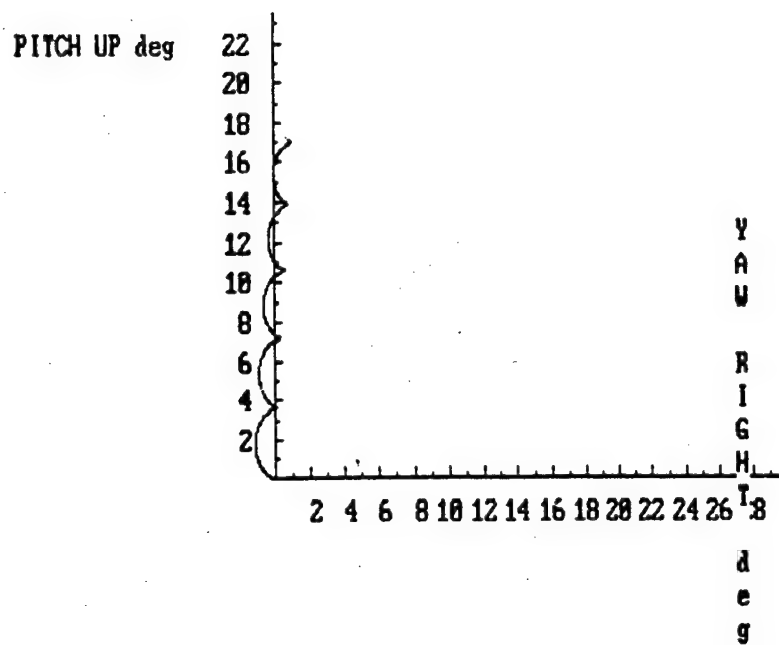


Figure 53 Reconstructed Motion with 1% Spin Rate Error

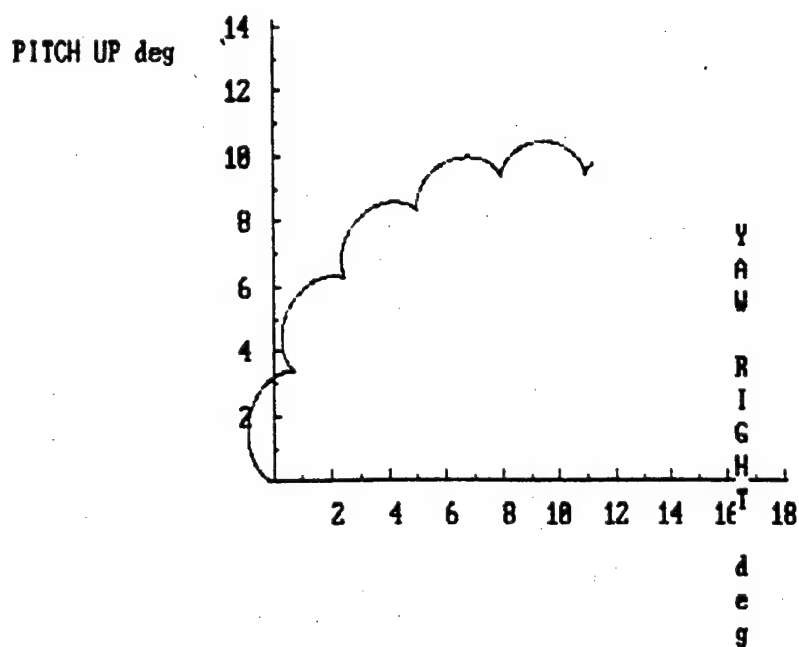


Figure 54 Reconstructed Motion with 0.5% Spin Rate Error

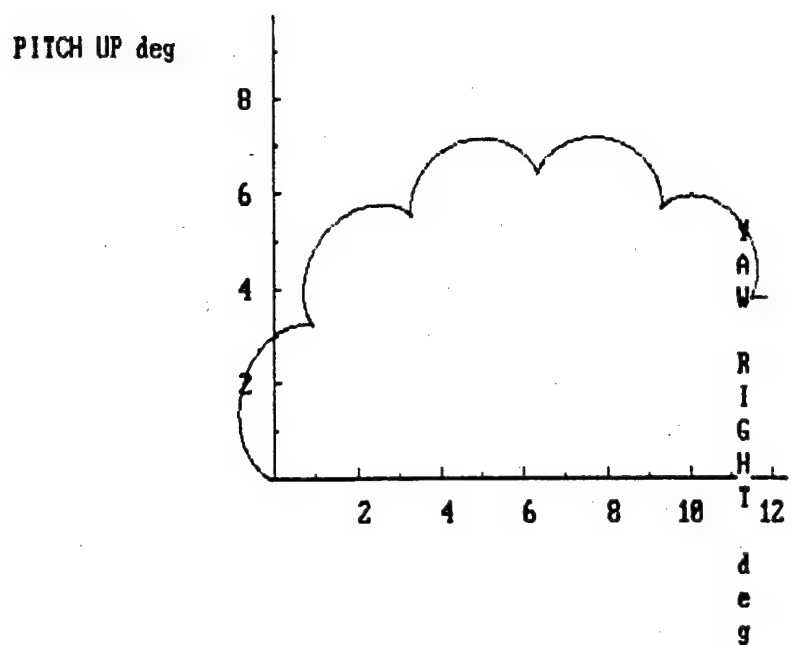


Figure 55 Reconstructed Motion with 0.25% Spin Rate Error

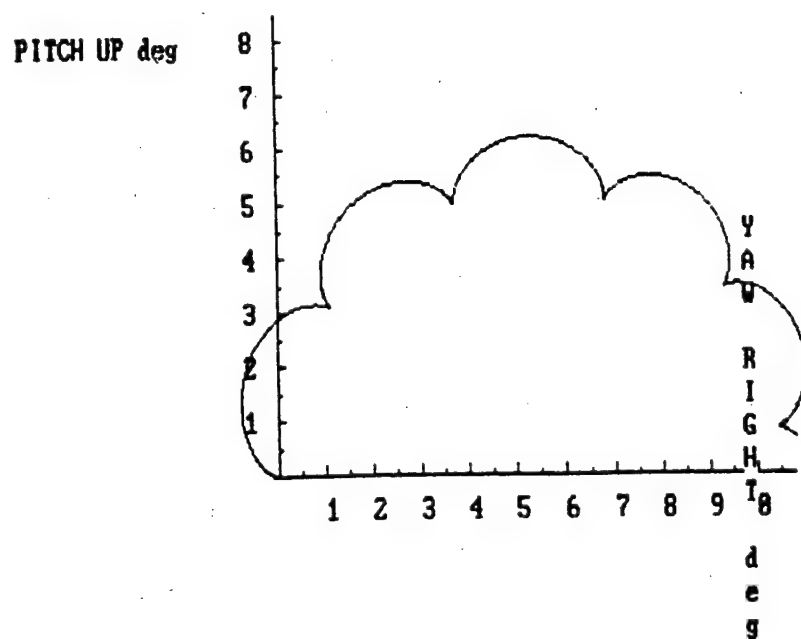


Figure 56 Reconstructed Motion with 0.10% Spin Rate Error

measurement after each cycle. Therefore, scale factor errors cannot accumulate. .1 Hz accuracy on a typical 155mm projectile (1369 radians/sec spin rate) translates to about .045%. By our estimate, this should result in less than a 5% error in the reconstructed motion using this integration technique.

3.15 Determining roll orientation with Phase Locked Loop

An alternate technique of achieving very accurate roll orientation was assessed, which employed a phase locked loop filtering mechanism to sense the gravity vector every time an accelerometer passed through the absolute vertical. Monthly report 3 gives detailed explanation of the theoretical forces and accelerations involved and the filtering process, not to be repeated here. The advantage to this technique, if correct in determining roll orientation, is that high accuracy is gained by re-zeroing the roll angle with a fixed reference after each cycle. This is similar to how the yawsonde gains its roll rate accuracy, as just presented. We have, however, not been able to resolve whether this mechanism measures inertial roll or eulerian roll with respect to the gravity vector. We suspect it is eulerian roll (inertial roll modulated by the yaw angle); and therefore, its practical value in aiding the determination of projectile yaw through the sensor output integration techniques has yet to be established.

4.0 Results and Discussions

4.1 General

The research just presented shows that there are several accelerometer and gyroscope telemetry options available to assess the stability and determine the yaw of both spin and fin stabilized projectiles. These configurations range from simple to the complex.

4.2 The binary answer.

The output from one radially oriented accelerometer indicates stable projectile flight if the acceleration history shows damping, and vice-versa. Damping is indicated in the accelerometer trace if the magnitudes of successive acceleration amplitudes are decreasing over time. This very simple configuration has some utility by itself. For example, an investigator may wish to determine if a projectile configuration undergoes alternate periods of stability and instability over the course of a trajectory involving varying flight velocities, roll rates, and atmospheric conditions. Isolation of the trajectory circumstances which indicate instabilities is an important first step towards understanding and

solving the problem in the projectile design.

4.3 Calculate the yaw arms from the measurement of the nutation, precession, and total yaw angular rates of motion

A.M. and F.M. demodulation of the outputs from two orthogonal radially oriented accelerometers gives the nutation and precession rates of motion for both spin and fin stabilized projectiles. In addition, the output from two longitudinally oriented accelerometers, or one longitudinally oriented gyroscope gives the maximum and minimum total yaw angular rate, Ω , for each nutation cycle. Using equations (8) and (9), one can then calculate the yaw arms at each nutation cycle:

$$\Omega_{max} = \Omega_{pre} * \alpha_{pre} + \Omega_{nut} * \alpha_{nut} \quad (8)$$

and

$$\Omega_{min} = \Omega_{pre} * \alpha_{pre} - \Omega_{nut} * \alpha_{nut} \quad (9)$$

This telemetry concept satisfies the objectives of this research program. That is, to determine the in-flight yaw of the projectile. For both spin and fin stabilized projectiles, this concept employs 4 accelerometers, or 2 accelerometers and one two-axis rate gyroscope. Depending on the launch environment of the projectile, i.e. high set-back acceleration and high spin acceleration, the use of off-the-shelf gyroscopes may not be practical. This is because the gyroscope is less durable than the accelerometers. However, recent advances in micro-device gyroscopes, which are hardenable to the level of accelerometers, may eliminate this concern. If use of a gyroscope is possible, this offers the advantage of greater accuracy in measuring the total yaw angular rate of motion, since the gyroscope directly measures this angular rate, whereas the alternate technique of differencing the outputs of two axially oriented accelerometers is affected by in-flight drag accelerations and transverse accelerations on top of the acceleration due to the yawing motion.

4.4 Reconstruct the epicycle motion of the projectile by measuring and then simultaneously integrating \dot{U} , \dot{V} , and \dot{W} , or $\dot{\Psi}_m$ and $\dot{\Theta}_m$

This telemetry concept is the most complex. However, it is the technique which more completely describes the yawing motion of both fin and spin stabilized projectiles.

\dot{V} and \dot{W} are measurable from two sets of two orthogonal radially

oriented accelerometers separated by an axial distance. \dot{U} is measurable from two longitudinally oriented accelerometers.

$\dot{\Psi}_m$ and $\dot{\Theta}_m$ are measurable from two orthogonal radially oriented two-axis rate gyroscopes.

The acceleration or angular rate outputs from either the accelerometer or gyroscope configurations are then numerically integrated to give a two dimensional trace of the complete epicycle motion of the projectile. This reconstructed motion has the advantage of providing continuous yaw data during flight, without the need for sophisticated demodulation of sensor signals. The accelerometer based system, however, has the limitation that the projectile center of gravity must be known and unchanging during flight. On the other hand, the gyroscope based system is the most powerful, in that all mass properties of the projectile may vary without affecting the accuracy of results.

Each of these techniques requires accurate knowledge of a relative inertial roll orientation angle to within .01% error for a 1% error in reconstructed motion. Roll orientation may be determinable from real time yawsonde data, direct measurement of inertial spin rate using two off-axis radial accelerometers or one radially oriented gyroscope, or perhaps with a mechanism for sensing the absolute vertical of the gravity vector.

5.0 Conclusions

5.1 General

The objectives of this Phase I study have been to develop a telemetry configuration based on inertial sensors, such as accelerometers or gyroscopes, which will allow accurate determination of the in-flight yaw of both spin and fin stabilized projectiles.

The results indicate that all objectives of this Phase I study have been met. Several configurations, using accelerometers, gyroscopes, or combinations have been derived and analyzed. The results of the analysis indicate that the yawsonde can be replaced with a package of inertial sensors.

Option 1 is to use two orthogonal radially oriented accelerometers coupled with two tandem axially oriented accelerometers. This four accelerometer system will allow calculation of the precession and nutation yaw arms for both spin and fin stabilized projectiles at any time during the trajectory. A modification to this concept is to replace the two tandem axially oriented accelerometers with one two-axis rate gyroscope. Both sensors perform the

same function. However, the gyroscope may provide greater accuracy in measuring the yawing angular rate of motion, which is required for determining the yaw arms.

A second option is to employ two pairs of orthogonal radially oriented accelerometers in tandem, with two tandem axially oriented accelerometers. This six accelerometer system will allow, through numerical integration, direct reconstruction of the two-dimensional epicycle motion of both spin and fin stabilized projectiles. This telemetry output will provide a continuous graphical record of the yawing motion of the projectile during the entire trajectory.

A modification to this second option is to substitute two orthogonal radially oriented two-axis rate gyroscopes in place of all six accelerometers. The outputs from these two gyroscopes will also allow, through numerical integration, direct reconstruction of the two-dimensional epicycle motion of both spin and fin stabilized projectiles. However, this gyroscope based system has the advantage that the projectile mass properties and center of gravity can be unknown and changing during flight, without affecting the determination of the yawing motion. The six accelerometer configuration is limited to projectiles with a known and unchanging center of gravity.

The only disadvantage to employing the configurations in the second option, the two gyroscope and the six accelerometer based system, is the requirement for an independent measurement of the projectile spin rate. Accurate spin rate knowledge allows decomposition of the pitch and yaw accelerations and angular rates into perpendicular components prior to numerical integration. Three concepts for providing accurate projectile spin rate have been presented in the body of this report.

5.2 Sensor Technical Data

There is no question that the required components can be obtained. The performance requirements for the inertial components are described in Monthly Report 5. *** go into report 5 and pull them out and present here *** The issue is being able to obtain components that can withstand the required launch environment (up to 13000 g's set-back in a 155mm projectile), and then function at the required performance levels. In the case of the accelerometers, they must maintain their linearity and be matched after the initial launch shock loading. In the case of longitudinally oriented accelerometers, this shock will be along the sensitive axis of the accelerometer.

6.0 Recommendations

The objective of the research was to develop telemetry configurations for determining yaw. This is certainly beyond the capabilities of the qualitative stability answer given by one radially oriented accelerometer. The individual nutation and precession yaw arms must be determined in order to give a quantitative answer on the magnitude of the in-flight yaw of the projectile.

For two mode epicycle motion -- nutation and precession -- yaw arms may be readily determined from the use of two axially oriented accelerometers or one gyroscope, coupled with two radially oriented accelerometers. Basic projectile stability and aerodynamics will be determinable from this configuration and data reduction. This technique should be tested and refined to see its performance with respect to real sensor capabilities and more complicated epicycle motions, which include more than two modes.

For the most complex projectile motions, involving projectiles with changing inertial parameters, complete reconstruction of the pitch and yaw histories should be performed using either accelerometer, gyroscope, or hybrid configurations, coupled with an independent measurement of the inertial spin, in order to decompose radial outputs into orthogonal rates for simultaneous integration. The resulting reconstructed motion will allow detailed analysis of the projectile stability and aerodynamic and inertial parameters, regardless of the complexity of the motion.